Dynamical Horizons in Binary Black Hole Mergers

Von der QUEST-Leibniz-Forschungsschule
der Gottfried Wilhelm Leibniz Universität Hannover

zur Erlangung des Grades

Doktor der Naturwissenschaften
Dr. rer. nat.

genehmigte Dissertation von

M.Sc. Daniel Klaus Ortwin Pook-Kolb

2020

Promotionskommission:

Prof. Dr. Domenico Giulini (Vorsitzender)
Prof. Dr. Bruce Allen
Prof. Dr. Erik Schnetter
Prof. Dr. Lars Andersson

Gutachter:

Prof. Dr. Bruce Allen
Prof. Dr. Erik Schnetter
Prof. Dr. Ivan Booth

Tag der Promotion: 2. Oktober 2020

Abstract

Marginally outer trapped surfaces (MOTSs) are the main tool in numerical relativity to infer properties of black holes in simulations of highly dynamical systems. On the one hand, the present work extends previous numerical methods in order to allow tracking of highly distorted horizons in axisymmetry. On the other hand, by applying the new method to a family of initial data as well as to simulations of head-on collisions of black holes, we discover three new phenomena: (i) the merger of MOTSs providing a connected history of the full merger in terms of marginal surfaces without any "jumps", (ii) the formation of self-intersecting MOTSs immediately after the merger, and (iii) a non-monotonicity result for the area of certain smoothly evolving MOTSs.

The merger of MOTSs closes a gap in our understanding of binary-black-hole mergers in terms of the quasilocal horizon framework and provides the quasilocal analog of the famous "pair-of-pants" picture of the event horizon of two merging black holes. It allows tracking the evolution of properties such as the area through the highly dynamical regimes from the initially separate to the final common horizon.

Through a detailed analysis of geometrical and dynamical properties, we uncover features of the horizons not often considered. In particular, we show why the area increase law for smoothly evolving MOTSs fails to hold in some of the cases analyzed here. Furthermore, we demonstrate a surprisingly direct correspondence of the decay behavior of multipoles and the shear on the outermost horizon with the quasinormal modes of a Schwarzschild black hole.

An important role is played by the spectrum of the MOTS stability operator, for which we provide numerical examples of the connection between invertibility of the operator and the existence of a MOTS. Furthermore, we give a prospect of how the full spectrum can become useful for gaining more insight into the merger in absence of symmetries.

Finally, a first working generalization of the new numerical algorithm to non-axisymmetric situations is shown, proving the general applicability of the method.

Keywords: Dynamical Horizons, MOTS, Black Holes, Numerical Relativity

Acknowledgements

This work would not have been possible without the help and support of many people. First, I would like to thank all my colleagues at the Max Planck Institute for Gravitational Physics (Albert-Einstein-Institute) Hannover for providing a great work environment often with helpful discussions, in particular Anjana Ashok, Liudmila Fesik, Xisco Jiménez Forteza, Shilpa Kastha, Pierre Mourier, Lars Nieder, Alex Nielsen, Andrey Shoom, Benjamin Steltner, and Julian Westerweck. This extends to the helpful administration in our institute as well as the QUEST-LFS and IMPRS-GW offices, including Sandra Bruns, Oksana Khiari, Gabriele Richardson, and especially Birgit Ohlendorf. Furthermore, I would like to thank the Perimeter Institute for the friendly hospitality during a two-week stay in mid of 2019.

I am very thankful for inspiring discussions with Abhay Ashtekar, Ivan Booth, Rodrigo Panosso Macedo, and Soham Mukherjee. I thank Bruce Allen for his support and for having made it possible for me to work at this institute. Throughout the projects leading to this thesis, many discussions and theoretical as well as practical advice of Ofek Birnholtz, José Luis Jaramillo, and Erik Schnetter were key to advance further, for which I am very thankful.

I am deeply grateful for the patient support of Badri Krishnan, who spared no effort to further my progress and physical understanding with countless discussions, advice, and ongoing active assistance.

Most of all, I thank my sister and my parents, and especially my father, for all their support, help, and love, which made it possible for me to study physics.

Contents

List of Figures

List of Tables

Chapter 1

Introduction

Black holes combine some of the most remarkable properties of objects that occur in nature. This holds for their theoretical description as well as in astrophysical situations: In stationary settings, they belong to the simplest exact solutions of Einstein's theory of general relativity, while at the same time providing the prime example of what is sometimes referred to as the "breakdown of the theory" due to the singularity they hide behind their horizon. In realistic contexts, they often are far from dark and instead power some of the most radiant and energetic phenomena in the observable universe. It is this combination of properties that makes them so interesting and important to understand. Due to their simplicity, stationary black holes lend themselves to detailed mathematical studies and perturbative analyses provide remarkable results for understanding black holes close to equilibrium. Nature itself presents us an abundant supply of black holes even in highly dynamical situations, while the enormous technical difficulty in accessing this supply observationally has been overcome through the now numerous direct detections of gravitational waves emitted during the coalescence of two black holes [1, 2, 76, 77, 97, 100] and the success in constructing the first image of the near horizon region of a supermassive black hole [3].

However, the mathematical simplicity of stationary black holes is strikingly contrasted by the complexity of understanding them in dynamical situations, such as the observed mergers, which are far beyond the applicability of perturbation theory. In these regimes, their defining property—the black hole region as the part of spacetime from which no information can escape to infinity—does not yield a physically meaningful interpretation capturing the details of the dynamics. The event horizon, defined as the boundary of this region, can grow in flat space regions due to its teleological nature. An example is provided by the Vaidya spacetime where an event horizon may form in a flat Minkowskian region in anticipation of a collapsing shell of null dust (see e.g. [20]). Moreover, a "precursory collapse" was recently found in [40], which describes an event horizon developing inside a neutron star even before it merges with a large black hole.

A non-teleological alternative to event horizons has its roots in the singularity theorems by Penrose and Hawking [48, 49, 79]. In his proof [79], Penrose introduced *trapped surfaces* defined in a *Cauchy slice* of spacetime—a notion of an *instant of*

time. To understand trapped surfaces, consider light emanating in normal direction from a sphere in a flat spacetime. The light rays converge to the inside and diverge to the outside. A trapped surface is a closed smooth surface where the light rays are converging in both directions. Existence of a trapped surface in such a Cauchy slice was shown to imply existence of an inextendible causal geodesic, i.e. spacetime is singular. Later, Hawking [47] introduced *trapped regions*, the outer boundaries of which were called *apparent horizons.* Assuming weak cosmic censorship and reasonable energy conditions, an apparent horizon must be in the black hole region and thus be located inside the event horizon or lie on it [47]. In other words, existence of a trapped surface implies the existence of a black hole.

Since trapped surfaces and apparent horizons are defined locally in time, this laid the foundations for the application to dynamical situations. However, several important questions remained open. Will these apparent horizons evolve smoothly? Are the world tubes they trace out independent from the way that spacetime is foliated using Cauchy slices? Do they faithfully capture the dynamics of black holes, for example when two black holes merge?

In numerical relativity, it became customary to associate black holes with marginally outer trapped surfaces (MOTSs). These are similar to trapped surfaces, except that the outgoing light rays are neither diverging nor converging, and there is no condition on the ingoing light rays. They are hence *marginally outer trapped.* The term "apparent horizon" is now used for the outermost of these surfaces. Though originally used as pragmatic alternatives to event horizons, which are numerically inaccessible during a simulation, apparent horizons and closely related surfaces and their time evolution have been studied thoroughly. This led to the notion of *trapping horizons* by Hayward [50–53] and later to the introduction of the *quasilocal horizon formalism* by Ashtekar, Krishnan and others, see [20] for a review. In the latter, a dynamical horizon is defined as 3-dimensional world tube of evolving MOTSs, with two added conditions: 1) ingoing null rays converge and 2) the world tube is a spacelike hypersurface of spacetime.

Within this context, several of the above questions can be answered. For a given spacetime, the dynamical horizons are not unique and instead depend on the foliation. There are, however, certain restrictions on their locations, see e.g. [17, 67]. The MOTS stability analysis of Andersson, Marc and Simon [7, 8] showed smoothness of the time evolution, and the laws of black hole mechanics have successfully been transferred to the quasilocal framework [10–12, 14, 16, 18, 19]. The area balance law of Ashtekar and Krishnan [18, 19] connected physical fluxes through the horizons with their growth in an exact formula in full nonlinear general relativity.

Even though the horizons were seen to evolve smoothly, there remained a gap in the understanding of the merger of two black holes within the quasilocal paradigm. While an intuitive way to imagine such a merger is given via the event horizon in the famous "pair of pants" picture [71], no such connected history was available in terms of

dynamical horizons. At a certain point after the initially two disjoint horizons approach each other, a common horizon forms around them. This common horizon immediately splits into an inner and an outer one, see [46] for an example. While the outer horizon subsequently loses its deformations and asymptotes to a Kerr state, the inner branch could not be tracked for very long and the question of its fate remained open. This scenario resulted in ideas of how a connected history might form. In [75] and [46], it is suggested that the inner branch and the two individual horizons could merge and annihilate. Unfortunately, a fundamental issue inherent in most numerical approaches to locating the MOTSs prevented further progress and this question remained open. The problematic assumption is that MOTSs must be *star-shaped* ("Strahlkörper"), which means that in the numerical coordinates, we can choose a point from which the MOTS can be parametrized via a horizon function h representing the coordinate distance of the surface to this point.

The present numerical work closes the gap and provides the missing link [80–84]. For the case of a head-on collision of two non-spinning black holes of unequal masses, we show that the dynamical horizons do merge, yielding a connected sequence of MOTSs taking us from the initial two separate black holes to the final common one. This result required the implementation of a new numerical algorithm for locating MOTSs. It is based on the commonly used *AHFinderDirect* [95] but removes the assumption of the MOTSs being star-shaped. Instead of a *reference point*, the new method uses a suitable *reference surface* and the horizon function h now describes the coordinate distance to this surface along its normal direction.

Most of the results presented here will be for the axisymmetric case, in which the problem of finding MOTSs simplifies greatly. However, the method itself can be generalized to fully non-symmetric cases, and first results of this generalized version of the algorithm are shown at the end of this work.

With the ability to find highly distorted surfaces with high accuracy, an unexpected wealth of results even for just the axisymmetric case was produced. Among the more surprising ones are the formation of self-intersecting MOTSs, a non-monotonicity result for the area evolution along a smoothly evolving MOTS, unusual geometrical properties related to the expansion of the ingoing light rays and the signature of the horizons, as well as an unexpectedly direct correspondence between the decay behavior of infalling gravitational radiation through the outermost horizon and the quasi-normal modes of a Schwarzschild black hole. The general occurrence of such correlations is not unexpected and it suggests the possibility of connecting the horizon dynamics of merging black holes with observations made far away (see e. g. [42, 43, 46, 58, 61, 62, 86, 88]).

Since the merger of MOTSs and the existence of self-intersecting MOTSs are new phenomena not previously described, much focus will be put on justifying the reliability of the numerical indications we have for these results. In this context it is noteworthy

that self-intersecting MOTSs have also been found by Booth et al. [29], who showed that in slices of a Schwarzschild spacetime there exist MOTSs with arbitrarily many self-intersections.

The remainder of this thesis is organized as follows. First, a precise attribution of the author's contributions is given in Sec. 1.1. Chapter 2 will introduce the basic mathematical notions required for the machinery of the quasilocal horizon framework. In particular, the terminology used throughout this work deviates in one key aspect from the usual one: Since the horizons we find occur in a much larger variety than usually considered, the term "dynamical horizon" will be used as in [80, 81] and refer to a more general case. The chapter continues with a geometric construction of coordinates on axisymmetric surfaces and then presents an important mathematical concept for our analyses, the MOTS stability operator introduced by Andersson et al. [7, 8]. It concludes with a brief discussion of a possible application of our results to a certain version of the Penrose inequality.

Chapter 3 introduces the new numerical algorithm and details the mathematical and practical steps needed to achieve highly accurate results. After the general idea of a surface representation suitable for a pseudospectral method of solving the nonlinear horizon problem, it will present several important improvements specific to the axisymmetric implementation. Finally, the new method is validated using analytically known horizon data.

The first set of main results is given in Chapter 4. This chapter focuses on a family of time-symmetric initial data containing two non-spinning black holes. It is parametrized by the mass ratio of the black holes and the distance parameter, both of which will be varied, yielding an unexpectedly rich variety of different horizon configurations. After a basic overview, we give an analysis of the connection between the MOTS stability operator and the vanishing of MOTSs in certain regions of the parameter space.

The most important results are presented in Chapter 5, where we determine the MOTS structure in numerical simulations of the head-on collision of two black holes. We first show the general evolution of the different horizons, including the merger of MOTSs and the occurrence of self-intersecting MOTSs. After a description of how the simulations are performed, the additional challenges of working with data on a finite set of grid points are discussed and a thorough analysis of the numerical convergence is given. This is followed by a detailed analysis of the numerical indications for the merger of MOTSs The results for geometrical properties, in particular the expansion of the ingoing light rays and the signature of the horizons, are then connected with the area anomaly of the inner horizon. A large part is played by the spectra of the MOTS stability operator, with a focus on the low eigenvalues demonstrating existence of the various world tubes, and an attempt at a global analysis using a short-range spectrum statistic called the nearest neighbor spacing distribution. This chapter is concluded with a study of the fluxes of gravitational radiation through the horizons.

The shear and multipole moments are compared with quasi-normal modes, revealing a direct correspondence with the different frequencies of the fundamental mode.

Chapter 6 shows a proof-of-concept of a generalized MOTS finder algorithm which works in non-axisymmetric settings and presents an example demonstrating that the method is applicable for this general case.

Finally, Chapter 7 concludes this thesis by summarizing the results and discussing possible future research.

1.1 Contributions of the Author

Since the results presented in this dissertation are based on the work of several authors, a clear attribution of the author's own contributions is in order. Most of the presented results have been published [82–84] or submitted [80, 81], a notable exception being the generalized algorithm discussed in Chapter 6. The following list gives a detailed account of the technical contributions.

- *MOTS Finder:* The new MOTS finder algorithm [85] has been devised and written by the author, with numerical and programming questions discussed with Ofek Birnholtz, Badri Krishnan and Erik Schnetter. The code is written in a combination of Python for the majority of the work, with certain parts being implemented in Cython. The libraries *SciPy* [98], *NumPy* [96], *SymPy* [73], *mpmath* [64], *spinsfast* [33] and *matplotlib* [38, 56], were used for most of the low-level numerical tasks, like solving systems of linear equations for the written pseudospectral solver, for working with large matrices, or for plotting tasks.

- *Numerical Simulation Data:* Most numerical simulations were initiated and supervised by Erik Schnetter using the *Einstein Toolkit* [39, 69] (see Chapter 5.2 for details). However, interpretation of the resulting data on the numerical grid, including their interpolation via Lagrange and Hermite interpolation, was implemented by the author.

- *MOTS Stability Operator:* The mathematical and numerical work required to compute the eigenvalues and eigenfunctions of the stability operator was performed by the author. Mathematical suggestions related to the mode decomposition in φ direction were contributed by José Luis Jaramillo. Supervised by the author, a numerical transformation of the stability operator was provided by Victor Zhang.

- *Physical quantities:* Many of the other computed properties of the MOTSs and dynamical horizons (e. g. intrinsic Ricci scalar, invariant coordinates, shear, multipoles, signature) were mathematically prepared and then implemented

by the author. For several of these, new algorithms were created to perform, e. g., numerical searches for self-intersections or construction of highly accurate tangent vectors to the dynamical horizon which are orthogonal to the MOTSs.

- *Analyses:* All the analyses that led to the presented results were carried out by the author. This includes implementing and supervising a horizon tracker which uses the finder to follow horizons through simulations or families of initial data.

- *Numerical algorithms:* For some mathematical computations, existing tools in the used libraries turned out to not be sufficient in either performance or accuracy. For this reason, an efficient implementation of the synthesis and analysis of spherical harmonic series was implemented in Cython using recursion relations and other formulas described in [54, 74].

Throughout the projects in the context of this thesis, discussions with the other members of our research group (i. e. the authors of [80–84]) and the author's supervisors and colleagues (and all those mentioned in the acknowledgement) provided important ideas and suggestions.

Chapter 2

Black Hole Horizons

This section will collect a set of basic geometrical constructs which will enable us to define various kinds of *trapped* and *marginally trapped* surfaces. These surfaces will play a fundamental role in the quasilocal definitions of black hole horizons and present the foundation upon which the remainder of this thesis is built. This quite terse and technical part will at the same time introduce the notation and conventions used throughout.

Spacetime $(\mathscr{M}, g)$ is a four-dimensional smooth manifold $\mathscr{M}$ with a Lorentzian metric $g_{\mu\nu}$ of signature $(-+++)$. The term *"surface"* will denote an orientable smooth two-dimensional spacelike submanifold of $\mathscr{M}$. We will use lowercase Greek letters $\mu, \nu, \rho, \ldots$ for the four spacetime indices, lowercase Latin letters $i, j, k, \ldots$ for the three "spatial" coordinates and uppercase Latin letters $A, B, C, \ldots$ for indices of coordinates on a surface $\mathcal{S} \subset \mathscr{M}$.

2.1 Trapped Surfaces

Let now $\mathcal{S} \subset \mathscr{M}$ be a closed surface with induced Riemannian metric q_{AB}. At any point $p \in \mathcal{S}$, the four-dimensional tangent space $T_p\mathscr{M}$ can be decomposed into the direct sum $T_p\mathscr{M} = T_p\mathcal{S} \oplus T_p\mathcal{S}^\perp$, where $T_p\mathcal{S}$ is the tangent space of $\mathcal{S}$ at the point $p \in \mathcal{S}$ and $T_p\mathcal{S}^\perp$ is the space of vectors orthogonal to any vector in $T_p\mathcal{S}$, i.e. the space of *normals* to $\mathcal{S}$. This space can be spanned by two future directed linearly independent null vectors, which we will call ℓ^μ and n^μ. We further assume that it is possible to assign an *outward* direction on $\mathcal{S}$ and will, by convention, take ℓ^μ and n^μ to be pointing outward and inward, respectively. The freedom of scaling ℓ^μ and n^μ by positive functions is reduced by requiring $\ell \cdot n = -1$. This yields an expression for the induced metric q_{AB}:

$$q_{\mu\nu} := (P^{\parallel}g)_{\mu\nu} = g_{\mu\nu} + \ell_\mu n_\nu + n_\mu \ell_\nu \,, \tag{2.1}$$

where $P^{\parallel}$ is the parallel projection onto the tangent space of $\mathcal{S}$. Acting on a vector field X^{μ}, the projection $P^{\parallel}X$ can be written in components as

$$(P^{\parallel}X)^{\mu} = q^{\mu}_{\nu}X^{\nu}\,. \tag{2.2}$$

This leads to the definition of the tensor field

$$\Theta^{(\ell)}_{\mu\nu} = q^{\alpha}_{\mu}q^{\beta}_{\nu}\nabla_{\alpha}\ell_{\beta}\,, \tag{2.3}$$

where ∇_{μ} is the covariant derivative compatible with $g_{\mu\nu}$. This tensor can be decomposed into a trace, a tracefree symmetric, and an antisymmetric part:

$$\Theta^{(\ell)}_{\mu\nu} = \frac{1}{2}\Theta_{(\ell)}q_{\mu\nu} + \sigma^{(\ell)}_{\mu\nu} + \omega^{(\ell)}_{\mu\nu}\,. \tag{2.4}$$

Here, $\Theta_{(\ell)} := q^{\mu\nu}\Theta^{(\ell)}_{\mu\nu}$ is the *expansion* of ℓ^{μ}, the symmetric tracefree tensor $\sigma^{(\ell)}_{\mu\nu} := \Theta^{(\ell)}_{\mu\nu} - \frac{1}{2}\Theta_{(\ell)}q_{\mu\nu}$ is the *shear*, and $\omega^{(\ell)}_{\mu\nu}$ the *twist*. The twist will vanish in our case because the field ℓ^{μ} is orthogonal to a smooth surface. The same construction can be repeated for the ingoing future pointing null normal n^{μ}, yielding

$$\Theta^{(n)}_{\mu\nu} = \frac{1}{2}\Theta_{(n)}q_{\mu\nu} + \sigma^{(n)}_{\mu\nu} + \omega^{(n)}_{\mu\nu}\,. \tag{2.5}$$

Since we will be mostly concerned with the shear of the outgoing null normal, $\sigma^{(\ell)}_{\mu\nu}$, we will drop the superscript and simply write $\sigma_{\mu\nu}$.

The conventional classification of $\mathcal{S}$ in terms of the expansions $\Theta_{(\ell)}$ and $\Theta_{(n)}$ is as follows.

Definition 1. A closed surface $\mathcal{S}$ is called a

1. *(future) trapped surface* if $\Theta_{(n)} < 0$ and $\Theta_{(\ell)} < 0$
   past trapped surface if $\Theta_{(n)} > 0$ and $\Theta_{(\ell)} < 0$

2. *(future) untrapped surface* if $\Theta_{(n)} < 0$ and $\Theta_{(\ell)} > 0$
   past untrapped surface if $\Theta_{(n)} > 0$ and $\Theta_{(\ell)} > 0$

3. *(future) marginally trapped surface* (MTS) if $\Theta_{(n)} < 0$ and $\Theta_{(\ell)} = 0$
   past marginally trapped surface if $\Theta_{(n)} > 0$ and $\Theta_{(\ell)} = 0$

4. *marginally outer trapped surface* (MOTS) if $\Theta_{(\ell)} = 0$ with no restriction on $\Theta_{(n)}$.

Each of the above conditions must hold on all points of $\mathcal{S}$. Note that the qualifier "future" is usually implied and hence omitted[1] (although in cosmological contexts it

---

[1]Case 3 is sometimes also referred to as "future/past marginally *outer* trapped surface". Here, the qualifier "future" cannot be omitted in order to keep cases 3 and 4 distinguishable.

becomes important).

Let spacetime $\mathscr{M}$ be foliated by spacelike hypersurfaces Σ_t. The label t becomes a coordinate ("time") on $\mathscr{M}$ via $t(p) = s \Leftrightarrow p \in \Sigma_s$. The unit timelike normal field on Σ_t will be denoted T^μ, i.e. we have $X^\mu T_\mu = 0$ for any $X \in T_p\Sigma_t$ and $T^\mu T_\mu = -1$. We shall choose T^μ future pointing by demanding $T^\mu \partial_\mu t > 0$. We can then write the vector field ∂_t with components $(\partial_t)^\mu$ using the usual decomposition into a *lapse* function α and the *shift* vector field β^μ:

$$(\partial_t)^\mu = \alpha T^\mu + \beta^\mu \,. \tag{2.6}$$

See e. g. [21, 44] for more details on the $3 + 1$ decomposition of spacetime. Further, we shall use h_{ij} to refer to the induced Riemannian 3-metric on the slice Σ_t and D_i for the covariant derivative operator compatible with h_{ij}. The second fundamental form of Σ_t, i.e. the extrinsic curvature of Σ_t in $\mathscr{M}$, is defined by

$$K_{\mu\nu} := -h^\rho_\mu h^\sigma_\nu \nabla_\rho T_\sigma \,. \tag{2.7}$$

If $\mathcal{S}_t$ is a surface contained in Σ_t, let R^μ denote the unit spacelike normal to $\mathcal{S}_t$ in Σ_t. One convenient choice of null normals in terms of the quantities introduced above is

$$\ell^\mu = \frac{1}{\sqrt{2}}(T^\mu + R^\mu)\,, \qquad\qquad n^\mu = \frac{1}{\sqrt{2}}(T^\mu - R^\mu)\,. \tag{2.8}$$

Fig. 2.1 shows a diagram indicating the various normals introduced here. One can then show that [45]

$$\Theta_{(\ell)} = \frac{1}{\sqrt{2}}(D_i R^i + K_{ij}R^i R^j - K)\,, \quad \Theta_{(n)} = \frac{1}{\sqrt{2}}(-D_i R^i + K_{ij}R^i R^j - K)\,, \tag{2.9}$$

where the normal R^μ has to be smoothly extended to a neighborhood of $\mathcal{S}$ in Σ_t (the result does not depend on how it is continued). The remarkable property of these equations is that they can be easily evaluated numerically for a surface $\mathcal{S}$ knowing *only* the data h_{ij} and K_{ij} on the Cauchy slice Σ_t, as we do in numerical relativity.

Note that there is still a remaining freedom to rescale ℓ^μ and n^μ by positive functions
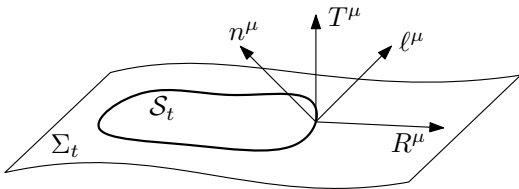
Figure 2.1: Visualization of the various introduced normals for a 2-surface $\mathcal{S}_t$ contained in a spatial slice Σ_t. The 3-dimensional slice is here represented with 2-dimensions.

9

f via

$$\widetilde{\ell}^{\mu} = f\ell^{\mu}\,, \qquad\qquad \widetilde{n}^{\mu} = f^{-1}n^{\mu}\,. \qquad\qquad (2.10)$$

This retains the condition $\widetilde{\ell} \cdot \widetilde{n} = -1$ but results in a change of the expansions

$$\Theta_{(\widetilde{\ell})} = f\Theta_{(\ell)}\,, \qquad\qquad \Theta_{(\widetilde{n})} = f^{-1}\Theta_{(n)}\,. \qquad\qquad (2.11)$$

Hence, the above classification of $\mathcal{S}$ in terms of the two expansions $\Theta_{(\ell)}$ and $\Theta_{(n)}$ is independent of the choice of null normals.

2.2 Quasilocal Horizons

Stacking up a series of MOTSs contained in slices Σ_t leads to the notion of a dynamical horizon $\mathcal{H}$.

Definition 2 (Dynamical Horizon)**.** Let $\mathcal{H} \subset \mathcal{M}$ be a smooth 3-dimensional hypersurface with topology $S^2 \times \mathbb{R}$. Then $\mathcal{H}$ is called a *dynamical horizon (DH)* if it admits a foliation by MOTSs $\mathcal{S}$.

Traditionally, these objects are called *marginally outer trapped tubes* (MOTTs) and a dynamical horizon is in addition required to have spacelike signature and be foliated by marginally trapped surfaces (i.e. having $\Theta_{(n)} < 0$ everywhere). However, as we shall see in Chapter 5, we will encounter MOTTs with not only spacelike but also timelike and even mixed signature, as well as cases not satisfying $\Theta_{(n)} < 0$ everywhere. Instead of adding multiple qualifiers to an acronym and reserving the term "dynamical horizon" to one special case, we will therefore follow [80, 81] and change the usual terminology in favor of more descriptive names. In particular, we can identify the following correspondences:

- A generic *MOTT* will here be called a *dynamical horizon*.

- A *marginally trapped tube (MTT)* is a *future dynamical horizon*.

- A *dynamical horizon* (as used in e.g. [18, 19]) is here called a *future spacelike dynamical horizon*.

- A *non-expanding horizon (NEH)* is a dynamical horizon $\mathcal{H}$ with null signature and the following additional condition: The Einstein field equations hold on $\mathcal{H}$ and $-T^{\mu}_{\nu}\ell^{\nu}$ is future directed and causal if ℓ^{μ} is future directed. Here, $T_{\mu\nu}$ is the stress energy tensor and ℓ^{μ} any null normal to $\mathcal{H}$. This latter condition is implied by e.g. the dominant energy condition.

A subclass of non-expanding horizons is that of *isolated horizons.* These need to satisfy additional requirements, which we will not introduce here. See [20] for the exact definition.

The question of uniqueness touched upon in the introduction is discussed in [67] with important results shown in [17]. In essence, in [17] it is shown that for a future spacelike dynamical horizon $\mathcal{H}$, the foliation via MOTSs is unique. Let now $\mathcal{S} \subset \mathcal{H}$ be a MOTS, with $\mathcal{S} \subset \Sigma_0$. The question of whether $\mathcal{S}$ evolves smoothly through a foliation that contains Σ_0 will be discussed below in Sec. 2.4. Given this is the case, then a dynamical horizon exists, at least for a short time, in *any* foliation containing Σ_0. Slices away from Σ_0 will, however, in general not contain the same MOTSs that foliate $\mathcal{H}$. Hence, the dynamical horizons must be different hypersurfaces in spacetime. Fortunately, there are restrictions as to how much two different of these dynamical horizons can deviate from each other. However, the present work will not contribute to these questions and the reader is referred to [17, 67] instead.

2.3 Invariant Coordinates in Axisymmetry

It will be helpful for several calculations and for presenting results to have access to invariant coordinates on a MOTS $\mathcal{S}$, i.e. coordinates that do not depend on a particular numerical representation. In fact, this will be crucial for defining the multipolar decomposition of certain fields on the horizons, which we shall discuss in great detail in Chapter 5, in particular Sec. 5.7. Fortunately, this is easy to do in axisymmetry, following [15]. In our case, we will have manifest axisymmetry with a readily available axial Killing field φ^A preserving the induced 2-metric q_{AB} on $\mathcal{S}$. This field has closed orbits and vanishes at two points of $\mathcal{S}$—the two "poles". We can now define a coordinate ζ via

$$\mathcal{D}_A \zeta = \frac{4\pi}{A} \epsilon_{BA} \varphi^B \,, \qquad\qquad \int_{\mathcal{S}} \zeta \, dA = 0 \,, \qquad (2.12)$$

where ϵ_{AB} is the volume 2-form on $\mathcal{S}$ and A its area. For a round sphere in flat space, $\zeta = \cos\theta$ for the usual polar angle θ. Even for distorted surfaces $\mathcal{S}$, it can be shown that $\zeta \in [-1, 1]$ and hence we can set $\theta := \arccos \zeta$. Note, however, that θ will not correspond to an "angle" in the traditional sense for very distorted surfaces. For example, it is well defined even if $\mathcal{S}$ has self-intersections. The other angular coordinate ϕ can now be defined as affine parameter along the orbits of φ^A. We can take the φ^A such that $\phi \in [0, 2\pi)$ on $\mathcal{S}$. Setting $\phi = 0$ along any one fixed integral curve of $\mathcal{D}^A \zeta$ fully determines the ϕ coordinate on $\mathcal{S}$.

A key result of [15] is now that in the coordinates (θ, ϕ), the volume element of the induced 2-metric q_{AB} on $\mathcal{S}$ becomes *identical* to that of a canonical round 2-sphere

metric

$$q_{AB}^{(0)} = R^2 \left(d\theta^2 + \sin^2\theta \; d\phi^2 \right) . \tag{2.13}$$

Again, $R = \sqrt{A/4\pi}$ is the areal radius of $\mathcal{S}$. This means that spherical harmonics written in terms of the coordinates (θ, ϕ) will automatically satisfy the usual orthogonality relations. In the same way, we can construct spin weighted spherical harmonics and perform a geometrically defined decomposition of fields on horizons.

2.4 The MOTS Stability Operator

Consider a MOTS $\mathcal{S}$ contained in a Cauchy slice Σ. Is it possible to tell whether $\mathcal{S}$ is a leaf of a dynamical horizon $\mathcal{H}$? In other words, can we determine the conditions, under which $\mathcal{S}$ has a smooth time evolution in a foliation of spacetime containing Σ? In 2005, Andersson, Mars and Simon [7] found an answer to this question in the affirmative. By calculating the eigenvalue spectrum of a second order, elliptic, not necessarily self-adjoint operator, existence of the dynamical horizon can be shown, at least locally in time, by a simple criterion. If zero is not contained in the spectrum, i. e. if the operator is invertible, there will be a smooth evolution. The analysis of this spectrum in families of initial data as well as in numerical simulations will be a major topic in this thesis. In this subsection, this stability operator is introduced and the main results important for our analysis are stated.

The general construction leading to the definition of the stability operator can easily be visualized as follows. Consider a smooth one-parameter family of surfaces $\mathcal{S}_\sigma$ such that $\mathcal{S}_{\sigma=0} = \mathcal{S}$. For definiteness, this family shall be constructed from a differentiable map $\Phi : \mathcal{S} \times I \to \mathcal{M}$, where $I = (-\varepsilon, \varepsilon)$ is an interval containing 0, and where we set $\mathcal{S}_\sigma := \Phi(\mathcal{S}, \sigma)$. For fixed σ, $\Phi(\,\cdot\,, \sigma)$ shall be an immersion and $\Phi(\mathcal{S}, 0) = \mathcal{S}$. Note that we make no reference to any spatial slice the surface $\mathcal{S}$ is contained in, whence the surfaces $\mathcal{S}_\sigma$ need not lie in the same spatial slice Σ_t as $\mathcal{S}$. On the other hand, fixing a point $p \in \mathcal{S}$ yields a curve $\sigma \mapsto \Phi(p, \sigma)$. The tangent vector X_p^μ to this curve is then given by

$$X_p^\mu = \left. \frac{\partial}{\partial \sigma} \right|_{\sigma=0} \Phi^\mu(p, \sigma) . \tag{2.14}$$

We are now able to define the variation of $\Theta_{(\ell)}$ on $\mathcal{S}$. To this end, construct null normal fields ℓ_σ^μ on $\mathcal{S}_\sigma$ which are differentiable with respect to σ. Their expansions $\Theta_{(\ell_\sigma)}$ then yield the variation of $\Theta_{(\ell)}$ along X^μ via

$$\delta_X \Theta_{(\ell)} := \left. \frac{\partial}{\partial \sigma} \right|_{\sigma=0} \Theta_{(\ell_\sigma)} . \tag{2.15}$$

It is shown in [8] that this is indeed fully characterized by the vector fields X^μ and ℓ^μ

on $\mathcal{S}$ and is independent of the particular map Φ or choice of ℓ_σ^μ for $\sigma \neq 0$. Clearly, if X^μ is tangent to $\mathcal{S}$, the variation (2.15) vanishes. We therefore consider only deformations in normal direction, i.e. we take

$$X^\mu = b\ell^\mu + cn^\mu \,. \tag{2.16}$$

The variation (2.15) is obviously $\mathbb{R}$-linear,

$$\delta_{aX+bY}\Theta_{(\ell)} = a\delta_X\Theta_{(\ell)} + b\delta_Y\Theta_{(\ell)} \,, \tag{2.17}$$

for $a, b \in \mathbb{R}$, but it is not $\mathbb{C}^\infty$-linear. That is, in general we have

$$\delta_{\psi X}\Theta_{(\ell)} \neq \psi\delta_X\Theta_{(\ell)} \,, \tag{2.18}$$

where ψ is a function on $\mathcal{S}$. Finally, we can define the stability operator.

Definition 3 (MOTS Stability Operator)**.** Let $\mathcal{S}$ be a MOTS with future pointing outgoing null normal field ℓ^μ and X^μ a normal field on $\mathcal{S}$. The *stability operator $L^{(X)}$* with respect to X^μ is then defined via

$$L^{(X)}\psi := \delta_{\psi X}\Theta_{(\ell)} \,. \tag{2.19}$$

For $X^\mu = \ell^\mu$, one can show [8] that in vacuum spacetimes we have

$$L^{(\ell)}\psi = \delta_{\psi\ell}\Theta_{(\ell)} = -2|\sigma|^2\psi \,, \tag{2.20}$$

where $|\sigma|^2 := \sigma_{\mu\nu}\sigma^{\mu\nu}$. To construct $L^{(X)}$ for a general normal $X^\mu = b\ell^\mu + cn^\mu$, we furthermore need

$$L^{(-n)}\psi = \left(-\Delta_\mathcal{S} + 2\omega^A\mathcal{D}_A\right)\psi + \left(\frac{1}{2}\mathcal{R} + \mathcal{D}_A\omega^A - \omega_A\omega^A\right)\psi \,. \tag{2.21}$$

Here, $\mathcal{D}_A$ is the covariant derivative compatible with the induced metric q_{AB}, $\Delta_\mathcal{S}$ and $\mathcal{R}$ are the Laplacian and Ricci scalar of $\mathcal{S}$, respectively, and $\omega_\mu := -q_\mu^\nu n_\rho \nabla_\nu \ell^\rho$.

The stability operator associated with the slice Σ is obtained by taking X^μ in the direction of the normal R^μ of $\mathcal{S}$ within Σ. Making use of the freedom to scale the operator by a constant to simplify further expressions, we consider

$$\sqrt{2}R^\mu = \ell^\mu - n^\mu \,, \tag{2.22}$$

and define

$$L_\Sigma \psi := L^{(\sqrt{2}R)}\psi = \left(-\Delta_{\mathcal{S}} + 2\omega^A \mathcal{D}_A\right)\psi$$
$$+ \left(\frac{1}{2}\mathcal{R} - \omega_A\omega^A + \mathcal{D}_A\omega^A - 2|\sigma|^2\right)\psi. \tag{2.23}$$

The operators $L^{(n)}$ and L_Σ are second order elliptic operators defined on the compact manifold $\mathcal{S}$ and thus have a discrete spectrum. Furthermore, under the rescalings (2.10), the expressions (2.21) and (2.23) transform such that the spectrum remains invariant [59].

An important result in [7, 8] is that the invertibility of L_Σ implies smoothness of the time evolution. This is numerically discussed in [81–84]. In general, L_Σ is not self-adjoint due to the $2\omega^A \mathcal{D}_A$ term. However, the principal eigenvalue Λ_0, defined as the eigenvalue with smallest real part, can be shown to be real. If it is positive, no other eigenvalue can be zero and invertibility is guaranteed.

There is an interesting connection between the principal eigenvalue and the behavior of a MOTS under small outward deformations. The following definition allows us to state the precise result.

Definition 4 (Strictly Stably Outermost)**.** Let $\mathcal{S}$ be a MOTS with normal R^μ in a slice Σ. Then $\mathcal{S}$ is called *strictly stably outermost* if and only if there exists a non-negative function $\psi \not\equiv 0$ on $\mathcal{S}$ such that $\delta_{\psi R}\Theta_{(\ell)} \geq 0$ with at least one point satisfying $\delta_{\psi R}\Theta_{(\ell)} > 0$.

It is shown in [7] that a MOTS $\mathcal{S}$ is strictly stably outermost if and only if $\Lambda_0 > 0$. Furthermore, a strictly stably outermost MOTS $\mathcal{S}$ has a neighborhood U such that no smooth surface $\mathcal{S}_+ \subset U$ with $\Theta_{(\ell)} \geq 0$ can enter the interior of $\mathcal{S}$ and no smooth surface $\mathcal{S}_- \subset U$ with $\Theta_{(\ell)} \leq 0$ can enter the exterior of $\mathcal{S}$.[2]

A useful simplification for the practical purpose of evaluating the spectrum numerically is the following. In axisymmetry, with the coordinates (θ, ϕ) on $\mathcal{S}$ introduced in Sec. 2.3, we can expand the ϕ dependence of ψ into a Fourier basis,

$$\psi(\theta, \phi) = \sum_{m=-\infty}^{\infty} \psi_m(\theta)\, e^{im\phi}. \tag{2.24}$$

All ϕ derivatives occurring in $L^{(X)}$ can therefore be carried out analytically, reducing the spectral problem to the following one-dimensional one:

$$L_m^{(X)}\psi_m = \left(L_\Sigma + 2im\omega^\phi + m^2 q^{\phi\phi}\right)\psi_m. \tag{2.25}$$

---

[2]To avoid pathological cases, one needs to add the condition that there must exist a smooth deformation of $\mathcal{S} \to \mathcal{S}_+$ (or $\mathcal{S} \to \mathcal{S}_-$) completely contained in U.

No summation over m is implied here. Instead, we solve the spectral problem for a fixed integer m and repeat this procedure for various values of m.

All configurations considered in this thesis will be axisymmetric and with no angular momentum. In these cases, it is possible to scale the null normal ℓ^μ such that ω_A vanishes.[3] This leaves the spectrum of $L^{(X)}$ invariant and yields the self-adjoint operators

$$L^{(-n)}\psi = \left(-\Delta_\mathcal{S} + \frac{1}{2}\mathcal{R}\right)\psi \tag{2.26}$$

and

$$L_\Sigma\psi = \left(-\Delta_\mathcal{S} + \frac{1}{2}\mathcal{R} - 2|\sigma|^2\right)\psi\,. \tag{2.27}$$

Note that due to $\omega_A = 0$ in this case, the effective one-dimensional problem (2.25) depends on m only via m^2, resulting in a $\pm m$ degeneracy for $m \neq 0$. With the spectrum being real, we will label the eigenvalues Λ by two integers via $\Lambda_{l,m}$, where we shall call m the *angular mode* fixed in Eq. (2.25). The number l is then assigned to the resulting set of values in ascending order

$$l = |m|, |m| + 1, |m| + 2, \dots, \tag{2.28}$$

which leads to a labeling of eigenvalues consistent with those we find for a round sphere.

To see this, we will now determine the spectrum of a round sphere $\mathcal{S}$ with negligible contributions of the $|\sigma|^2$ term. This can later be compared with the spectra we find on actual MOTSs especially for the case when they approach or originate from such a state. For a round sphere of radius R, the Ricci scalar is just $\mathcal{R} = 2/R^2$. This is also the value of $\mathcal{R}$ for a Schwarzschild horizon of areal radius $R = \sqrt{A/4\pi}$, where A is the surface area of a cross section of the horizon. The spectrum of the stability operators is then given by the spectrum of the Laplacian on the sphere, shifted by the constant $1/R^2$, i. e. we have

$$\Lambda_{l,m} = \frac{1}{R^2}(1 + l(l+1))\,, \tag{2.29}$$

where (l, m) label the eigenvalues and run through $l = 0, 1, \dots$ and $m = -l, \dots, l$, respectively. Thus, the eigenvalue l is $(2l + 1)$-fold degenerate.

---

[3]From [60, eq. (4)], we know that we can always scale the null normals ℓ^μ and n^μ such that ω_A is divergence free. After this rescaling, ω_A is related to the angular momentum [63] and will be zero in all cases considered here.

2.5 The Penrose Inequality in a Black Hole Merger

One possible application of the quasilocal horizon framework concerns one of the open problems of mathematical relativity, namely the Penrose inequality [78]. See also [70] for a general review.

This inequality reads

$$A \leq 16\pi M^2 \tag{2.30}$$

and it bounds a "suitable" surface A of a section of a black hole with a Cauchy slice Σ by the Arnowitt Deser Misner (ADM) mass of the spacetime. Different choices for this surface can be considered, with $A = A_{\min}$ being the most promising candidate for a general proof. Here $A_{\min}$ is defined as the infimum of the areas of all surfaces enclosing the apparent horizon in Σ. In the original argument of Penrose, a fundamental assumption is the weak cosmic censorship conjecture, which states that all singularities are hidden from observers at infinity by an event horizon. It was since the goal to prove this inequality without cosmic censorship.

For the case that Σ is time symmetric, i. e. its extrinsic curvature vanishes, and the dominant energy condition is satisfied, the inequality was proven for A being the area of the apparent horizon itself. This version of the inequality is called the *Riemannian Penrose inequality* and the proof of Huisken and Ilmanen [55] for the case that the horizon has one component was later followed by Bray [34] for the case of multiple components.

A result due to Ben-Dov [22] showed by an explicit counter example that without time symmetry, (2.30) cannot be proven for A being the apparent horizon area. However, instead of general apparent horizons, consider now leaves of future spacelike dynamical horizons $\mathcal{H}$. For this case, Ashtekar and Krishnan suggest in [18] that the monotonicity of the area evolution along $\mathcal{H}$ may help proving a version of this inequality. An important ingredient is the fact that if the final state of $\mathcal{H}$ is an isolated horizon extending to timelike infinity i^+, then the horizon mass will tend to the asymptotic value of the Bondi mass, provided that suitable regularity conditions hold [11]. By the positivity of the energy flux through null infinity $\mathscr{I}^+$ [28, 89], the Bondi mass is bounded from above by the ADM mass, whence this suggested version of the inequality is even stronger than the original one. Note that in this argument, no use is made of the event horizon and of weak cosmic censorship.

The question relevant for the present work is now whether this suggestion is applicable for the case of a binary black hole merger. Provided the final common horizon becomes an isolated horizon and does extend to i^+, the above argument would apply to the initial two separate horizons of the individual black holes and to the final common horizon, but not directly in the very dynamic merger regime. For this, one needs to control the area evolution across the merger. Our results [83, 84] may help at exactly this

point, since we do find a connected history of the dynamical horizons numerically, see Chapter 5. However, despite the powerful monotonicity results of Bousso & Engelhardt [30, 31], the question cannot be settled completely. The results shown here in Chapter 5 and in [80] will demonstrate that the area is not fully monotonic across this history due to certain properties of the involved horizons, which will be discussed in great detail. Provided an understanding of this small "area anomaly" can be achieved, the applicability of the suggestion in [18] should be reevaluated.

Chapter 3

Numerical Method

This chapter describes the new numerical algorithm which is able to accurately find MOTSs even when they are highly distorted. Our method has first been described in [82] with certain details discussed in [84]. The need for an extension of previous methods rarely arises for the outermost MOTS in a given slice, as it is found in practice to be "round" enough in the numerical coordinates to not present a problem for common algorithms. However, in order to understand the geometry of the dynamical horizons involved, and to resolve the merger of these horizons, we need to be able to numerically track not only the outermost MOTSs, but also the *inner* horizons that may form. These are seen to become highly distorted and cannot be tracked with the usual methods for very long before they disappear, see e. g. [46, 75].

The technical reason for this is an ubiquitous assumption of how the MOTS $\mathcal{S}$ can be represented numerically. Using a suitable reference point, $\mathcal{S}$ is usually described by a horizon function h encoding the coordinate distance to this point. Surfaces that can be represented this way are called "star-shaped" surfaces or "Strahlkörper".

The advantage of this representation is that it solves the problem of numerically computing the surface normal R^i in the slice and its derivatives appearing in the expansion formula of Eq. (2.9). One uses the fact that the horizon $\mathcal{S}$ becomes the zero-level set of the function

$$F := r - h \,, \tag{3.1}$$

where r is the coordinate distance from the reference point and h the horizon function. The normal is computed using $s_i = D_i F$ and then normalized $R^i = s^i / \sqrt{s^j s_j}$. Eq. (2.9) then becomes an elliptic nonlinear partial differential equation for the horizon function h. Algorithms based on this concept are hence often called *elliptic-PDE* finders. Publicly available implementations are, for example, the often used *AHFinderDirect* by Thornburg [94] or *TGRapparentHorizon2D* by Schnetter [91, 92].

The basic idea of the new algorithm presented here is to use a *reference surface* instead of a reference point. This modifies the representation of the surface as well as the definition of the function F in Eq. (3.1), but retains most of the other aspects of these algorithms. In particular, the star-shaped version of the algorithm becomes the special case of taking a round sphere as reference surface.

The details of this method are discussed in the remainder of this chapter. Starting

with the new representation of surfaces in Sec. 3.1, the numerical implementation of the nonlinear search using a pseudospectral method is described in Sec. 3.2. Up to this point, the discussion is applicable to fully general cases without any symmetries. Sec. 3.3 then concentrates on the axisymmetric case, which is the focus of the present work, and presents several numerical techniques developed to enhance accuracy and aid in situations of highly distorted MOTSs. Finally, Sec. 3.4 validates the new algorithm using analytically solvable problems.

3.1 Representation of arbitrary smooth surfaces

In this section, we will introduce a representation of surfaces which removes the need to assume the surfaces to be star shaped. In fact, the representation is general enough to, at least in principle, represent any smooth immersion of a smooth surface of arbitrary topology, although in practice we will limit ourselves to immersions of the 2-sphere S^2.

The new idea naturally arises as generalization of the star-shaped parametrization in terms of a horizon function h. This function maps S^2, parametrized by, say, the two angles θ and φ of the usual spherical coordinates, to the coordinate distance $h(\theta, \varphi)$ between a reference point p_{ref} and a point $p \in \mathcal{S}$ on the represented surface $\mathcal{S}$, i.e.

$$p = \Phi^{-1}\Big(\Phi(p_{\text{ref}}) + h(\theta, \varphi)\, e_r\Big),\tag{3.2}$$

where $\Phi : U \subset \Sigma \to V \subset \mathbb{R}^3$ is a local chart of a slice Σ containing $\mathcal{S}$ with $\mathcal{S} \subset U$ and e_r is the usual radial unit vector. The dependence of e_r on θ, φ is implied. Instead of $\Phi(p_{\text{ref}})$, we can, in fact, take any point $x_{\text{ref}} \in \mathbb{R}^3$ as reference point, even if $x_{\text{ref}} \notin V$, provided that $x_{\text{ref}} + he_r \in V$.

We will henceforth assume that a particular chart Φ has been chosen and we will call its component functions (the *coordinates*) in the common way $x^i = x^1, x^2, x^3$, so that $\Phi(p) = x^i(p)\, e_i$, where $\{e_1, e_2, e_3\}$ is the canonical basis of $\mathbb{R}^3$. Where convenient and when no ambiguity can arise, we may also use the names x, y, z to refer to x^1, x^2, x^3, respectively. With such a chart fixed—as is common practice in the context of numerical relativity—we can express (3.2) in the more familiar form

$$x(\theta, \varphi) = x_{\text{ref}} + h(\theta, \varphi)\, e_r\,,\tag{3.3}$$

where $x \in \mathbb{R}^3$ now traces out the points of $\Phi(\mathcal{S})$, i.e. it represents $\mathcal{S}$ in coordinate space. Following common practice, we will henceforth identify points and surfaces in Σ with their coordinate representation. For example, we might state that the points x of Eq. (3.3) are points on the surface $\mathcal{S}$. Likewise, adding a displacement vector to a point is always defined to take place in the coordinate space of the fixed chart Φ.

The generalization, which eliminates the assumption that $\mathcal{S}$ is star shaped, consists of
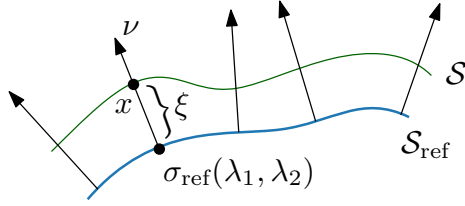
Figure 3.1: Visualization of the representation of a surface $\mathcal{S}$ using a reference shape $\mathcal{S}_{\text{ref}}$.

letting the reference point x_{ref} become a function of θ, φ. More formally, let $\sigma_{\text{ref}} : S^2 \to \mathbb{R}^3$ be an immersion and let $\lambda^A = \lambda^1, \lambda^2$ be coordinates on S^2 (e. g. the usual angles θ, φ). We shall call $\mathcal{S}_{\text{ref}} = \sigma_{\text{ref}}(S^2)$ the *reference surface* and σ_{ref} a parametrization of $\mathcal{S}_{\text{ref}}$. We now construct coordinates $\lambda^1, \lambda^2, \xi$ in a neighborhood of $\mathcal{S}_{\text{ref}}$ via

$$x(\lambda^1, \lambda^2, \xi) = \sigma_{\text{ref}}(\lambda^1, \lambda^2) + \xi \, \nu(\lambda^1, \lambda^2), \tag{3.4}$$

where ν is a fixed smooth nowhere vanishing vector field on the reference surface $\mathcal{S}_{\text{ref}}$ pointing in a direction transverse to $\mathcal{S}_{\text{ref}}$. Fig. 3.1 shows a visualization of this construction. It is numerically both convenient and efficient to construct ν by taking a field of normals (not necessarily normalized) in coordinate space.

We can now state how surfaces $\mathcal{S}$ are represented. Let $h : S^2 \to \mathbb{R}$ be a smooth function. We then define

$$\sigma(\lambda^1, \lambda^2) = x(\lambda^1, \lambda^2, h(\lambda^1, \lambda^2)) = \sigma_{\text{ref}}(\lambda^1, \lambda^2) + h(\lambda^1, \lambda^2) \, \nu(\lambda^1, \lambda^2). \tag{3.5}$$

This way, the surface $\mathcal{S} = \sigma(S^2)$ is written in terms of the coordinates (3.4) where we have set $\xi = h$. As a consequence, $\mathcal{S}$ is, in coordinate space, the zero-level set of the function

$$F(\lambda^1, \lambda^2, \xi) = \xi - h(\lambda^1, \lambda^2). \tag{3.6}$$

With this definition of F replacing the analog definition (3.1) in the previous star-shaped methods, one can in principle return to these methods and employ the existing numerical machinery to determine h.

Fig. 3.2 shows a simple example where the advantage of the reference-shape based representation over the star-shaped representation is easily seen. Note that here the reference shape $\mathcal{S}_{\text{ref}}$ is not very well adapted to the geometry of the represented surface $\mathcal{S}$ but still provides a clear advantage.
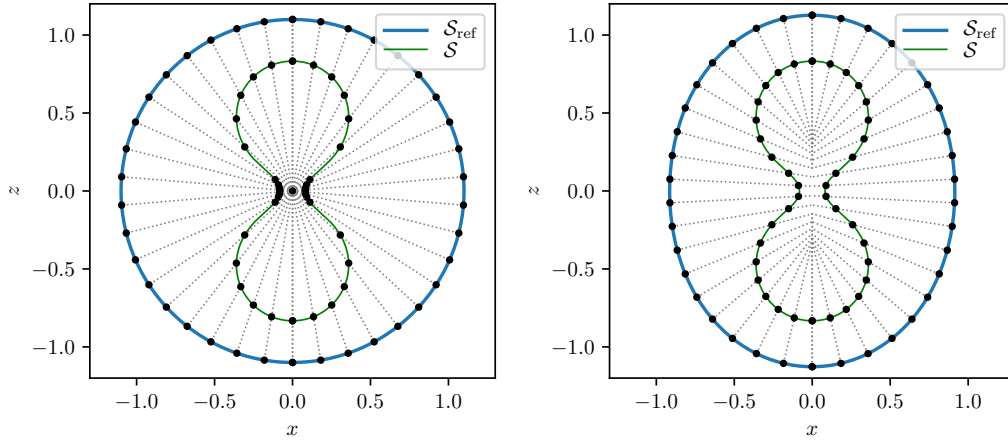
Figure 3.2: Effect of a star-shaped parametrization (left) and a parametrization based on a reference shape that is not a perfect sphere (right). The left panel shows a problematic accumulation of points near the central region with accompanying loss of resolution further away. This is alleviated by taking a suitable reference shape. In practice, the reference shape will be much closer to the target shape than shown in this example. (Figure adapted from [82].)

3.2 Numerical Implementation

One additional mathematical ingredient is required for an actual numerical implementation of an algorithm based on this new parametrization. In order to evaluate the surface normal $R^i = s^i / \sqrt{s^j s_j}$, we compute

$$s_i = D_i F = \partial_i F = \frac{\partial \xi}{\partial x^i} - \frac{\partial h}{\partial \lambda^A} \frac{\partial \lambda^A}{\partial x^i} \,, \tag{3.7}$$

where $A = 1, 2$. Below, we shall use u^a, $a = 1, 2, 3$, to refer to the coordinates $\lambda^1, \lambda^2, \xi$. Furthermore, we will use the abbreviations $u^a_{,i} = \frac{\partial u^a}{\partial x^i}$, $x^i_{,a} = \frac{\partial x^i}{\partial u^a}$ and extend this to higher derivatives in the obvious way.

On a first glance, it may seem as if (3.7) poses a problem since it involves derivatives of the new reference-shape based coordinates u^a with respect to the coordinates x^i, effectively requiring the inverse of the transformation (3.4). For fully general, numerically given, reference shapes σ_{ref}, it is nontrivial to find a highly accurate but still fast enough method for evaluating this inverse transformation as it generally involves numerical optimization. However, this problem can easily be avoided since the Jacobian of a coordinate transformation is the inverse of the Jacobian of the inverse transformation, i.e.

$$\left(u^a_{,i} \right) = \left(x^i_{,a} \right)^{-1} \,. \tag{3.8}$$

In order to evaluate the expansion $\Theta_{(\ell)}$ and its variational derivatives, the latter being needed for the strategy introduced below, we will need derivatives $\partial_i s_j$ and $\partial_i \partial_j s_k$. These can easily be obtained by differentiating (3.7). Higher derivatives of u^a, which occur in these expressions, are given by

$$u^a_{,ij} = -\, u^b_{,i} u^c_{,j} u^a_k x^k_{,bc} \tag{3.9}$$

$$u^a_{,ijk} = -\, \left[u^b_{,ik} u^c_{,j} u^a_{,l} x^l_{,bc} + u^b_{,i} u^c_{,jk} u^a_{,l} x^l_{,bc} + u^b_{,i} u^c_{,j} u^a_{,kl} x^l_{,bc} + u^b_{,i} u^c_{,j} u^a_{,l} u^d_{,k} x^l_{,bcd} \right] . \tag{3.10}$$

To find $x^i_{,a}$ and the higher derivatives, first note that from Eq. (3.4) we immediately get

$$x^i_{,\lambda^A} = (\sigma^i_{\text{ref}})_{,\lambda^A} + \xi\, \nu^i_{,\lambda^A} , \qquad\qquad x^i_{,\xi} = \nu^i . \tag{3.11}$$

We hence have

$$x^i_{,a} = (\sigma^i_{\text{ref}})_{,a} + \xi\, \nu^i_{,a} + \delta^0_a \nu^i , \tag{3.12}$$

$$x^i_{,ab} = (\sigma^i_{\text{ref}})_{,ab} + \delta^0_a \nu^i_{,b} + \delta^0_b \nu^i_{,a} + \xi\, \nu^i_{,ab} , \tag{3.13}$$

$$x^i_{,abc} = (\sigma^i_{\text{ref}})_{,abc} + \delta^0_a \nu^i_{,bc} + \delta^0_b \nu^i_{,ca} + \delta^0_c \nu^i_{,ab} + \xi\, \nu^i_{,abc} , \tag{3.14}$$

where, of course, we have $(\sigma_{\text{ref}})_{,3} = \nu_{,3} = 0$. At this point, we note that the numerical representation of the reference surface σ_{ref} must allow for highly accurate computation of third and even fourth derivatives[1] to evaluate (3.14).

3.2.1 Solving the nonlinear problem for the horizon function

With the reference-shape based parametrization of the surface $\mathcal{S}$, the MOTS condition $\Theta_{(\ell)} = 0$ translates to formally the same equation as in the case of a star-shaped parametrization [94], that is

$$\frac{A}{\|s\|^3} + \frac{B}{\|s\|} + \frac{K_{ij} s^i s^j}{\|s\|^2} - \text{tr}(K) = 0 , \tag{3.15}$$

where $\|s\|^2 = h_{ij} s^i s^j$ and

$$A = -s^i s^j s_{i,j} - \frac{1}{2} s^i h^{kl}_{,i} s_k s_l \tag{3.16}$$

$$B = h^{ij}_{,i} s_j + h^{ij} s_{i,j} + (\ln \sqrt{\det h_{ij}})_{,k}\, s^k . \tag{3.17}$$

---

[1]Fourth derivatives of $\sigma_{\text{ref}}(\lambda^A)$ are needed for the third derivatives of the normal $\nu(\lambda^A)$, which are computed from the tangents (i. e. the first derivatives of σ_{ref}).

Using (3.7) to define s_i, we see that (3.15) becomes a nonlinear partial differential equation (PDE) for the horizon function h. There are multiple ways to numerically solve such a nonlinear PDE. We chose to use a method based on the idea of a standard Newton root search, extended to solving nonlinear differential equations via the *Newton-Kantorovich* scheme as follows. See [32] for a discussion.

Let $\mathcal{N}$ be a nonlinear differential operator and u a solution of $\mathcal{N}(u) = 0$. We will start with some initial guess $u^{(0)}$ for u and let $u^{(i)}$ be the ith step in the search. Now, let $\Delta^{(i)} = u - u^{(i)}$, so that we have $u = u^{(i)} + \Delta^{(i)}$. If the $u^{(i)}$ are sufficiently close to u, we can expand $\mathcal{N}(u)$ around $u^{(i)}$ up to linear order, i.e.

$$0 = \mathcal{N}(u^{(i)} + \Delta^{(i)}) \approx \mathcal{N}(u^{(i)}) + \mathcal{N}_u \Delta^{(i)} . \tag{3.18}$$

Here, $\mathcal{N}_u$ is the variational derivative of $\mathcal{N}(u)$ acting as a linear operator on $\Delta^{(i)}$ and it is defined as

$$\mathcal{N}_u \Delta = \lim_{\varepsilon \to 0} \frac{\mathcal{N}(u + \varepsilon \Delta^{(i)}) - \mathcal{N}(u)}{\varepsilon} = \frac{d}{d\varepsilon}\Big|_{\varepsilon=0} \mathcal{N}(u + \varepsilon \Delta^{(i)}) . \tag{3.19}$$

A common and possibly more familiar notation for (3.19), which we shall use in some instances, is $\mathcal{N}_u \Delta = (\delta \mathcal{N})\Delta$. We take (3.18) to approximate a step $u^{(i)} \to u^{(i+1)}$ by solving the *linear* PDE

$$\mathcal{N}_u \Delta^{(i)} = -\mathcal{N}(u^{(i)}) \tag{3.20}$$

for $\Delta^{(i)}$ and define $u^{(i+1)} = u^{(i)} + \Delta^{(i)}$. These steps are continued until a suitable convergence criterion is satisfied.

In our case, the operator is the expansion $\Theta_{(\ell)}$ taken as acting on the horizon function h. Note that $\Theta_{(\ell)}$ depends on h only ultralocally, i.e. evaluated at one point of a surface $\mathcal{S}$ represented by h, it depends on h only through its value and partial derivatives, not on values of h elsewhere. This immediately implies that (3.19) can be obtained almost trivially by treating $\zeta^1 := h$, $\zeta^2_A := \partial_A h$ and $\zeta^3_{AB} := \partial_A \partial_B h$ as independent variables of an ordinary function $\Theta_{(\ell)}(\zeta^1, \zeta^2_A, \zeta^3_{AB})$ and computing the partial derivatives $\partial_{\zeta^1}\Theta_{(\ell)}$, $\partial_{\zeta^2_A}\Theta_{(\ell)}$ and $\partial_{\zeta^3_{AB}}\Theta_{(\ell)}$. The linear operator (3.19) is then, with obvious notation, given by

$$(\delta\Theta_{(\ell)})\Delta^{(i)} = \left[(\partial_h \Theta_{(\ell)}) + (\partial_{\partial_A h}\Theta_{(\ell)})\partial_A + (\partial_{\partial_A \partial_B h}\Theta_{(\ell)})\partial_A \partial_B\right]\Big|_{h=h^{(i)}} \Delta^{(i)} , \tag{3.21}$$

where summation over A and B is implied.

3.2.2 Taking the linear steps

The individual Newton steps consist of solving

$$(\delta\Theta_{(\ell)})\Delta^{(i)} = -\Theta_{(\ell)} \tag{3.22}$$

for $\Delta^{(i)}$ and then taking the step $h^{(i+1)} = h^{(i)} + \Delta^{(i)}$. Note that the expansion $\Theta_{(\ell)}$ and its variation occurring in Eq. (3.22) depend on $h^{(i)}$ and its derivatives, so that we solve a different problem in each step. These steps are repeated until a suitable convergence criterion, to be detailed below, is met. We chose a pseudospectral method to solve (3.22) numerically. This method is based on the idea that we represent the solution $u : \mathbb{R}^d \to \mathbb{R}$ of a general uniquely solvable linear PDE,

$$\mathcal{L}u = f \qquad \text{and boundary conditions}, \tag{3.23}$$

as a truncated series of suitable functions $\Phi_n : V \subset \mathbb{R}^d \to \mathbb{R}$, i. e.

$$u^N(x) = \sum_{n=1}^{N} a_n \, \Phi_n(x). \tag{3.24}$$

In one-dimensional problems ($d = 1$), we will call N the *resolution* of a particular numerical solution. When inserting (3.24) into (3.23), the operator $\mathcal{L}$ acts only on the basis functions, i. e. (3.23) is equivalent to

$$\sum_{n=1}^{N} a_n \, \mathcal{L}\Phi_n(x) = f(x). \tag{3.25}$$

We now choose a set of N points in V, the so-called *collocation points*

$$x_m \in V, \qquad m = 1, \dots, N, \tag{3.26}$$

and demand that (3.25) holds at these points. The result is a set of N linear equations for the N coefficients a_n,

$$L\boldsymbol{a} = \boldsymbol{f}, \tag{3.27}$$

where L is the matrix with elements $L_{mn} := \mathcal{L}\Phi_n(x_m)$, $\boldsymbol{a}$ is the vector of components a_n and $\boldsymbol{f}$ has components $f_m := f(x_m)$. Boundary conditions can be imposed by either choosing the Φ_n to individually satisfy them or by replacing equations in (3.27). We will be able to use the former strategy in our applications. With a suitable choice of a basis Φ_n and collocation points x_m and the correct boundary conditions imposed such that (3.23) is uniquely solvable, the square matrix L_{mn} will have full rank. Efficient numerical methods exist in many of the standard numerical libraries to solve for the a_n

with high accuracy. Note that for common choices of basis sets Φ_n, the convergence of u^N in (3.24) will be exponential in general cases [32, 37], which means that for large N, we usually have $|u(x) - u^N(x)| \sim \mathcal{O}(b(N)e^{-rN})$, where $b(N)$ varies more slowly with N than the exponential. If the basis functions are of order 1, which will be the case for the usual choices, then this implies that the coefficients a_n also decay exponentially. As a first convergence test, it is therefore possible to simply inspect the decay of $|a_n|$.

In one dimension, the typical choices for bases include Fourier bases for periodic problems without further symmetries, cosine or sine bases for periodic problems with even or odd symmetry, respectively, w. r. t. reflections about $x = 0$, and Chebyshev polynomials for general problems without symmetries. This exponential convergence is thus retained when solving (3.23) using the pseudospectral method.

In general, convergence can be assessed in various ways. For the present case, we use the fact that by (3.22), we obtain values of the expansion at the collocation points in each step. Since a MOTS has $\Theta_{(\ell)} = 0$, we take the maximum of the magnitudes of these values. If this lies below some tolerance, we define the solution to have converged *at the collocation points*. This test checks for a solution of the nonlinear problem (3.15), i.e. that the Newton steps have converged. However, it will not indicate convergence of the solution in terms of the resolution N. Therefore, after convergence at the collocation points has been achieved, we evaluate $\Theta_{(\ell)}$ at a larger set of points lying between the original collocation points. The solution has converged if these values also lie below the set tolerance. Typical for numerical methods involving finite representations of real values is the occurrence of a *round-off plateau*, indicated by no further reduction of errors when increasing the resolution or taking further Newton steps. Further factors limiting the accuracy we can attain occur when individual quantities used in computing $\mathcal{L}\Phi_n(x_m)$ or $f(x_m)$ contain errors. In our case, the main source of such errors will be the values of the metric components h_{ij} and the extrinsic curvature K_{ij} as well as their derivatives. When these are obtained from numerical relativity simulations, their accuracy is often limited much more by the used evolution parameters than by the limitations in floating point representation. Additional errors are introduced if such quantities are known on a fixed set of grid points and need to be interpolated to the exact coordinates they have to be evaluated at. Fortunately, the effect of all these errors can easily be analyzed by (independently) varying the resolution of the simulation as well as the resolution with which the MOTS finder operates. These error analyses will be discussed together with the results for the time symmetric case in Chapter 4 and for numerical simulations in Chapter 5.

3.3 Considerations in axisymmetry

If we limit ourselves to axisymmetric problems, i.e. to slices Σ of spacetimes possessing a one-parameter group of isometries χ_ϕ with orbits that are closed spacelike curves contained within a slice, and also only consider axisymmetric MOTSs, then the MOTS finding problem (3.15) becomes an ordinary differential equation (ODE) for the horizon function $h : S^1 \to \mathbb{R}$. The axisymmetry allows us to represent the reference surface $\mathcal{S}_{\text{ref}}$ via a *curve* γ_{ref} in some coordinate plane. Without loss of generality, we shall choose coordinates such that the symmetry axis is the z axis and we shall take γ_{ref} to lie in the x-z coordinate plane. The surface of revolution around the z axis then defines $\mathcal{S}_{\text{ref}}$. The curve $\gamma_{\text{ref}} : [0, \pi] \to \mathbb{R}^2$ starts at one pole $\gamma_{\text{ref}}(0)$ and ends at the other pole $\gamma_{\text{ref}}(\pi)$, both lying on the z axis. For sufficient smoothness, we demand that the tangents $\gamma'_{\text{ref}}(0)$ and $\gamma'_{\text{ref}}(\pi)$ are orthogonal to ∂_z, i.e. to vectors pointing along the symmetry axis. This is achieved by writing the component functions for x and z as

$$\gamma_{\text{ref}}(\lambda) = \begin{pmatrix} \sum_{n=1}^{N_{\text{ref}}} a_n^x \sin(n\lambda) \\ \sum_{n=0}^{N_{\text{ref}}-1} a_n^z \cos(n\lambda) \end{pmatrix}. \tag{3.28}$$

We shall call N_{ref} the resolution of the reference curve. The transverse vector field ν used in (3.4) to define the local coordinates is constructed via

$$\nu(\lambda) = \begin{pmatrix} -\left(\gamma'_{\text{ref}}(\lambda)\right)_z \\ \left(\gamma'_{\text{ref}}(\lambda)\right)_x \end{pmatrix}, \tag{3.29}$$

where the differentiation of the sums in (3.28) can be done analytically. The horizon function h is accordingly written as

$$h(\lambda) = \sum_{n=0}^{N-1} a_n \cos(n\lambda), \tag{3.30}$$

where we use cosines to account for the symmetries of h with respect to mirroring across $\lambda = 0$ and $\lambda = \pi$. The curve $\gamma : [0, \pi] \to \mathbb{R}^2$ representing the MOTS $\mathcal{S}$ is thus

$$\gamma(\lambda) = \gamma_{\text{ref}}(\lambda) + h(\lambda)\, \nu(\lambda). \tag{3.31}$$

N shall be called the resolution of the curve γ representing the MOTS $\mathcal{S}$. When no ambiguity can arise, we will henceforth identify the curves γ and γ_{ref} with the MOTS $\mathcal{S}$ and the reference shape $\mathcal{S}_{\text{ref}}$, respectively.

In a simulation scenario, where we are given slices (Σ, h_{ij}, K_{ij}) of spacetime in close succession, it is natural to *track* a horizon by using a MOTS we found in one slice as reference surface in the next slice. But even in case of just initial data, a successful strategy has been to locate a MOTS in a configuration where it can easily be found, possibly even with a star-shaped ansatz, and then successively change the parameters in small increments until the desired values are reached. In each step, we can use the MOTS of the previous step as reference shape. We always start with $h(\lambda) \equiv 0$, resulting in the previous MOTS becoming our initial guess for the nonlinear search. To avoid a deep hierarchy in the shape definition (with multiple layers of reference shapes being each in turn based on a reference shape, up to an almost undistorted star-shaped initial shape), we numerically sample the x and z component functions and represent these as finite sums as per (3.28).

However, one key observation was necessary for achieving accurate results, especially in cases of highly distorted MOTSs: Consider a slice Σ_{t_1} containing a MOTS γ_1 and a neighboring slice Σ_{t_2} containing a MOTS γ_2 close to γ_1. Assume γ_1 has already been located by the MOTS finder. We now wish to use γ_1 as reference surface γ_{ref} for locating γ_2.[2] When γ_{ref} has a high resolution N_{ref}, then the precise details of this shape will not match the features of the MOTS γ_2 we try to locate. One example is a narrow almost crease-like *neck* which we found for the inner common MOTS (see Chapter 5). Even if the location of this near-crease-like structure is offset only slightly by the time step, all the details introduced by the high-frequency components (i.e. the contributions of the a_n^x and a_n^z for large n) need to be compensated (and the new structure be introduced) by the horizon function h of the MOTS γ_2 we try to find. Much higher accuracy could be obtained, and at a much lower resolution, when the reference surface γ_{ref} was artificially smoothed by limiting its resolution N_{ref} to low values, usually around $10\,\%$ of the original curve's resolution, but no less than $N_{\mathrm{ref}} = 5$.

3.3.1 Reparametrization

Another equally important part of the numerical strategy is controlling the parametrization of the reference shape γ_{ref}. Take any smooth bijection $s : [0, \pi] \to [0, \pi]$, where $s(0) = 0$ to retain orientation, then $\gamma_{\mathrm{ref}} \circ s$ has the same image as γ_{ref} and could, at least conceptually, be taken equally well as reference shape. In practice, however, the parametrization of γ_{ref} has a large influence on the resolution N required to obtain accurate results. One approach to fix the parametrization is that of constant speed in coordinate space, i.e.

$$\|\gamma_{\mathrm{ref}}'\|_2 = \mathrm{const}\,, \tag{3.32}$$

---

[2]This means we use the component functions of γ_1 with respect to coordinates in Σ_{t_1} as component functions of γ_{ref} with respect to coordinates in Σ_{t_2}.

where $\|\cdot\|_2$ is the Euclidean 2-norm of the coordinate values. However, it turned out that a better choice is to "slow down" at places of high curvature in coordinate space. Best results were achieved with the following algorithm for reparametrizing a reference curve γ_{ref}.

1. Compute a constant speed parametrized curve $\gamma_0 = \gamma_{\text{ref}} \circ s_0$, such that $\|\gamma_0'\|_2 = \text{const}$.

2. Take the function $f(\lambda) = k^{AB} k_{AB}|_{\gamma_0(\lambda)}$ and expand it into a series of cosines, $f(\lambda) \approx \sum_{n=0}^{N_0-1} a_n \cos(n\lambda)$. Here, k_{AB} is the extrinsic curvature of the surface of revolution embedded in coordinate space.

3. "Smoothen" f by artificially damping the coefficients via $a_n \to a_n e^{-\beta n}$, where the smoothing factor β is set to $\beta = 0.05$. Let f^{smooth} be the function constructed from this new set of coefficients.

4. Compute a parametrized curve γ_1, such that $\|\gamma_1'\|_2 \propto 1/\sqrt{f^{\text{smooth}}}$ and take γ_1 as the reparametrized reference curve.

Given a curve γ_0 and any speed function v, how do we obtain a curve $\gamma = \gamma_0 \circ s$, such that $\|\gamma'\|_2 \propto v$? First, note that

$$\|\gamma'(\lambda)\|_2 = s'(\lambda) \|\gamma_0'(s(\lambda))\|_2 \,, \tag{3.33}$$

implying

$$s' = \alpha \frac{v(s)}{\|\gamma_0'(s)\|_2} \tag{3.34}$$

for some proportionality factor α, which is chosen such that $s(\pi) = \pi$. This is a nonlinear ODE for the reparametrization function s. To solve (3.34) numerically, we initially set $\alpha = 1$. Starting now with $s(0) = 0$, we integrate (3.34) using a Runge-Kutta integration method provided by the *scipy.integrate.solve_ivp* routine of the *SciPy* Python library [98]. We stop the integrator when it reaches $s = \pi$. This will happen at a parameter b and the result is a bijection $s : [0, b] \to [0, \pi]$. A simple linear rescaling provides the reparametrization function $\lambda \mapsto s(\lambda b/\pi)$ used to construct the new curve γ.

Fig. 3.3 shows the effect of three different parametrizations. For the same MOTS, we take the same initial reference curve and parametrize it in three different ways. Afterwards, the MOTS finder is used to locate the precise MOTS in the given slice. In this example, we use a fairly distorted inner common MOTS $\mathcal{S}$ of Brill-Lindquist initial data, which is discussed in detail in Chapter 4. The three panels on the left show $\mathcal{S}$ and a visual indication of the parametrization using a set of equidistant points in the curve parameter λ. The panels on the right show the magnitudes of the coefficients needed
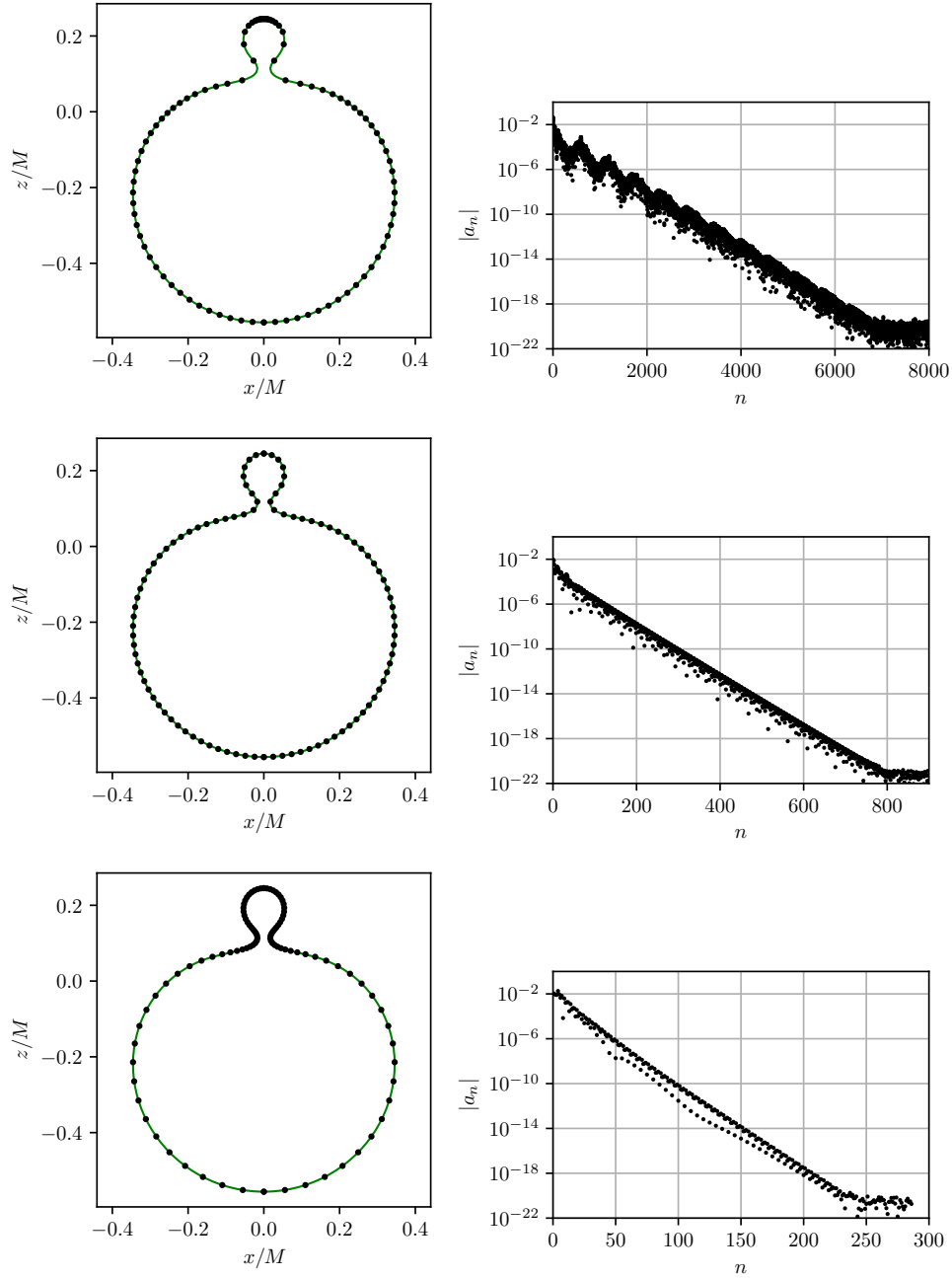
Figure 3.3: Comparison of different reparametrization strategies. The left panel in each row shows the coordinate representation of a MOTS together with 100 points distributed according to the parametrization of the curve, i.e. the points lie equidistant in the curve parameter λ. The respective right panels show the magnitudes of the coefficients a_n used to represent the horizon function h via Eq. (3.30). The point at which these reach the round-off plateau is an indication of the resolution required for convergence. See text for details.

for representing the horizon function h. Note that for easier comparison, the number of points shown on the left is always set to 100. We follow the strategy explained above and track $\mathcal{S}$ through a series of initial data, starting with a case where $\mathcal{S}$ is star-shaped and easy to locate. The reference shape $\mathcal{S}_{\text{ref}}$ is then the MOTS of the previous step.

The top panel of Fig. 3.3 shows a case with no reparametrization performed. The resulting parametrization is "inherited" from the first MOTS located with points equally distributed in the angle θ in coordinate space. As a result, the horizon function h requires a resolution of about $N \approx 7000$ basis functions to produce an accurate representation of the MOTS. With a constant speed parametrization using Eq. (3.32), the middle panel shows that the resolution required for convergent results drops by about one order of magnitude to $N \approx 800$. The curvature-based parametrization shown in the bottom panel reduces this resolution further and produces the numerically most efficient and accurate result with a resolution of $N \approx 250$.

3.3.2 Bispherical Coordinates

The numerical difficulty of finding the various MOTSs is strongly dependent on how distorted their coordinate shapes are. For all but the most extreme cases, the methods introduced thus far are sufficient to converge to the floating point round-off plateau or the respective accuracy limits imposed by the numerical data. We encountered these extreme cases solely with the inner common MOTSs consisting of two near-spherical portions smoothly connected by a very narrow *neck*-like part. See Chapter 5 for details on the geometry of this MOTS. There exists a choice of coordinates, the bipolar coordinates (u_1, u_2), which are well suited for such kinds of problems. They possess two foci located at $x = 0$ and $z = c \pm a$ and are implicitly defined by

$$ x = \frac{a \sin u_1}{\cosh u_2 - \cos u_1} \,, \qquad\qquad z = c + \frac{a \sinh u_2}{\cosh u_2 - \cos u_1} \,. \qquad (3.35) $$

Representing the reference shape γ_{ref} using component functions for the (u_1, u_2) coordinates instead of the (x, z) coordinates leads to a much less distorted shape. This is shown in Fig. 3.4, where three cases of different degrees of distortion are shown with corresponding choices of the constants c and a.

Applying additionally the reparametrization strategy of Sec. 3.3.1 in the (u_1, u_2) coordinate space equipped with a fictitious flat metric, results in both, higher accuracy as well as lower required resolution N. An example demonstrating the effect of these coordinates is shown in Fig. 3.5.

The parameters c and a used in Eq. (3.35) are numerically optimized. The precise strategy utilizes multiple of the MOTSs available in each Cauchy slice of an evolution. The following description will therefore refer to a particular aspect, which is presented
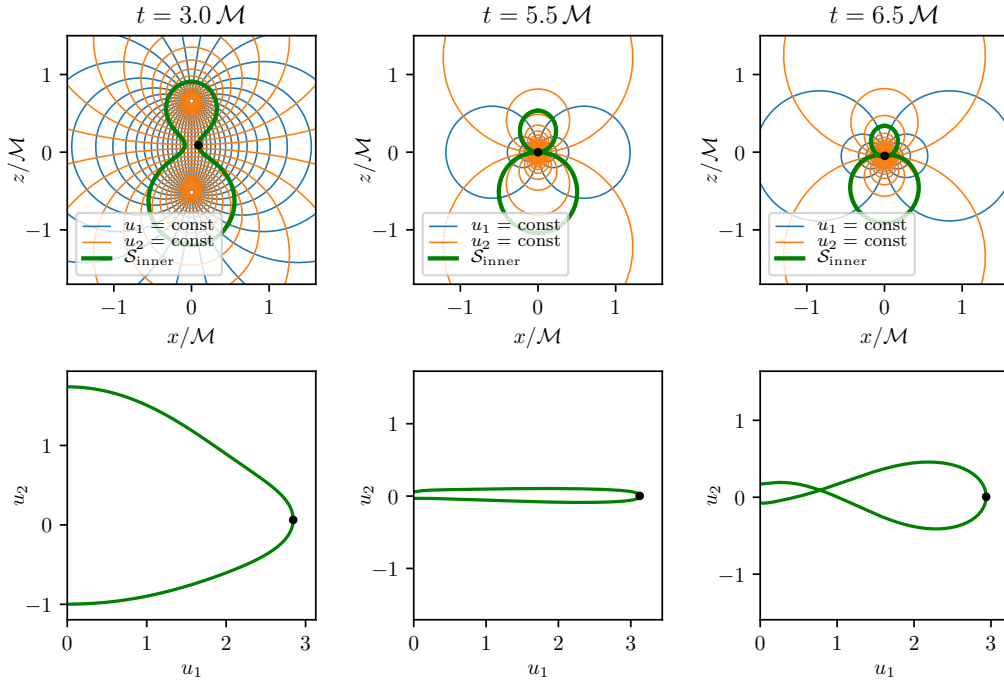
Figure 3.4: Effect of using bipolar coordinates to represent highly distorted surfaces. The three columns show a particular MOTS, $\mathcal{S}_{\text{inner}}$, at three different times of a simulation, with the right-most column showing a case with self-intersections. Details of the physical interpretation can be found in Chapter 5. The top panels show the MOTSs in the numerical coordinates as well as lines of constant u_1, u_2. The bottom panels contain the representation in the bipolar coordinates (here limited to the part of positive x values). Note that the constants c and a of Eq. (3.35) are numerically optimized to minimize distortions in the $u_{1,2}$ coordinate plane. The results of this optimization read in the left panel $c \approx 0.07\,\mathcal{M}$, $a \approx 0.59\,\mathcal{M}$, in the middle panel $c \approx -0.0007\,\mathcal{M}$, $a \approx 0.016\,\mathcal{M}$, in the right panel $c \approx -0.05\,\mathcal{M}$, $a \approx 0.033\,\mathcal{M}$. (Figure adapted from [84].)

and interpreted in much greater detail in Chapter 5. For the present description, it suffices to know that in the slices considered here, we have two MOTSs $\mathcal{S}_1$, $\mathcal{S}_2$ with relatively low distortions. These are accompanied by a common highly distorted MOTS $\mathcal{S}_{\text{inner}}$ which encloses $\mathcal{S}_{1,2}$ from the outside or inside. The outermost MOTS $\mathcal{S}_{\text{outer}}$ will be unimportant here. We now choose c to lie in the coordinate center between the facing points of $\mathcal{S}_1$ and $\mathcal{S}_2$ on the symmetry axis. The value of a is optimized after $\mathcal{S}_{\text{inner}}$ is found in one slice and this optimal value is used for constructing the coordinates (3.35) when finding $\mathcal{S}_{\text{inner}}$ in the next slice.

The optimization itself is carried out as follows. We first represent the curve defining $\mathcal{S}_{\text{inner}}$ using coordinate functions $u_1(\lambda)$ and $u_2(\lambda)$ chosen to be truncated series of sines and cosines, respectively. This choice correctly captures the reflection symmetry of the shapes across the symmetry axis in the x-z coordinate plane. We truncate these
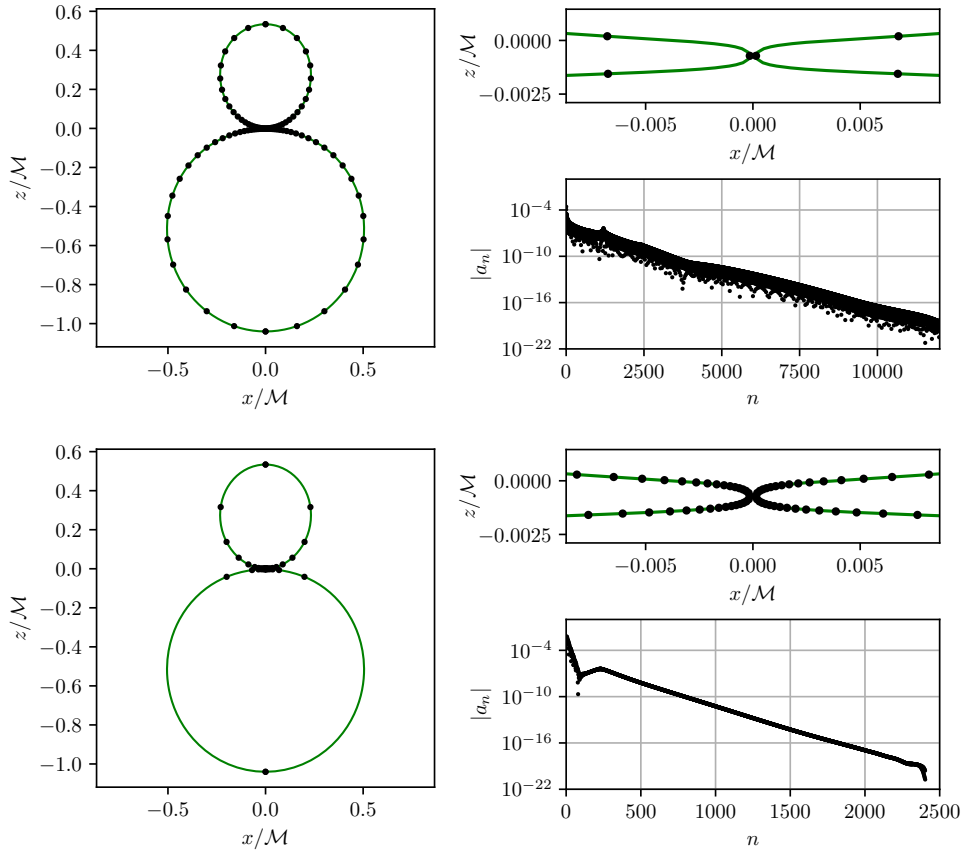
Figure 3.5: The effect of applying the curvature based reparametrization described in Sec. 3.3.1 in the numerical x, y, z coordinate space (top) or the bipolar u_1, u_2 coordinate space (bottom). To visualize the resulting parametrization, both cases show 100 points equidistant in the curve parameter λ. Both cases show the same MOTS, $\mathcal{S}_{\text{inner}}$, at a simulation time $t = 5.5\,\mathcal{M}$ where the distortions are very high (see Chapter 5 for details). The left panels show an overview and the upper and lower panels on the right show a close-up near the "neck" where the curvature is highest, and the coefficients of the horizon function required for a converging solution, respectively. Notice how the case on the bottom using bipolar coordinates requires only a fraction of the resolution of the top case without bipolar coordinates. The reason is the extremely high curvature at the "neck", which is resolved much better in the bottom case.

series slightly earlier than required for a faithful representation. As a consequence, the residual expansion will be larger than the round-off plateau. Varying a, this process is repeated until a local minimum of the residual expansion is found, indicating a suitable value of a. Assuming the optimal parameter varies slowly with simulation time, this value is then used in the next time step.

3.4 Validation

With a new MOTS finder code in place, it is important to assess its performance both in terms of correctness and accuracy. The first test verifies the most important aspect, namely the correct calculation of the expansion of the outgoing null rays on a surface. Since our convergence checks are based on computing this quantity, it is crucial that its evaluation yields correct and highly accurate results. This test uses a slice of the Schwarzschild spacetime in isotropic coordinates. The 3-metric is given by $h_{ij} = \psi^4 \delta_{ij}$, where δ_{ij} is the flat 3-metric and

$$\psi(r) = 1 + \frac{M}{2r} \,. \tag{3.36}$$

Surfaces of constant r coordinate then have the expansion

$$\Theta_{(\ell)} = \frac{\sqrt{2}}{\psi^2} \left(\frac{1}{r} + 2\frac{\psi'}{\psi} \right) = \sqrt{2} r \frac{r - M/2}{(r + M/2)^3} \,. \tag{3.37}$$

We construct different surfaces $\mathcal{S}_r$ of constant r coordinate using the new reference shape based parametrization. For $r \neq M/2$ these will not be MOTSs, but they are surfaces of constant expansion $\Theta_{(\ell)}$. The expansion on these surfaces computed using the numerical methods implemented in our code are then compared with the analytical value given by Eq. (3.37). Fig. 3.6 shows that the numerical calculation matches with the analytical one on the order of 10^{-15}, i.e. close to the floating point limit.

The second test evaluates the MOTS finder itself and uses a much more general configuration. In order to have a non-time-symmetric slice and hence non-vanishing extrinsic curvature, we take the Schwarzschild spacetime in Kerr-Schild coordinates

Figure 3.6: Accuracy of the numerical code to compute the expansion. We calculate the expansion $\Theta_{(\ell)}$ at a point of an $r = \text{const}$ surface in a slice of the Schwarzschild spacetime in isotropic coordinates and compare it with the exact value of Eq. (3.37). For each value of r, we use a sphere of radius $r/2$ as reference shape $\mathcal{S}_{\text{ref}}$. (Figure adapted from [82].)
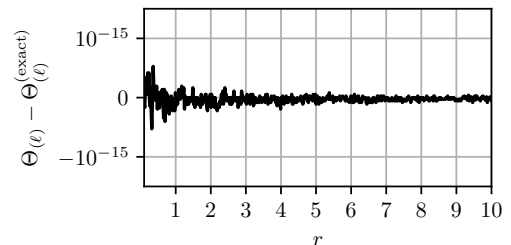
[72]

$$h_{ij} = \delta_{ij} + \frac{2M}{r} \frac{x_i x_j}{r^2} \,, \tag{3.38}$$

$$K_{ij} = \frac{2M}{r^4} \frac{1}{\sqrt{1 + 2M/r}} \left[r^2 \delta_{ij} - \left(2 + \frac{M}{r} \right) x_i x_j \right] \,. \tag{3.39}$$

Here, δ_{ij} is again the flat 3-metric and $(x_1, x_2, x_3) = (x, y, z)$ the Cartesian coordinates for which δ_{ij} becomes the Kronecker delta, and $r^2 = x^2 + y^2 + z^2$. The notion of a MOTS being star-shaped is bound to the chosen coordinates. We can hence perform a coordinate transformation to make it non-star-shaped. The transformation used here is $\bar{z} = z$ and

$$\bar{x} = x \left(1 - \frac{\beta}{\cosh((z - z_0)/\gamma)} \right) \,, \tag{3.40}$$

where z_0, β, γ are constants. Using the transformation (3.40), the metric h_{ij} and extrinsic curvature K_{ij} are sampled on grids of various resolutions and the MOTS finder is used to locate the apparent horizon $\mathcal{S}$. The exact location of $\mathcal{S}$ is at $r = 2M$, whence we can compare the numerically generated result with the exact one. Fig. 3.7 shows in the left panel the exact form of $\mathcal{S}$ in the transformed coordinates and the
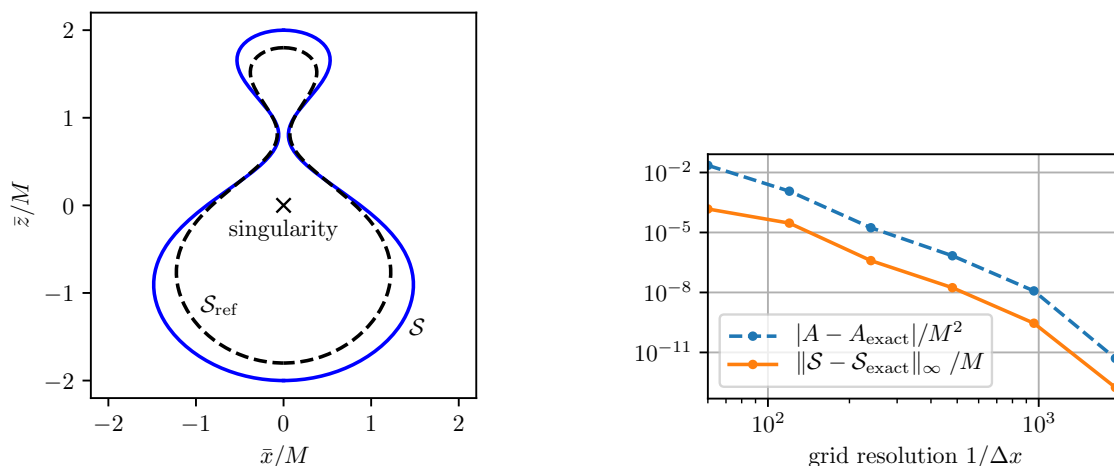
Figure 3.7: Horizon $\mathcal{S}$ in a slice of the Schwarzschild spacetime in Kerr-Schild coordinates (3.38) transformed using Eq. (3.40). The left panel shows the exact shape $\mathcal{S}$ as well as the reference shape $\mathcal{S}_{\mathrm{ref}}$ used to numerically locate $\mathcal{S}$. We sample the slice data on an equidistant grid in the $(\bar{x}, \bar{z})$ coordinates to test the full pipeline of finding MOTSs in numerical simulations. Varying the grid spacing Δx, the right panel shows that both, the numerically computed area A of $\mathcal{S}$ as well as its coordinate shape converge to the exact results as the grid resolution $1/\Delta x$ is increased. (Figure adapted from [84].)

reference surface $\mathcal{S}_{\mathrm{ref}}$ used also as initial guess for the finder. The right panel shows that we do find the horizon with high accuracy by plotting the errors of two different quantities as function of the grid resolution. The first is the area A of the numerically found surface. The second shows the maximum coordinate distance of the found shape to the exact shape. Both quantities clearly decay for higher resolutions demonstrating the high accuracy of our finder.

Chapter 4

Results for Initial Data

One of the great practical advantages of the quasilocal horizon formalism is the fact that the basic building blocks, the MOTSs, can be located using data on a Cauchy slice $\Sigma \subset \mathcal{M}$ without knowledge of the surrounding spacetime. Even though some exact black-hole solutions to the Einstein field equations are known, there is a much larger variety of solutions providing data only on such a slice. In a numerical context, these can e.g. be used as initial data for a simulation. One of the simplest of these solutions is due to Brill and Lindquist [35], which provides a closed-form expression for a slice containing an arbitrary number of black holes at a moment of time symmetry. This class of solutions will be discussed in Sec. 4.1.

From a numerical perspective, these solutions are very fast and accurate to compute and thus open the unique opportunity to analyze horizons in a large number of configurations. Among these are configurations containing highly distorted MOTSs useful for benchmarking a horizon finder. However, the interest in these configurations extends beyond having an efficient numerical test bench. In fact, the number of horizons we can locate varies across the parameter space of even a simple two-black-hole Brill-Lindquist configuration. By approaching the points where horizons "disappear", we can gain insights not only into the performance of the numerical algorithm, but also into the connection between the MOTS stability operator and their existence. Many of the results discussed here are published in [82].

4.1 Brill-Lindquist initial data

Let Σ be an orientable sufficiently smooth 3-manifold and h_{ij} a Riemannian metric on Σ. Furthermore, let K_{ij} be a symmetric tensor field. Provided that the *constraint equations*

$$R + K^2 - K_{ij}K^{ij} = 16\pi \, T_{ij}T^iT^j \,, \tag{4.1}$$

$$D_jK_i^j - D_iK = -8\pi \, T_{jk}h_i^jT^k \,, \tag{4.2}$$

are satisfied, the initial value formulation of general relativity tells us that we can, at least locally, construct a spacetime satisfying the Einstein field equations by evolving

h_{ij} and K_{ij} using evolution equations. See also [21, 44]. In Eq. (4.1), R is the Ricci scalar of Σ, D_i the covariant derivative compatible with h_{ij}, and $K := K_i^i$ is the trace of K_{ij}. T_{ij} is the stress energy tensor and T^i defines a direction normal to Σ. The constructed spacetime will contain Σ as a Cauchy slice with induced metric h_{ij} and extrinsic curvature K_{ij}.

This is the predominant strategy to find spacetimes satisfying Einstein's field equations: We prescribe some initial data describing a physical situation of interest and then use numerical simulations to obtain a part of the corresponding spacetime. Interestingly, by making several simplifying choices, we can still obtain a great variety of black hole initial data. First, we choose our slice Σ to be time symmetric, which means that the extrinsic curvature K_{ij} vanishes identically on Σ. Next, we choose the 3-metric h_{ij} to be conformally flat,

$$h_{ij} = \psi^4 \, \delta_{ij} \,, \tag{4.3}$$

where ψ is the conformal factor and δ_{ij} the flat metric. The constraints then turn into a Laplace equation for ψ, i.e.

$$\Delta_\delta \psi = 0 \,, \tag{4.4}$$

where Δ_δ is the *flat* Laplacian, and we demand $\psi \to 1$ for $\|x\| \to \infty$ to obtain an asymptotically flat solution. The possible solutions then depend on the topology we choose for Σ. For $\Sigma = \mathbb{R}^3 \setminus \{x_i : i = 1, \ldots, n\}$, we obtain

$$\psi(x) = 1 + \sum_{i=1}^n \frac{a_i}{\|x - x_i\|} \,, \tag{4.5}$$

where $a_i \in \mathbb{R}$ are constants and $x_i \in \mathbb{R}^3$ are the coordinate values of the n punctures of Σ. This metric was described by Brill and Lindquist in 1963 [35] and represents a configuration of n non-spinning black holes at a moment of rest. In fact, this solution has $n + 1$ asymptotically flat ends; one for $\|x\| \to \infty$ and one each for $x \to x_i$. Their ADM masses can be shown to be

$$M = \sum_{i=1}^n 2a_i \qquad\qquad \text{for } \|x\| \to \infty \,, \tag{4.6}$$

$$M^{(i)} = 2a_i \left(1 + \sum_{\substack{j=1 \\ j \neq i}}^n \frac{a_j}{\|x_i - x_j\|} \right) \qquad\qquad \text{for } x \to x_i \,, \tag{4.7}$$

where M is associated with the total mass of Σ.

It is common to define $m_i := 2a_i$ and call m_i the "bare masses". This is motivated by the case when the x_i are far apart in coordinates, whence the ADM masses of the

asymptotic ends converge to the m_i for infinite separation. However, it is important to note that in the general case, the m_i are not the ADM masses of the n black holes. Nevertheless, $M = \sum_i m_i$ always holds exactly.

4.2 The MOTS structure in Brill-Lindquist data

Despite the simplicity of the Brill-Lindquist solution, there can be a rich MOTS structure. As an example, Fig. 4.1 shows the MOTSs found for $n = 3$ black holes located very close together on the z axis. The left panel shows a 3-dimensional visualization of the surfaces, while the right panel only shows the sections through the x-z plane. Due to the axisymmetry, the full information of the MOTSs is contained in the curves shown in the right panel. Therefore, we will henceforth represent axisymmetric MOTSs by curves in the x-z plane. In the depicted setting, we see three individual horizons (dashed red lines in the right panel) as well as various common MOTSs enclosing two or three of the individual horizons. The outermost MOTS, i.e. the apparent horizon, encloses all other MOTSs in this configuration.

For a more systematic study of the MOTSs, we will now consider configurations
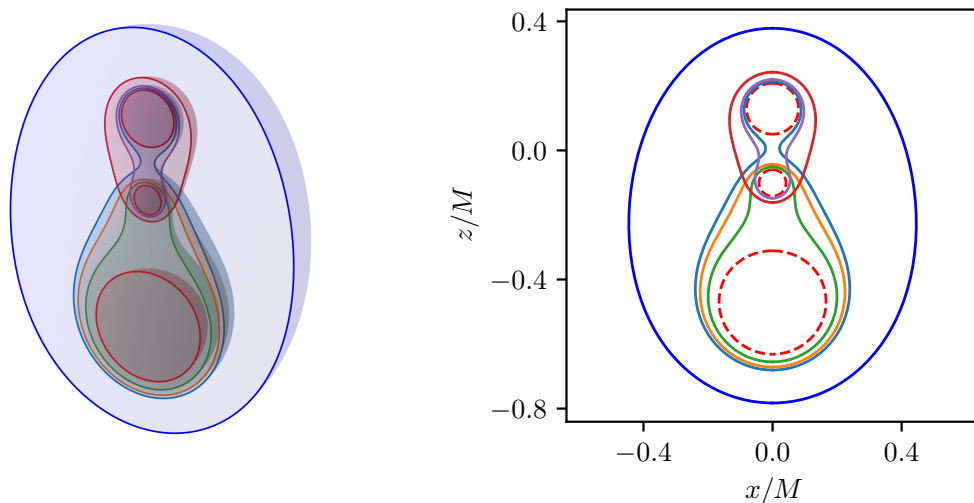
Figure 4.1: MOTSs found in Brill-Lindquist data for $n = 3$ black holes with bare masses $m_1 = 0.5$, $m_2 = 0.2$, $m_3 = 0.3$ and punctures located at $z_1 = -0.45$, $z_2 = -0.1$ and $z_3 = 0.12$. The total ADM mass is $M = 1$. The left panel shows a 3-dimensional visualization of the 9 MOTSs found in this setting, while the right panel shows only the sections in the x-z plane.

with $n = 2$ black holes, i.e.

$$h_{ij} \, dx^i \otimes dx^j = \left(1 + \frac{m_1}{2r_1} + \frac{m_2}{2r_2}\right)^4 (dx^2 + dy^2 + dz^2), \qquad (4.8)$$

where $r_i := \|x - x_i\|$ and $x_{1,2} = (0, 0, \pm d/2)$. These configurations are axisymmetric with the two black holes placed on the z axis. To parametrize this family of initial data, we use the *bare mass ratio* $q = m_2/m_1 \geq 1$, with $M = m_1 + m_2 = 1$, and the *distance parameter d*.

4.2.1 Results for mass ratio 1:4

The general behavior we find when modifying the distance parameter d has certain similarities to what one expects for a simulation of a head-on collision of two non-spinning black holes. For example, for large d there are only two separate individual MOTSs, while common horizons form as d is decreased. However, this correspondence is qualitative only and no quantitative conclusions can be drawn which would apply to time evolutions. For example, reducing d keeps the ADM mass of the slice constant, while by Eq. (4.7) the individual ADM masses $M^{(i)}$ tend to infinity as $d \to 0$.

In this section, we first focus on the case of a bare mass ratio $q = 4$. This has been studied previously by Mösta et al. [75] and since our new numerical algorithm is able to locate even highly distorted MOTSs, we will be able to extend the results presented in Fig. 2 of [75]. The MOTSs we find for various values of d are depicted in Fig. 4.2. For large d, there is no common horizon and the two black holes are seen to be separate, each having their own individual MOTS $\mathcal{S}_1$ and $\mathcal{S}_2$. When d becomes smaller than some q-dependent value $d_{\text{bifurcate}}$, two common horizons exist, an outer one, $\mathcal{S}_{\text{outer}}$, and an inner one, $\mathcal{S}_{\text{inner}}$. For $d \nearrow d_{\text{bifurcate}}$, $\mathcal{S}_{\text{inner}}$ and $\mathcal{S}_{\text{outer}}$ are found to coincide, while for decreasing d, $\mathcal{S}_{\text{outer}}$ loses its distortions while $\mathcal{S}_{\text{inner}}$ becomes highly distorted as is visible in Fig. 4.3.

For values of d below some value $d_{\text{vanish}} < d_{\text{bifurcate}}$, we are not able to locate $\mathcal{S}_{\text{inner}}$ numerically, although we continue to locate the three remaining horizons. Reducing d further by a small amount, we reach a case when also $\mathcal{S}_2$ cannot be found. One might ask whether this is due to numerical issues preventing $\mathcal{S}_{\text{inner}}$ and $\mathcal{S}_2$ from being located successfully, or whether the horizons are actually not present in these configurations. We will return to this question in much greater detail in Sec. 4.3 but it already seems clear from the shape visible in Fig. 4.3 that at least for $\mathcal{S}_2$, distortions cannot be responsible for the failure of locating it.

In summary, for $q = 4$, the behavior when d decreases is as follows:

- For large d, only $\mathcal{S}_1$ and $\mathcal{S}_2$ are found.

- At $d \approx 0.6987$, the two common horizons $\mathcal{S}_{\text{outer}}$ and $\mathcal{S}_{\text{inner}}$ form.
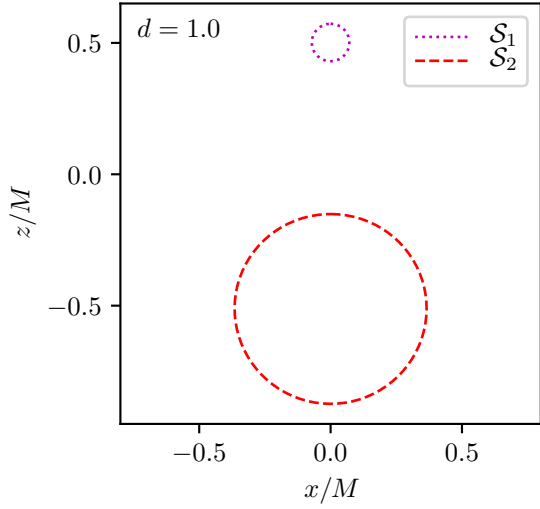
(a) At $d = 1$, common MOTSs have not yet formed and only the two individual ones $\mathcal{S}_1$, $\mathcal{S}_2$ exist.
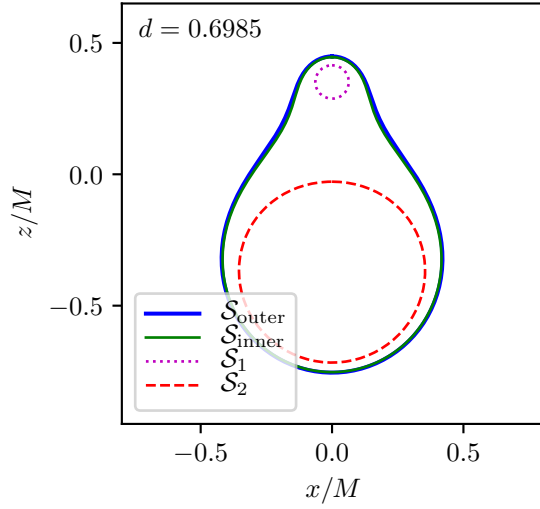
(b) Here, two common MOTSs $\mathcal{S}_{\text{outer}}$ and $\mathcal{S}_{\text{inner}}$ exist. At this distance, they are very close to each other.
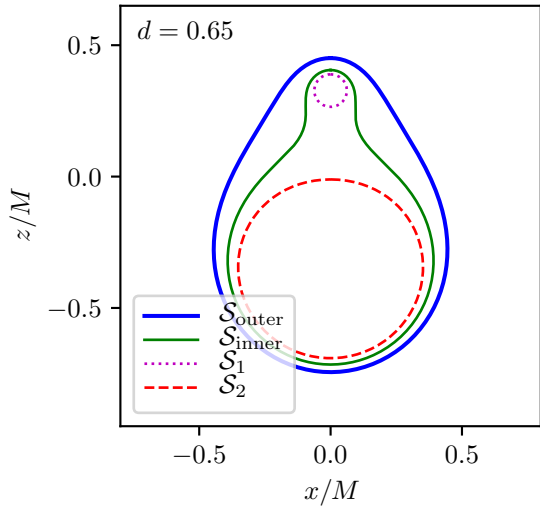
(c) Reducing the distance, $\mathcal{S}_{\text{outer}}$ and $\mathcal{S}_{\text{inner}}$ clearly separate.
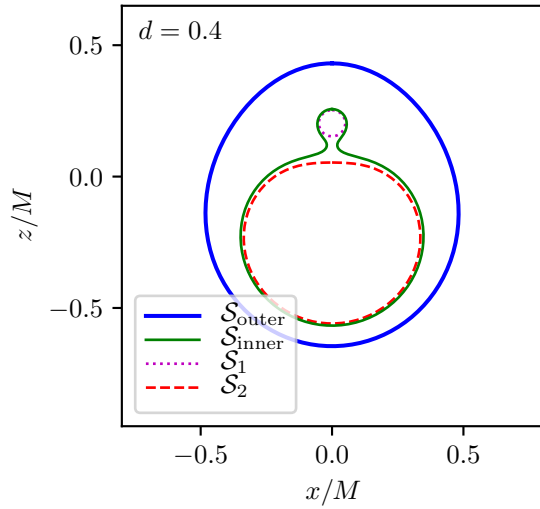
(d) As d is reduced further, $\mathcal{S}_{\text{outer}}$ becomes less distorted while $\mathcal{S}_{\text{inner}}$ is increasingly distorted.

Figure 4.2: MOTSs in Brill-Lindquist initial data for a bare mass ratio of $q = 4$ and various values of the distance parameter d. (Figure adapted from [82].)

- For $d \lesssim 0.6987$, $\mathcal{S}_{\text{outer}}$ becomes less distorted while $\mathcal{S}_{\text{inner}}$ becomes increasingly distorted.

- For $d \lesssim 0.1660$, $\mathcal{S}_{\text{inner}}$ ceases to be located by our MOTS finder.

- For $d \lesssim 0.1646$, $\mathcal{S}_2$ is no longer found, leaving only $\mathcal{S}_{\text{outer}}$ and $\mathcal{S}_1$ for smaller d.

Before continuing the discussion of physical and geometric properties of the MOTSs presented above, we shall point out that our new numerical algorithm is able to produce highly accurate results, even in the very distorted cases. Fig. 4.4 shows a quantity we monitor in order to asses convergence, i.e. the residual expansion $\|\Theta_{(\ell)}\|_\infty$, which is the maximum violation of the MOTS condition along $\mathcal{S}$. In order to get a conservative estimate of $\|\Theta_{(\ell)}\|_\infty$, we evaluate $\Theta_{(\ell)}$ at a large number of "measuring" points along the curve representing $\mathcal{S}$. Recall that we use a pseudospectral method to perform the linear steps, which eventually converge to $\Theta_{(\ell)}$ vanishing. By construction, the expansion will vanish only on the chosen set of collocation points. The number of collocation points is referred to here as the *resolution* of the curve. Choosing too small a resolution may lead to a large residual expansion *between* these collocation points. Hence, the number of measuring points is chosen to be at least a factor of 2 larger than the resolution of the curve, and the points are placed to not coincide with the collocation points. The log-linear plots in Fig. 4.4 clearly show exponentially decaying residual expansion as the pseudospectral resolution N is increased, with a final plateau of order 10^{-13}.
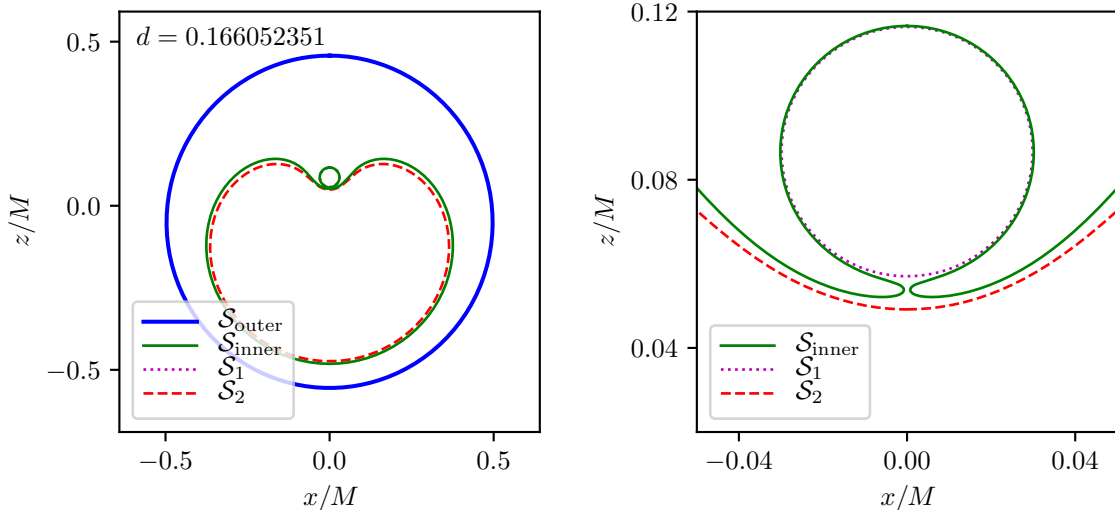
Figure 4.3: MOTSs at the smallest value of d for which $\mathcal{S}_{\text{inner}}$ could still be found. The left panel shows an overview and the right panel a close-up at the "neck" of $\mathcal{S}_{\text{inner}}$. (Figure adapted from [82].)
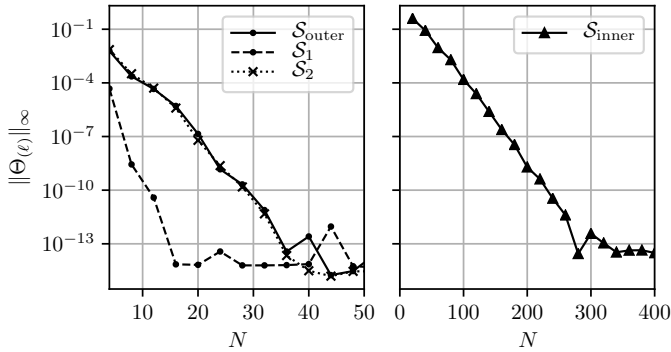
Figure 4.4: Residual expansion computed using increasing pseudospectral resolution N of the MOTS representation. The initially nearly linear decay in this log-linear plot indicates exponential decay of the error until the round-off plateau is reached. Note that for each resolution N, the full nonlinear search is repeated. The four MOTSs are found using the configuration of Fig. 4.2(d). (Figure adapted from [82].)

One notable feature in Fig. 4.3 is the fact that $\mathcal{S}_2$ becomes deformed, seemingly avoiding $\mathcal{S}_1$. This can be understood as an effect of keeping the condition of time symmetry. In time symmetric initial data, the MOTS condition $\Theta_{(\ell)} = 0$ coincides with that of $\Theta_{(n)} = 0$ and is the condition for a minimal surface. As argued in [75], two minimal surfaces sharing a common tangent must coincide by the maximum principle for elliptic operators. This implies that in axisymmetric configurations, MOTSs cannot touch on the z axis, which is consistent with the shapes we find.

One valid concern at this point could be that distortions of MOTSs are here discussed in terms of their shape in the x-z coordinate plane. We will therefore now present coordinate independent measures of curvature, namely the intrinsic Ricci scalar $\mathcal{R}$ of the MOTSs. This is shown in Fig. 4.5 for all four horizons for various values of d. From the top two panels, we see that $\mathcal{S}_{\text{outer}}$ and $\mathcal{S}_{\text{inner}}$ have very similar scalar curvatures for d close to $d_{\text{bifurcate}}$. However, as d is reduced, we see that $\mathcal{R}$ becomes essentially constant along $\mathcal{S}_{\text{outer}}$, while for $\mathcal{S}_{\text{inner}}$ it develops regions of high negative values around the points of highest distortion in coordinate shape. Note that the plot of $\mathcal{R}$ for $\mathcal{S}_{\text{inner}}$ does not show the value at the extremum in order to better visualize the remaining behavior. The dependence of the extremal value on d will be discussed together with other mass ratios in Sec. 4.2.2. Interestingly, for very small d close to d_{vanish}, the Ricci scalar has a second region with negative values (albeit less pronounced), which seems to correspond with a similar region of $\mathcal{S}_2$. Furthermore, while $\mathcal{S}_1$ has an almost constant Ricci scalar which decreases as $d \to 0$, we find stronger variations in $\mathcal{S}_2$, again matching the expectation from the coordinate shapes.

4.2.2 Considering other mass ratios

The results in this section contain various geometric quantities for the bare mass ratios $q = 1, 1.5, 2, 3, 4, 5$. We will present the dependency on the distance parameter d, while keeping the ADM mass of the slice at $M = 1$ as before.

(a) As d decreases to 0, $\mathcal{R}$ becomes constant along $\mathcal{S}_{\mathrm{outer}}$. Note that close to where it forms, there is a region with negative Ricci scalar.

(b) $\mathcal{R}$ coincides with that of (a) for d close to $d_{\mathrm{bifurcate}}$. Distortions increase dramatically towards smaller d. See Fig. 4.7 for extremal values.

(c) The smaller MOTS has nearly constant $\mathcal{R}$ for all d with the value decreasing despite the MOTS becoming "smaller" in coordinate space.

(d) Almost constant for large d, the Ricci scalar starts to vary considerably towards the point where $\mathcal{S}_2$ cannot be found anymore.

Figure 4.5: Ricci scalar along the four MOTSs as function of the invariant angle θ introduced in Sec. 2.3.

The first property we shall discuss is the horizon area

$$A = \int_{\mathcal{S}} dA \,, \tag{4.9}$$

where dA denotes the surface element on $\mathcal{S}$. In terms of coordinates (θ, φ) on $\mathcal{S}$, where $\cos\theta = \zeta$ refers to the invariant angular coordinate introduced in Sec. 2.3, this reduces in axisymmetry to a one-dimensional integral

$$A = 2\pi \int_0^\pi \sqrt{\det q_{AB}} \; d\theta \,. \tag{4.10}$$

Fig. 4.6 shows the numerically computed areas for the different mass ratios as function

(a) The area of the apparent horizon $\mathcal{S}_{\mathrm{outer}}$ approaches $16\pi M^2$ for all mass ratios. The increase is faster for more unequal masses.

(b) The area of $\mathcal{S}_{\mathrm{inner}}$ increases for decreasing d until it can no longer be found. The increase is slower for more unequal masses.

(c) $\mathcal{S}_1$ has the largest area increase as $d \to 0$ (note the logarithmic y axis). For $d \to \infty$, it has smaller area for higher mass ratios.

(d) The area of $\mathcal{S}_2$ is larger for higher mass ratios as $d \to \infty$.

Figure 4.6: Areas of the four MOTSs as function of d for various mass ratios. (Figure adapted from [82].)

of d. Note that as $d \to 0$, the initial data becomes a slice of the Schwarzschild spacetime in isotropic coordinates with an ADM mass of $M = m_1 + m_2 = 1$. The horizon mass of $\mathcal{S}_{\mathrm{outer}}$ is in our case of vanishing angular momentum just the irreducible mass

$$M_{\mathrm{irr}} := \sqrt{A/16\pi} \qquad (4.11)$$

and must hence tend to this value, i.e. $A_{\mathrm{outer}} \to 16\pi M^2 \approx 50.265$. This can indeed be seen in the upper-left panel of Fig. 4.6 for all mass ratios considered.

A similar argument can be made for $\mathcal{S}_1$ and $\mathcal{S}_2$. In this case, they can be modeled

(a) For $d \to 0$, we have $\mathcal{R} \to 1/(2M_{\text{irr}}^2)$, consistent with the results here.

(b) This complements Fig. 4.5(b) and shows that the extremum takes on large values near the point where $\mathcal{S}_{\text{inner}}$ vanishes.

(c) The maximum of $|\mathcal{R}|$ for $\mathcal{S}_1$ vanishes as $d \to 0$, consistent with $\mathcal{S}_1$ moving towards the puncture (i. e. an asymptotically flat end).

(d) For $q = 1$, this is the same as in (c). The discontinuous slope in the other cases is due to jumps of the point where the maximum is attained.

Figure 4.7: Maximum magnitude of the Ricci scalar $\mathcal{R}$ of the four MOTSs as function of d. (Figure adapted from [82].)

as isolated Schwarzschild black holes in the limit $d \to \infty$. Here, the separate ADM masses depend on the mass ratio q via $M^{(1)} \to 1/(1 + q)$ and $M^{(2)} \to q/(1 + q)$. For large d, we hence expect $A_1 \to 16\pi/(1 + q)^2$, i. e. the area decreases with q, and $A_2 \to 16\pi q^2/(1+q)^2$, where the area increases with q. Finally, no such simple argument exists for the area of $\mathcal{S}_{\text{inner}}$, which is seen to rapidly increase as d is reduced. At $d_{\text{bifurcate}}$, the two MOTSs $\mathcal{S}_{\text{outer}}$ and $\mathcal{S}_{\text{inner}}$ coincide and have the same area. At any smaller d where $\mathcal{S}_{\text{inner}}$ could be located, its area is larger than that of any of the other MOTSs.

The next quantity is depicted in Fig. 4.7 and it shows the maximum absolute
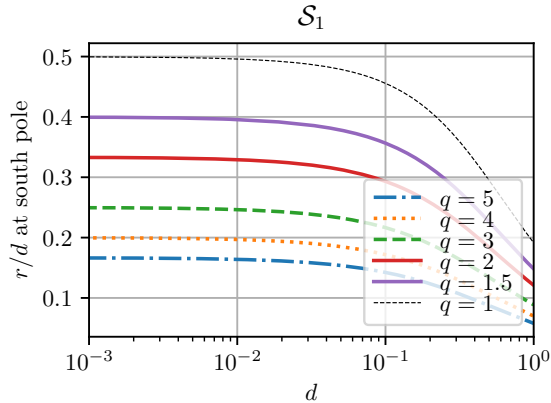
Figure 4.8: Behavior of the ratio r/d as $d \to 0$, where r is the *coordinate* distance of $\mathcal{S}_1$ to the puncture. Values asymptoting to a constant < 1 mean that $\mathcal{S}_1$ cannot intersect the other puncture (at x_2, cf. Eq. (4.8)). This constant is smaller for larger mass ratios. (Figure adapted from [82].)

value of the Ricci scalar along the four surfaces $\mathcal{S}$. For $\mathcal{S}_{\text{inner}}$, this complements the top-right panel of Fig. 4.5, which did not show the extremal value. As above, the four panels belong to the four horizons and the different curves represent the various mass ratios, with the x axis representing the distance parameter. The maximum $\|\mathcal{R}\|_\infty$ is found by first sampling $|\mathcal{R}|$ on a large number of points and then performing a numerical maximum search starting from the point of largest $|\mathcal{R}|$. Consistency with the theoretical prediction for $\mathcal{S}_{\text{outer}}$ can again be observed. To see this, consider the limiting case $d = 0$, where $\mathcal{S}_{\text{outer}}$ is the horizon of a Schwarzschild black hole and is geometrically a "round" sphere with constant Ricci scalar $\mathcal{R} = 2/R^2$, where R is the area radius defined by $R = \sqrt{A/4\pi} = 2M_{\text{irr}}$. As a result, the top-left panel of Fig. 4.7 is consistent with $\mathcal{R}$ converging to $1/2$ as $d \to 0$.

Note that for $\mathcal{S}_{\text{inner}}$ and $\mathcal{S}_2$, the curves extend to the smallest value of d for which the respective MOTS could be located numerically. For $\mathcal{S}_{\text{inner}}$, this is a point of very large variation compared with the behavior for other values of d. Accordingly, the end points, i.e. the maximal values of $\|\mathcal{R}\|_\infty$, are therefore not accurate enough to allow interpretation. The maximum of $|\mathcal{R}|$ for small d is actually a global *minimum* where $\mathcal{R} \ll 0$ (compare the top-right panel of Fig. 4.5).

The Ricci scalar of the smaller horizon $\mathcal{S}_1$ becomes small as $d \to 0$. Recall from Fig. 4.6 that in this limit, the area of $\mathcal{S}_1$ is rapidly increasing. This is compatible with the interpretation that $\mathcal{S}_1$ is "moving" across the Einstein-Rosen bride into the asymptotically flat end of the x_1 puncture. To further analyze this idea, Fig. 4.8 shows the ratio of the coordinate radius r of $\mathcal{S}_1$ at the south pole to d. The proper distance from the horizon to the puncture is, of course, infinite, which is why we show the coordinate radius. This still allows for a geometric interpretation: For the mass ratios considered here, r/d asymptotes to a value less than 1. This means that, asymptotically, $\mathcal{S}_1$ cannot intersect the puncture at x_2 as $d \to 0$.

We have found no deeper insight into the behavior of $\|\mathcal{R}\|_\infty$ of $\mathcal{S}_2$, which, in the bottom-right panel of Fig. 4.7, shows local minima and maxima as d is varied. Note

that the discontinuous slopes of the curves are due to showing the global maximum of $|\mathcal{R}|$, the location of which can jump along the surface.

4.3 The "vanishing" of MOTSs

An aspect that was briefly mentioned in the previous section, but is in fact central to the understanding of the behavior of marginal surfaces, is that they appear and disappear in our numerical analysis. Above, we showed how we were unable to locate $\mathcal{S}_{\text{inner}}$ and $\mathcal{S}_2$ at different values of the distance parameter d. For reference, we find for a mass ratio of $q = 4$

- $\mathcal{S}_{\text{outer}}$ is found for $0 \leq d \lesssim d_{\text{bifurcate}} \approx 0.6987$,

- $\mathcal{S}_{\text{inner}}$ is found for $d_{\text{vanish}}^{\text{inner}} \approx 0.1660 \lesssim d \lesssim d_{\text{bifurcate}}$,

- $\mathcal{S}_1$ is found for $0 < d$,

- $\mathcal{S}_2$ is found for $d_{\text{vanish}}^{(2)} \approx 0.1646 < d$.

The same holds for the other mass ratios with slightly different numerical values. The vanishing of $\mathcal{S}_{\text{outer}}$ and $\mathcal{S}_{\text{inner}}$ for $d \geq d_{\text{bifurcate}}$ can be understood as the horizons coinciding in the limit $d \to d_{\text{bifurcate}}$ at which point they "annihilate".

The lower limits of d are more interesting. It is true that $\mathcal{S}_{\text{inner}}$ is numerically more difficult to represent than $\mathcal{S}_2$. This poses the question of whether the difference $\Delta d := d_{\text{vanish}}^{\text{inner}} - d_{\text{vanish}}^{(2)} \approx 0.0014$ of the values of d at which we fail to locate them is due to numerical issues alone. This section will focus on this question and show that there is strong numerical evidence against such a numerical cause. The key here will be the analysis of the MOTS stability operator. However, even if numerical issues were to blame for Δd not vanishing, they cannot immediately explain the disappearance of $\mathcal{S}_2$, which shows no sign of becoming numerically difficult to locate.

Before turning to the stability operator, we shall first collect other indicators making an actual vanishing of $\mathcal{S}_{\text{inner}}$ and $\mathcal{S}_2$ plausible. First, from Figs. 4.2 and 4.3, one could naively assume that $\mathcal{S}_{\text{inner}}$ might merge with or touch one or both of the individual horizons. As argued previously and proven in [75], this would necessitate $\mathcal{S}_{\text{inner}}$ to cease to exist separately. In order to examine this possibility, we compute the proper distance of the intersections of $\mathcal{S}_{1,2}$ with the symmetry axis to the intersections of $\mathcal{S}_{\text{inner}}$ with this axis. In particular, we measure the distance of the "south poles" of $\mathcal{S}_{\text{inner}}$ and $\mathcal{S}_2$ and the "north poles" of $\mathcal{S}_{\text{inner}}$ and $\mathcal{S}_1$. Fig. 4.9 shows the former of these quantities and it is clear that no such merger happens. Instead, an interesting *increase* of this distance measure is seen to occur just before $\mathcal{S}_{\text{inner}}$ vanishes. The sudden change of behavior may be taken as a first hint that we approach a critical value of d.
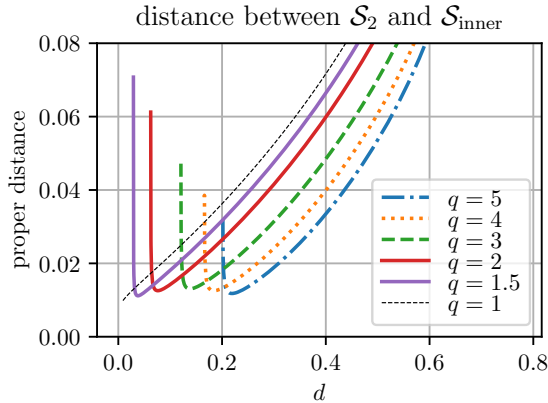
Figure 4.9: Proper distance of $\mathcal{S}_2$ and $\mathcal{S}_{\text{inner}}$ computed as proper length of the geodesic connecting the south pole of $\mathcal{S}_2$ with the south pole of $\mathcal{S}_{\text{inner}}$ along the z axis. As d is reduced, this distance initially decreases. However, shortly before $\mathcal{S}_{\text{inner}}$ vanishes the distance increases rapidly, showing that the two MOTSs do not merge. The case of equal masses behaves qualitatively different and no increase of separation can be observed for as long as $\mathcal{S}_{\text{inner}}$ could be tracked. (Figure adapted from [82].)

From Sec. 2.4 and in particular Definition 4 and the connection with the stability operator, we know that deformations of a MOTS $\mathcal{S}$ within the spatial slice Σ of a foliation are related to local existence of the dynamical horizon in that slicing. A particular class of such deformations takes a MOTS with $\Theta_{(\ell)} = 0$ into a surface of constant expansion $\Theta_{(\ell)} = \text{const} \neq 0$. Fig. 4.10 shows such surfaces of constant expansion close to $\mathcal{S}_{\text{outer}}$ and $\mathcal{S}_{\text{inner}}$. As expected, there are untrapped surfaces in a neighborhood of $\mathcal{S}_{\text{outer}}$, which lie completely outside, and trapped surfaces on the inside. This is the barrier property of $\mathcal{S}_{\text{outer}}$ discussed in Sec. 2.4 and an indication that it is stable. On the other hand, all surfaces of constant expansion we find close to $\mathcal{S}_{\text{inner}}$ intersect $\mathcal{S}_{\text{inner}}$ and lie partially outside and partially inside—an indication that $\mathcal{S}_{\text{inner}}$ is unstable, since it is not a barrier. $\mathcal{S}_1$ and $\mathcal{S}_2$ behave just like $\mathcal{S}_{\text{outer}}$ in this respect.

Note that Fig. 4.10 shows a case of $d = 0.65$, far from the critical values of d where horizons disappear. It turns out that for $\mathcal{S}_{\text{inner}}$ and $\mathcal{S}_2$, there is an upper limit c_{max} for the expansion for which surfaces of constant expansion can be located.

To understand this, first note that there may be many surfaces satisfying $\Theta_{(\ell)} = c$ in a spatial slice Σ, just like there are multiple MOTSs. Our numerical method for locating MOTSs and surfaces of constant expansion is naturally suited to find surfaces in a neighborhood of another surface, by using this other surface as an initial guess. If it is close enough to one of the solutions, the nonlinear search will quickly locate this surface. This enables us to look for surfaces of constant expansion in the neighborhood of a particular MOTS. We then gradually increase or decrease the value of c and use the previously found surface as initial guess. Suppose now $\mathcal{S}_c$ is a surface of constant expansion c in a neighborhood of $\mathcal{S}_{\text{inner}}$. Using this as starting point for locating a surface with constant expansion $c + \Delta c$ succeeds if Δc is small enough. These "steps" are then continued until the search fails for any $\Delta c \geq \varepsilon$, where ε controls how accurately we find the upper limit c_{max} and is chosen to be $\varepsilon = 10^{-8}$ in our searches.

Note that c_{max} will depend on d and, by definition, we have $c_{\text{max}}(d_{\text{vanish}}) = 0$. In
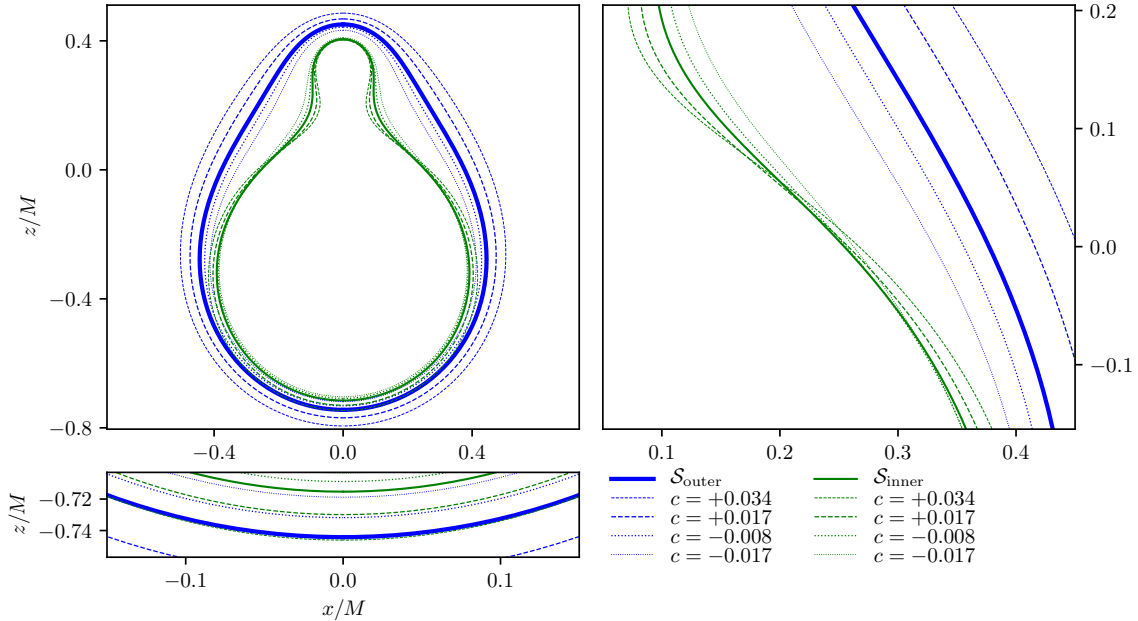
Figure 4.10: Surfaces of constant expansion in a Brill-Lindquist slice for $q = 4$ ($m_1 = 0.2, m_2 = 0.8$) and $d = 0.65$. Shown are the MOTSs $\mathcal{S}_{\text{outer}}$ (solid blue) and $\mathcal{S}_{\text{inner}}$ (thin solid green) along with nearby surfaces $\mathcal{S}^c_{\text{outer}}$ and $\mathcal{S}^c_{\text{inner}}$ of various positive and negative constant expansions $\Theta_{(\ell)} = c$. The surfaces $\mathcal{S}^c_{\text{outer}}$ do not cross $\mathcal{S}_{\text{outer}}$, consistent with it being a barrier for trapped ($c < 0$) and untrapped ($c > 0$) surfaces, cf. Sec 2.4. This does not hold for $\mathcal{S}_{\text{inner}}$, where all found surfaces $\mathcal{S}^c_{\text{inner}}$ cross $\mathcal{S}_{\text{inner}}$. (Figure adapted from [82].)

other words, approaching a critical value of d at which a horizon $\mathcal{S}$ vanishes, we find that c_{max} gradually decreases, reaching 0 at the point d_{vanish} of $\mathcal{S}$ vanishing, and then continues to negative values. That is, reducing d further, we get $c_{\text{max}} < 0$ and continue to find surfaces of constant expansion $c \leq c_{\text{max}} < 0$.

Fig. 4.11 shows an example of the structure of constant expansion surfaces around $\mathcal{S}_{\text{inner}}$ and $\mathcal{S}_{\text{outer}}$ in terms of parametric curves of area over expansion. This also demonstrates the behavior of c_{max} as d is varied. Since we consider time symmetric slices here, MOTSs are surfaces of (locally) minimal area. Therefore, we expect that a plot of the surface area over the expansion should have the MOTSs appear at local minima. Consistent with this, the blue dots marking the location of the MOTSs in Fig. 4.11 all lie at minima of the curves. The lowest dot in this plot belongs to the apparent horizons $\mathcal{S}_{\text{outer}}$ for four different values of d.[1] From $\mathcal{S}_{\text{outer}}$, we find surfaces of constant expansion larger than zero (i.e. to the right in the plot) and smaller than zero (to the left). The former lie outside $\mathcal{S}_{\text{outer}}$ while the latter are inside, cf. Fig. 4.10.

---

[1]Since the area of $\mathcal{S}_{\text{outer}}$ varies only slightly for the shown values of d, the four dots appear as only one dot in this figure.
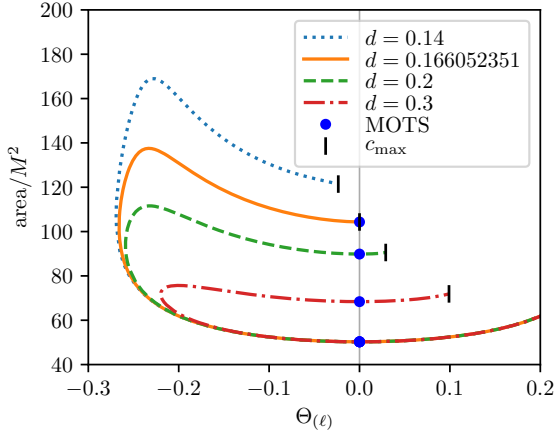
Figure 4.11: Parametric curves showing the area over the expansion of surfaces of constant expansion. We use a mass ratio of $q = 4$ and plot the curves for four values of d. The lowest blue dot marks the four different MOTSs $\mathcal{S}_{\text{outer}}$, which have very similar areas. The three remaining blue dots belong to $\mathcal{S}_{\text{inner}}$. For the case $d = 0.14$, $\mathcal{S}_{\text{inner}}$ could not be located. The shown endpoints of the curves mark the value of $c_{\max}$ for the respective distance d. (Figure adapted from [82].)

Reducing the expansion further, we see that the area increases up to a point where no further reduction of the expansion is possible. Going further inward and nearing $\mathcal{S}_{\text{inner}}$, the expansion starts to *increase* again and soon after, the area has a local maximum. If this procedure is to reach $\mathcal{S}_{\text{inner}}$, the expansion must increase and become zero at a point where the area has another minimum. Fig. 4.11 shows that this is what we find for values of $d > d_{\text{vanish}}^{\text{inner}}$, where we can generically extend to positive expansions. However, for $d = 0.14$, we see that $c_{\max} < 0$ and neither $\mathcal{S}_{\text{inner}}$ nor surfaces with constant negative expansion $0 > c > c_{\max}$ are found.

As a remark, Fig. 4.11 shows that there is a family of surfaces of constant expansion connecting $\mathcal{S}_{\text{outer}}$ and $\mathcal{S}_{\text{inner}}$. No such connection could be found for other horizon pairs as the punctures pose natural obstructions. However, this family is not a regular foliation of the space in this region, since the surfaces start to intersect each other when approaching $\mathcal{S}_{\text{inner}}$ (cf. Fig. 4.10).

4.3.1 MOTS Stability and Existence

The previous discussion presented several indications that the MOTSs are actually not present when the numerical algorithm fails to locate them. However, non-existence is inherently difficult to show numerically, and the discussion is as yet far from conclusive. We will therefore now turn to the stability operator introduced in Sec. 2.4. Recall from there that invertibility of the operator L_Σ implies existence of the dynamical horizon in a foliation of spacetime that contains the slice Σ. The numerical tool we use to analyze this invertibility is the spectrum of the operator. If it does not contain 0, the operator is invertible. We are here only considering time symmetric initial data. The horizon existence criterion hence picks out the parts of parameter space where the dynamical horizon does *not end* in Σ. In general, one expects that the points where one of the eigenvalues approaches 0 are the critical points beyond which the initial

data do not contain the horizon in question. A good illustration of this is $d_{\text{bifurcate}}$, where $\mathcal{S}_{\text{outer}}$ and $\mathcal{S}_{\text{inner}}$ are last found when increasing d. Fig. 4.12 shows that as d is increased, one of the eigenvalues, in this case the principal eigenvalue Λ_0, becomes zero at the same value of d, i.e. at $d_{\text{bifurcate}}$, for both MOTSs.
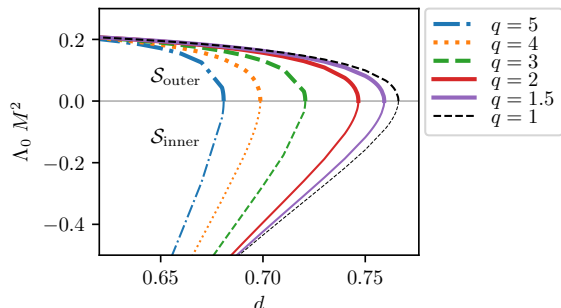
Fig. 4.13 shows the principal eigenvalue for all four MOTSs as function of d for the various mass ratios. For $\mathcal{S}_{\text{outer}}$ in the top-left panel, the behavior is as expected. It appears with vanishing principal eigenvalue, which then increases as d is reduced. For $d \to 0$, we obtain, for all mass ratios, the expected value of $\Lambda_0 = 1/4$ compatible with the value of a Schwarzschild horizon in Eq. (2.29). For $\mathcal{S}_1$, the bottom-left panel of Fig. 4.13 shows that Λ_0 is positive throughout, though it vanishes asymptotically for $d \to 0$, again compatible with the previous observations.

The more interesting cases are when $\mathcal{S}_{\text{inner}}$ and $\mathcal{S}_2$ disappear for decreasing d. The bottom-right panel of Fig. 4.13 clearly shows that the principal eigenvalue vanishes for *finite* values of $d > 0$ for all mass ratios. The exception is the case $q = 1$, which behaves qualitatively different. This provides clear support for $\mathcal{S}_2$ not being present in those configurations.

The situation is very different for $\mathcal{S}_{\text{inner}}$. Its principal stability eigenvalue immediately decreases from 0 and assumes large negative values. The behavior near the point it is born is shown in Fig. 4.12 and the full curves can be seen in the top-right panel of Fig. 4.13. Recall that the principal eigenvalue is defined as the eigenvalue with smallest real part. Since the stability operator is self-adjoint in this axisymmetric and time symmetric case, the full spectrum is real. Hence, in case $\Lambda_0 > 0$, no other eigenvalue can approach zero and the analysis of Λ_0 suffices. This does not hold for $\mathcal{S}_{\text{inner}}$, where $\Lambda_0 < 0$ throughout. Here, since $\Lambda_0 = 0$ initially, we look at the next higher eigenvalue, Λ_1, which is plotted in Fig. 4.14. This eigenvalue provides the missing link in understanding the vanishing of $\mathcal{S}_{\text{inner}}$, as it also goes to zero at precisely the point our algorithm ceases to find the MOTS. Again, the mass ratio $q = 1$ behaves differently in that we find no evidence for $d_{\text{vanish}}^{\text{inner}} > 0$ in this case.

These overview plots do not yet suffice for arguing that $\mathcal{S}_{\text{inner}}$ and $\mathcal{S}_2$ cease to exist

Figure 4.12: Principal eigenvalue Λ_0 of the stability operator L_Σ at the values of d where $\mathcal{S}_{\text{outer}}$ and $\mathcal{S}_{\text{inner}}$ appear for different mass ratios. The negative values (thin lines) belong to $\mathcal{S}_{\text{inner}}$ while the other values belong to $\mathcal{S}_{\text{outer}}$. (Figure adapted from [82].)

(a) $\mathcal{S}_{\text{outer}}$ appears with $\Lambda_0 = 0$ at $d_{\text{bifurcate}}$. Λ_0 then increases as d is reduced. For $d \to 0$, we have $\Lambda_0 \to 1/(4M_{\text{irr}}^2)$.

(b) Like $\mathcal{S}_{\text{outer}}$, $\mathcal{S}_{\text{inner}}$ appears with $\Lambda_0 = 0$. It then rapidly decreases to negative values as d is reduced.

(c) For the smaller MOTS $\mathcal{S}_1$, Λ_0 seems to vanish in the limit $d \to 0$, compatible with a diverging area (cf. Eq. (2.29)).

(d) The principle eigenvalue Λ_0 vanishes at *finite* values of d, consistent with $\mathcal{S}_2$ not existing for small d. The case of equal masses is qualitatively different and not easy to resolve numerically.

Figure 4.13: Principal eigenvalue Λ_0 of L_Σ for all four MOTSs as function of d for different mass ratios. (Figure adapted from [82].)

at different values of d. For this reason, we show a close-up of the relevant stability parameters (Λ_0 for $\mathcal{S}_2$ and Λ_1 for $\mathcal{S}_{\text{inner}}$) in Fig. 4.15, which provides conclusive numerical evidence for the outlined scenario. This figure shows the mass ratio $q = 4$, but the behavior is qualitatively the same for the other analysed mass ratios (with the usual exception of $q = 1$).

Finally, Fig. 4.16 contains the different values of d for which the two horizons $\mathcal{S}_2$ and $\mathcal{S}_{\text{inner}}$ vanish as a function of the mass ratio q. In this plot, the difference between

Figure 4.14: The second eigenvalue Λ_1 of L_Σ as function of d for different mass ratios. Λ_1 vanishes at *finite* values of d, consistent with $\mathcal{S}_{\text{inner}}$ not existing for smaller values. This happens at larger d for more unequal masses. Again, the case $q = 1$ is numerically difficult to resolve. (Figure adapted from [82].)
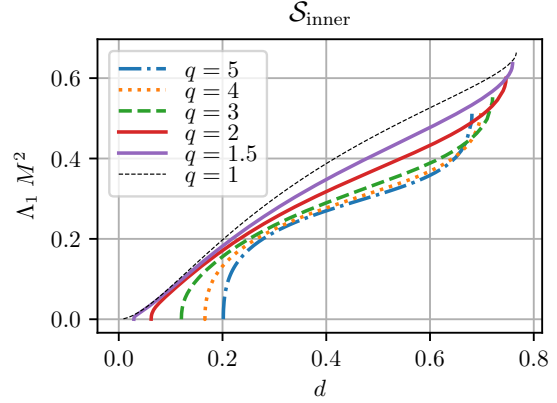
Figure 4.15: Close-up of Λ_0 for $\mathcal{S}_2$ and Λ_1 for $\mathcal{S}_{\text{inner}}$ near the values of d where they cannot be found anymore. Clearly, the two curves become zero at different values of d, indicating that the MOTSs cease to exist at different points. The shown curves are for a mass ratio $q = 4$ and look very similar for the other mass ratios, with the exception of $q = 1$ where neither curve becomes zero for as far as we can track the MOTSs. (Figure adapted from [82].)
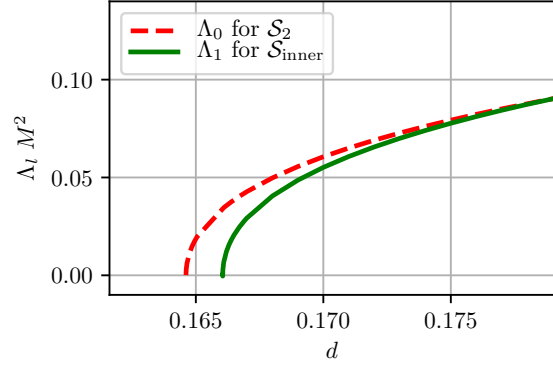
Figure 4.16: Distance parameters d_{vanish} at which $\mathcal{S}_2$ and $\mathcal{S}_{\text{inner}}$ vanish. The difference of the two values is difficult to see in this plot, but it is much larger than the numerical uncertainty, as explained in the text and visible in Fig. 4.15. (Figure adapted from [82].)
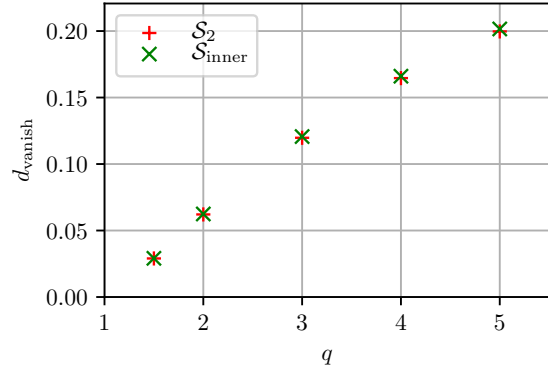
the values at which the two horizons vanish can hardly be made out by eye. However, the general q-dependence is clearly visible and d_{vanish} is seen to increase with higher mass ratio.

With the detailed understanding we gained from the study of the time symmetric

case, especially for the connection between MOTS stability and existence, we will now turn to the time evolution of MOTSs, yielding dynamical horizons not accessible via initial data alone.

Chapter 5

Results for Numerical Relativity Simulations

The study of the time-symmetric case in Chapter 4 already revealed a rich structure of MOTSs in a family of parametrized initial data. However, many questions of interest cannot be answered without an analysis of the dynamical horizons foliated by MOTSs in a spacetime. Among these are questions regarding the appearance and vanishing of MOTSs, whether dynamical horizons can connect in a binary black hole merger, as well as the evolution of physical properties such as the area, shear, and multipoles.

The results shown in this chapter are centered around a particular simulation of Brill-Lindquist initial data of two black holes merging in a head-on collision. After giving an overview of the dynamical horizons present in this simulation in Sec. 5.1, including the main results of the merger of MOTSs and the formation of self-intersections, Sec. 5.2 then describes how our numerical simulations are performed. This is followed by the specific new challenges for the MOTS finder in Sec. 5.3 where we also discuss the numerical convergence in detail. Sec. 5.4 will justify the MOTS merger with a detailed analysis of the numerical indications we find for this new phenomenon.

The signature of the dynamical horizons and the expansion of the ingoing null rays will be shown in Sec. 5.5, where a connection to the evolution of the area is analyzed. Sec. 5.6 studies in detail the eigenvalues of the MOTS stability operator and Sec. 5.7 concludes by discussing multipoles and fluxes through the horizons as well as their decay when the final state is approached.

Most of the results presented throughout this chapter have been published in [80, 81, 83, 84].

5.1 Dynamical Horizons in a Black Hole Head-on Collision

We start with the kind of initial data already analyzed in Chapter 4, namely Brill-Lindquist data, and perform a numerical evolution to obtain part of the corresponding spacetime. The parameters chosen for this simulation are $m_1 = 0.5$, $m_2 = 0.8$ and a distance parameter $d = 1.3 = M$. We will often state simulation times t in units of $\mathcal{M} := M/1.3$ rather than the usual units of ADM mass M.

The various MOTS configurations we encounter during the evolution are shown in Fig. 5.1. Initially, common horizons are not present in the data, but they form shortly after the beginning of the simulation. The notable phases can be summarized as follows:

- Initially, only the two individual horizons $\mathcal{S}_1$ and $\mathcal{S}_2$ exist (top-left panel of Fig. 5.1).

- At $t = t_{\text{bifurcate}} \approx 1.37460222\,\mathcal{M}$, the apparent horizon $\mathcal{S}_{\text{outer}}$ and the inner common MOTS $\mathcal{S}_{\text{inner}}$ form together. The top-right panel shows the MOTSs a short time afterwards. During this phase, $\mathcal{S}_{\text{outer}}$ quickly loses its initial distortions while $\mathcal{S}_{\text{inner}}$ becomes increasingly distorted. Though based on the horizon shapes in the numerical coordinates, this intuitive interpretation shall turn out to be supported by the analysis of geometrical quantities like the multipoles and shear of the horizons presented in the subsequent sections.

- $\mathcal{S}_{\text{inner}}$ encloses the individual MOTSs $\mathcal{S}_{1,2}$ from the outside, always keeping a (decreasing) distance. Various quantities presented below give strong numerical indication that $\mathcal{S}_{\text{inner}}$ *merges* with $\mathcal{S}_{1,2}$ at the moment they touch at $t_{\text{touch}} \approx 5.5378176\,\mathcal{M}$. The bottom-left panel of Fig. 5.1 shows the last time before t_{touch} at which our algorithm is able to locate $\mathcal{S}_{\text{inner}}$ separately.

- After t_{touch}, we find that $\mathcal{S}_{\text{inner}}$ and $\mathcal{S}_{1,2}$ all *continue* to exist separately, now intersecting each other. At this point, $\mathcal{S}_{\text{inner}}$ has self-intersections. The bottom-right panel of Fig. 5.1 shows this case at a time well after t_{touch}.

The numerical values presented above are given up to the number of decimal places we can show convergence for. This will be detailed in Sec. 5.3.3.

The history of how the MOTSs evolve can also be summarized by plotting their respective dynamical horizons $\mathcal{H}$. These are 3-dimensional manifolds and can be seen as the world tubes traced out by the MOTSs. Fig. 5.2 shows the four dynamical horizons we find in our simulation. $\mathcal{H}_1$ (in purple) and $\mathcal{H}_2$ (in red) are the world tubes of $\mathcal{S}_1$ and $\mathcal{S}_2$, respectively. In the figure, they are shown as 2-dimensional "tubes" starting at $t = 0$. Time progresses upwards here and the tubes hence extend vertically up to $t = 8\,\mathcal{M}$. Horizontal sections through these tubes are sections through the MOTSs, yielding the curves shown in Fig. 5.1. $\mathcal{H}_{\text{outer}}$ is the dynamical horizon formed by $\mathcal{S}_{\text{outer}}$ and it is shown in blue in Fig. 5.2. $\mathcal{H}_{\text{inner}}$ connects with $\mathcal{H}_{\text{outer}}$ at $t_{\text{bifurcate}}$ and is shown in green with a mesh to make it easier to see. The horizontal lines of this mesh are equidistant in t and the vertical lines are equidistant in the invariant angle θ (cf. Sec. 2.3). At t_{touch}, $\mathcal{H}_{\text{inner}}$ crosses $\mathcal{S}_{1,2}$ and subsequently lies inside the individual horizons. The right panel is a close-up of the part after t_{touch}, showing $\mathcal{S}_1$, $\mathcal{S}_2$ and the self-intersections of $\mathcal{S}_{\text{inner}}$. Fig. 5.2 is the quasilocal analog of the famous "pair-of-pants" picture [71] for the head-on collision of two black holes in terms of the event horizon.
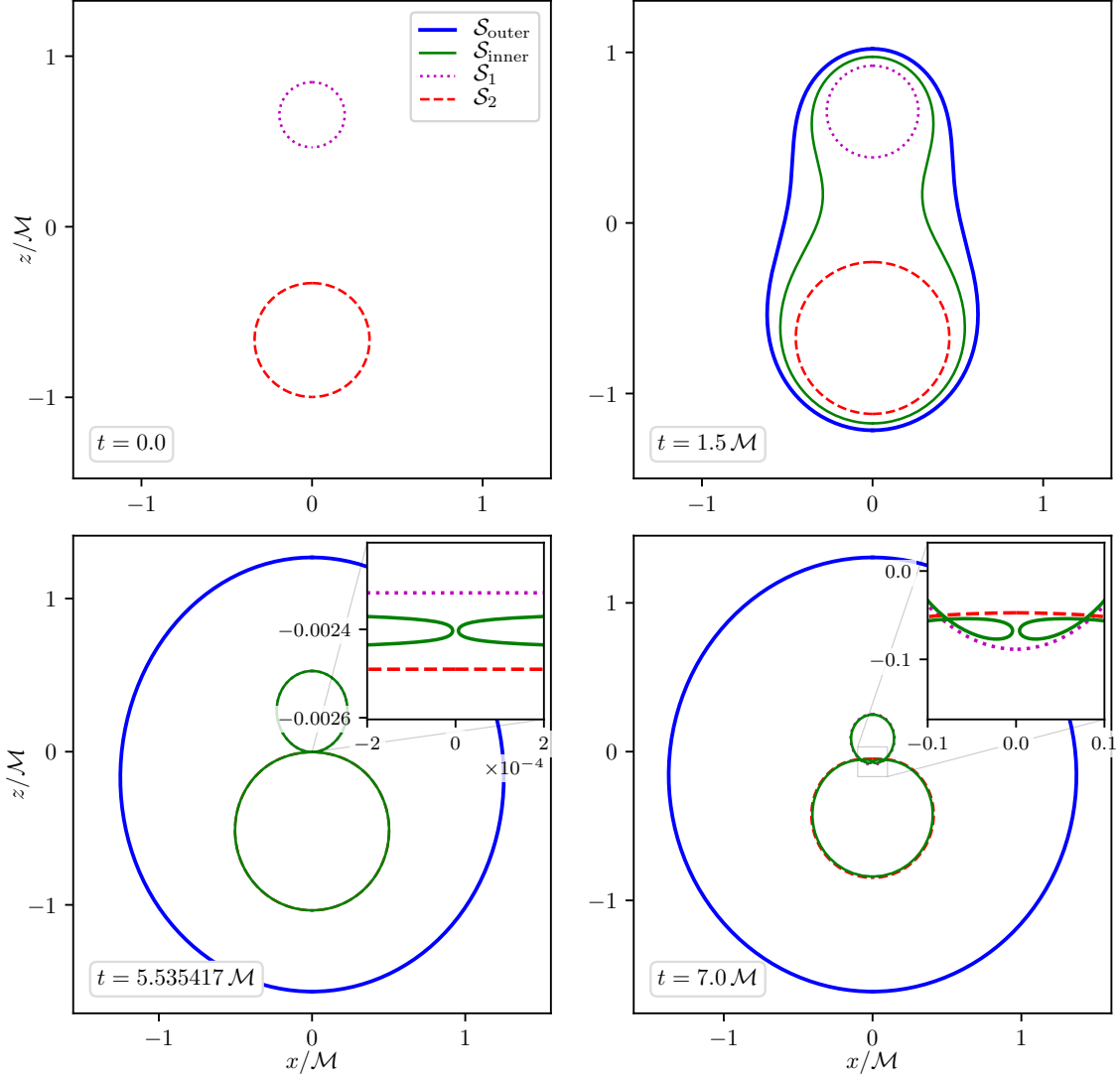
Figure 5.1: MOTSs found at various times during the simulation of a head-on collision of two non-spinning black holes. The initial data is a Brill-Lindquist configuration with $m_1 = 0.5$, $m_2 = 0.8$ and $d = 1.3$. The top-left panel shows that there are two separate MOTSs and no common horizons initially. Common MOTSs form at $t_{\text{bifurcate}} \approx 1.375\,\mathcal{M}$ and the top-right panel shows a time shortly after this where $\mathcal{S}_{\text{outer}}$ and $\mathcal{S}_{\text{inner}}$ have already clearly separated. The bottom-left panel shows the last time we can find $\mathcal{S}_{\text{inner}}$ before $t_{\text{touch}} \approx 5.538\,\mathcal{M}$, which is the time where $\mathcal{S}_{1,2}$ touch. The inset demonstrates that $\mathcal{S}_{\text{inner}}$ is very distorted and nearly pinches off between $\mathcal{S}_1$ and $\mathcal{S}_2$. The bottom-right panel shows a time well after t_{touch} where now $\mathcal{S}_{\text{inner}}$ is on the inside of $\mathcal{S}_{1,2}$. The inset shows that $\mathcal{S}_{\text{inner}}$ has developed self-intersections close to the intersection points of $\mathcal{S}_1$ and $\mathcal{S}_2$. (Figure adapted from [84].)
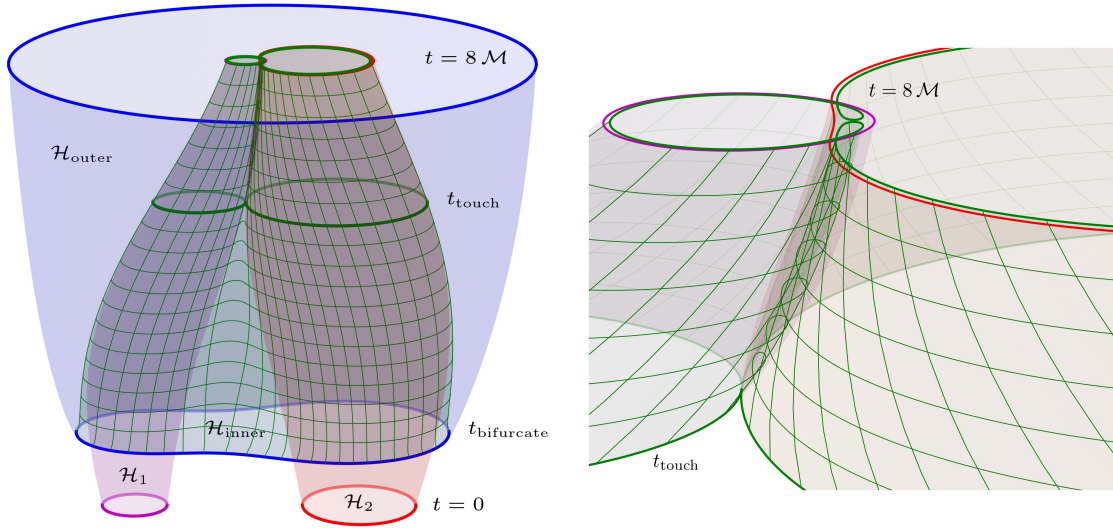
Figure 5.2: World tubes of the four MOTSs showing the analog of the "pair-of-pants" picture of the black hole merger now in terms of dynamical horizons. The left panel shows an overview containing the individual horizons $\mathcal{H}_1$ (purple) and $\mathcal{H}_2$ (red) as well as the outer common one $\mathcal{H}_{\text{outer}}$ (blue) and the inner common horizon $\mathcal{H}_{\text{inner}}$ (green with mesh). Indicated is the time $t_{\text{bifurcate}}$ where the common horizons form as well as the time t_{touch} where $\mathcal{S}_1$ and $\mathcal{S}_2$ touch and start to intersect. The right panel shows a close-up of the part after t_{touch} where the self-intersections of $\mathcal{H}_{\text{inner}}$ can clearly be made out. (Figure adapted from [80].)

5.1.1 Understanding the Self-intersection

One of the most surprising results in this numerical study is the existence of MOTSs that intersect themselves. Fig. 5.3 shows a close-up of such a case. Not only do the individual horizons intersect each other—such a case was already observed in [75]—but the curve representing $\mathcal{S}_{\text{inner}}$ has two double points at which it self-intersects. The full two-dimensional MOTS consequently has a *ring* at which it intersects itself. Staying in the curve-picture for this axisymmetric configuration, such a case can mathematically be understood in terms of an immersion $i : S^1 \to \Sigma$ of the circle S^1 into the Riemannian 3-manifold Σ. For the self-intersecting cases, the immersion i is not injective, though the push forward $i_* : TS^1 \to T\Sigma$ of the tangent bundles of course is.[1] Therefore, tangent spaces, normals, and quantities like the expansion $\Theta_{(\ell)}$ are well defined at the double points. Numerically, aside from $\mathcal{S}_{\text{inner}}$ not being star-shaped, nothing changes from a computational side, since even non-injective immersions locally are just embeddings.

By the nature of our algorithm, finding these self-intersecting MOTSs requires an

---

[1]This is in contrast to the other MOTSs, in which case i is injective and, since S^1 is compact, an *embedding.*
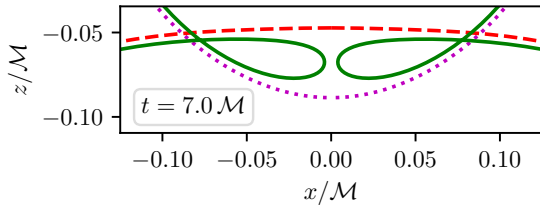
Figure 5.3: Close-up of the self-intersections of $\mathcal{S}_{\text{inner}}$ close to the points of intersection between $\mathcal{S}_1$ and $\mathcal{S}_2$.

appropriate reference surface and a good initial guess. In practice, we use the reference surface as initial guess in most cases. In the simulations, we find $\mathcal{S}_{\text{inner}}$ after t_{touch} by constructing a self-intersecting reference surface at one time not too close to t_{touch}, in this case at $t = 5.75 \, \mathcal{M}$. From this point, the MOTS is tracked forward and backward in time.

5.2 Numerical Simulations

As mentioned above, our simulations evolve the initial data introduced and thoroughly analysed in the previous chapter. In particular, we start with a Brill-Lindquist slice described in Sec. 4.1, containing two black holes at a moment of rest, with the punctures occurring at coordinates on the z axis. This makes the initial slice axisymmetric w. r. t. the z axis.

The parameter files containing the exact settings of the various simulations we have performed are available in the repository [85]. The various initial conditions differ by the mass ratio and initial distance of the two black holes. Several of these configurations have been simulated using different grid resolutions $1/\Delta x$ to verify convergence of the simulation as well as the accuracy of the MOTS finder. These two aspects will be discussed below and in Sec. 5.3.3, respectively. Most results presented in this chapter are obtained for a configuration with parameters $m_1 = 0.5$, $m_2 = 0.8$ and $d = 1.3$. This setup has been simulated with the resolutions $1/\Delta x = 60, 120, 240, 480, 960$.

The simulations themselves are carried out using the *Einstein Toolkit* [39, 69]. The initial data is generated by *TwoPunctures* [9] and the evolution is performed by an axisymmetric version of *McLachlan* [36], which in turn uses *Kranc* [57, 66] for generating C++ code. The evolution is based on the Baumgarte-Shapiro-Shibata-Nakamura (BSSN) formulation of the Einstein equations, using $1 + \log$ slicing and a Γ-driver shift condition [4, 6].

For the axisymmetric evolution, we do not need to evolve a full 3-dimensional slice Σ. Instead, our domain was set to only span the $y = 0$ plane for positive x coordinates,

i. e. we have

$$x \in [0, x_{\max}] \,, \qquad y = 0 \,, \qquad z \in [-x_{\max}, x_{\max}] \,, \qquad t \in [0, t_{\max}] \,. \qquad (5.1)$$

We impose Dirichlet conditions at the outer domain boundaries. This creates errors that "travel" from the boundaries to the interior. However, since the simulation evolves only a small amount of total time, we can chose $x_{\max}$ large enough to prevent any information from the boundary to reach the near-horizon region before the simulation end time $t_{\max}$.

Axisymmetry could be imposed using the *Cartoon* method [5] and we initially used this method for our simulations. It is based on the idea that spatial finite difference derivatives can be computed with the usual method, even involving points away from the y axis, by using the axisymmetry to *rotate* the x-z plane. This way, all necessary grid points in a small 3-dimensional volume around the $y = 0$ plane can be populated with data required for computing derivatives *on* that plane. However, higher than 4th order finite differencing produces large oscillations near the symmetry axis due to the larger rotation angles there. Subsequently, following the ideas of [87] extended to second derivatives, a new method for evolving axisymmetric data was developed.[2] It is based on the idea that the Lie derivatives in φ direction of axisymmetric tensors vanish by definition. Derivatives in y direction are then 0 or can be expressed in terms of (lower order) x derivatives.

In this grid-based evolution method, the spatial derivatives themselves are computed using a finite difference scheme. These schemes use linear combinations of a small number of values on a usually equidistant grid (the "stencil") to approximate the derivative at a particular point. The accuracy of this approximation can be controlled by the grid spacing Δx and the size of the stencil, i. e. the number of grid points used. The residual error of the computed derivative is proportional to a power of Δx. This power is called the *order* of the method. A method of order 2, 4, 6, or 8 uses, respectively, 3, 5, 7, or 9 grid points in each direction. An effect that becomes important as the grid spacing is reduced is the magnification of the floating point round-off error. The round-off error is a result of the finite representation of numeric values. The representation used throughout this work uses 64-bit floating point numbers with a maximum relative representation error of roughly 10^{-16}. Arithmetic operations involving these imperfect representations necessarily lead to an accumulation of errors. Finite difference schemes magnify this kind of error in the following way. Consider the

---

[2]The described analysis and development of the new evolution code was done by Erik Schnetter and not by the author.
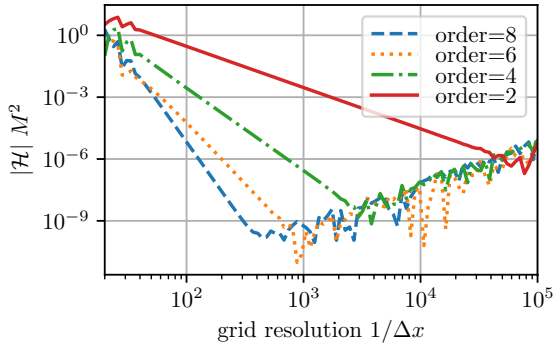
Figure 5.4: Error of second to eighth order finite difference derivatives as function of the grid resolution $1/\Delta x$. Shown is the Hamiltonian constraint computed at one point of radial coordinate $r \approx 0.24\,M$ in a slice of Schwarzschild spacetime in Kerr-Schild coordinates (cf. Sec. 3.4). Since this is an exact solution of the Einstein equations, we have $\mathcal{H} \equiv 0$ and hence show the error introduced by the discretization. (Figure adapted from [84].)

following centered second order accurate first derivative approximation

$$f'(x) \approx \frac{f(x + \Delta x) - f(x - \Delta x)}{2\Delta x} \,. \tag{5.2}$$

The error ε_f of the representation of the difference $f(x + \Delta x) - f(x - \Delta x)$ is then essentially independent of Δx. Consequently, the round-off error of the approximation of $f'(x)$ will be of order $\varepsilon_f/\Delta x$ and grow indefinitely as $\Delta x \to 0$. There is hence a balance between reducing the grid spacing to get a better approximation of the derivative and not reducing it so far that the round-off errors become dominant. Fortunately, this round-off error is independent of the order of the method used, so that higher order methods can reach much higher accuracies at the optimum grid spacing. This is shown in Fig. 5.4, where we evaluate the Hamiltonian constraint

$$\mathcal{H} := K_{ij}K^{ij} - K - R \tag{5.3}$$

using different grid spacings and second to eighth order finite differencing.

For our simulations, we chose to use the 6th order accurate finite difference scheme, which is significantly faster than the 8th order methods since the latter use larger stencils and a higher number of time integrator substeps. On the other hand, a 4th order method requires much higher resolutions to produce the same accuracy. Further details of our simulation are a 6th order Kreiss-Oliger artificial dissipation and a 6th order Runge-Kutta time integrator. We did not use mesh refinement.

Due to the dissipation, the effective spatial accuracy is reduced to 5th order. To show this, we plot in Fig. 5.5 the Hamiltonian constraint (5.3) close to a MOTS (the inner common MOTS $\mathcal{S}_{\text{inner}}$ in this case) for different grid spacings at two different simulation times. The left panel shows a time before t_{touch} and the right a time after t_{touch}. This allows for a comparison of the convergence for a case without self-intersections (left) and one with self-intersections (right). The plotted curves are scaled such that they lie on top of each other if we do have 5th order convergence. As can be seen, this is
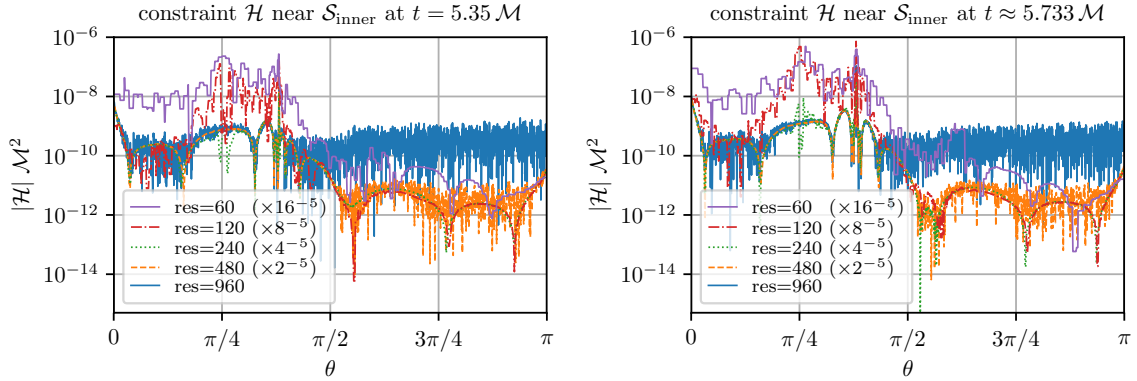
Figure 5.5: Hamiltonian constraint near the inner common MOTS at two simulation times for the grid resolutions $1/\Delta x = 60, 120, 240, 480, 960$. The constraint is computed at the grid points closest to $\mathcal{S}_{\text{inner}}$ and plotted as function of the invariant angle θ (cf. Sec. 2.3). The left panel shows a case before t_{touch} where no self-intersections are present and the right panel a case after t_{touch} where $\mathcal{S}_{\text{inner}}$ self-intersects. The curves have been scaled to account for 5th order convergence in the grid resolution, i.e. curves roughly agreeing confirm this convergence. (Figure adapted from [84].)

the case for resolutions of res $:= 1/\Delta x \geq 240$ in the first half and for res ≥ 120 in the second half of the curves. The difference between these two regions is that in the first, $\mathcal{S}_{\text{inner}}$ lies closer to one of the punctures, while in the second it is further away. This implies that the regions closer to the punctures require higher resolutions to enter the convergence regime. Another observation is that for the highest resolution of $1/\Delta x = 960$, the second half is slightly worse than 5th order convergence predicts. This is a case where the round-off error described above limits the accuracy. An important feature is that the two cases depicted do not show any significant differences, which indicates that the simulations themselves are equally accurate at both times and do not exhibit numerical problems that could be held responsible for the occurrence of self-intersections.

5.3 Finding MOTSs in Simulation Data

The numerical simulations produce data on a series of spatial slices Σ_t, where t is the time coordinate of the simulation. Specifically, we obtain data for

- the six independent components of the 3-metric h_{ij},

- the six independent components of the extrinsic curvature K_{ij},

- the lapse function α (a scalar) and its time derivative $\dot{\alpha}$, and

- the three components of the shift vector field β^i and their time derivatives $\dot{\beta}^i$.

Each of these 20 components is provided on a 2-dimensional grid on a $t = \text{const}$ section of the domain given by Eq. (5.1).

Our algorithm to locate MOTSs relies on evaluating the expansion and its various variational derivatives on a set of collocation points on a trial surface. This surface is numerically represented as a curve in the x-z plane. In general, the collocation points on this surface do not coincide with any of the grid points, making it necessary to interpolate the components of the above tensor fields. Similar to [94, section 6.1], we explored 5-point Lagrange interpolation and later decided to use quintic Hermite interpolation. These will now be described in turn.

5.3.1 Lagrange Interpolation

Lagrange interpolation of order n interpolates data using an nth order polynomial through $n + 1$ grid points. We employed a 5 point scheme as follows. For a point $p = (x, z) \in \mathbb{R}^2$ in the numerical domain, we first determined the closest grid point (x_i, z_j). The 2-dimensional interpolation is carried out on a 5×5 grid around this point by first interpolating along the five rows (x direction) and storing the five interpolated values (x, z_{j+n}), $n = -2, \ldots, 2$. These are then interpolated to (x, z).

The main drawback with this scheme is that the necessary moving of the considered grid across the numerical domain creates an interpolant that is either not continuous or not differentiable. With a 5 point scheme, the grid is moved half way between two grid points, creating discontinuous jumps in the interpolant.

5.3.2 Hermite Interpolation

Focussing first on 1-dimensional interpolation, this scheme is based on polynomials defined each by only two neighboring grid points. In contrast to Lagrange interpolation, the polynomial here is determined by the values *and a number of derivatives* at the grid points. We chose to use the first two derivatives, leading to a twice continuously differentiable interpolant. The six conditions (a value and two derivatives each on two points) then fully determine a polynomial of degree 5.

The same principle can be applied in two dimensions. In each "cell" of four grid points, we prescribe the four values and the first and second partial derivatives. This means that, at each of the four grid points (x_k, z_l), we use the 9 values

$$\partial_x^i \partial_z^j f(x_k, z_l), \qquad i, j = 0, 1, 2, \tag{5.4}$$

where $f : \mathbb{R}^2 \to \mathbb{R}$ is one of the interpolated tensor component functions. These 36

values are used to determine the 36 coefficients c_{ij} of the interpolating polynomial

$$f_{\text{interp}}(x, z) = \sum_{i,j=0}^{5} c_{ij} \, x^i z^j \, . \tag{5.5}$$

It should be noted here that the partial derivatives used in Eq. (5.4) must be approximated numerically by a finite difference scheme, since the component functions are only available on the numerical grid. For finding MOTSs, we choose the same 6th order finite difference scheme that is used in the evolution described above.

5.3.3 Convergence

Before discussing physical properties of the horizons, their reliability, that is, the convergence behavior of the individual MOTSs, should be analyzed. Are the self-intersecting instances of $\mathcal{S}_{\text{inner}}$ actually just numerical artifacts caused by extremely distorted surfaces that our algorithm simply cannot resolve? To answer this question, this section presents a detailed convergence analysis for all horizons, focusing on $\mathcal{S}_{\text{inner}}$ at one time before, and one time after t_{touch}. The former has no self-intersections, while in the latter case, $\mathcal{S}_{\text{inner}}$ is self-intersecting. The simulations were already shown in Fig. 5.5 to be reliable near $\mathcal{S}_{\text{inner}}$ at these two times.

There are multiple measures of convergence. First, we can vary the resolution of the simulation grid and look at the coordinate shape and residual expansion of the MOTSs we find. The latter was already used in Sec 4.2.1 to determine the reliability of our results. The next quantity to vary is the pseudospectral resolution, i.e. the number of basis functions used to represent the horizon function. For sufficiently well-behaved solutions and the correct choice of basis, the error of an expansion into a Fourier-kind basis should decay exponentially when increasing this resolution. We will then track the residual expansion for all MOTSs throughout the simulation to ensure the heuristics for choosing a sufficient resolution have picked correct values at each analysed time step. Finally, the dependence of the numerical values for $t_{\text{bifurcate}}$ and t_{touch} on the grid resolution of the simulation can be used to give a conservative estimate of the accuracy of these values.

We begin with the convergence of the *coordinate representations* of $\mathcal{S}_{\text{inner}}$ at $t = 5.35 \, \mathcal{M}$, which is before $t_{\text{touch}} \approx 5.5378176 \, \mathcal{M}$, and at $t \approx 5.733 \, \mathcal{M}$, which lies after. Fig. 5.6 shows the maximum coordinate distance of a MOTS found at a particular grid resolution to the respective MOTS found using the highest resolution simulation. We clearly see convergence of the shapes as the resolution is increased with no appreciable difference between the cases with and without self-intersections.

A more meaningful measure for convergence is the next quantity: the residual expansion, which corresponds to the maximum value of $|\Theta_{(\ell)}|$ on the MOTS (i.e.
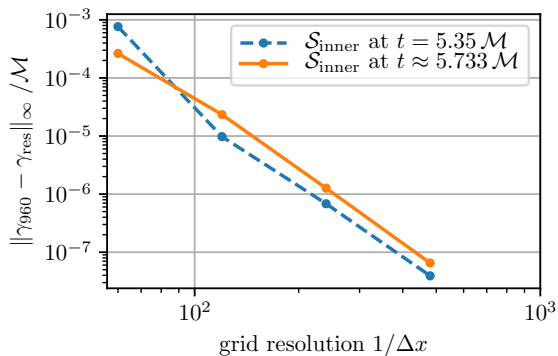
Figure 5.6: Maximum coordinate distance between the curves γ representing the MOTSs in simulations of various grid spacings Δx. Shown is the distance to the MOTS found in the highest resolution simulation of $1/\Delta x = 960$. The dotted blue curve refers to a time before and the solid orange curve to a time after t_{touch}. (Figure adapted from [84].)
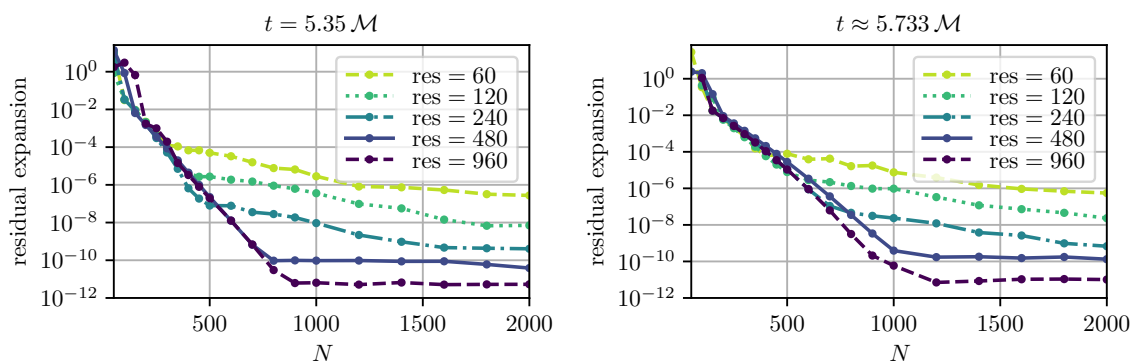
Figure 5.7: Residual expansion, i.e. maximum of $|\Theta_{(\ell)}|$ measured between collocation points, as function of the pseudospectral resolution N for various grid resolutions $1/\Delta x$. The two panels show again a case before t_{touch} (left) and a case after (right). (Figure adapted from [84].)

computed *between* the collocation points). Fig. 5.7 shows that this error clearly falls off exponentially, which is indicated by the nearly straight line segments of negative slope in the log-linear plot. For each resolution of the simulation grid, this figure shows a convergence plot obtained by varying the pseudospectral resolution of the MOTS representation at the same two times as before. Again, there is no significant difference in the behavior with (right panel) and without self-intersections (left panel). Another notable feature is the different plateaus, which signify that other convergence limiting effects become dominant at certain pseudospectral resolutions. These plateaus occur at much higher errors when the grid resolution is lower.

Note that for lower grid resolutions, the plateaus still have a small negative slope. In this regime, the solutions adapt to unwanted features introduced by the interpolation on the numerical grid. Here, the slope is controlled by the smoothness of these added features, which become less smooth with higher grid resolutions. For the highest two grid resolutions of $1/\Delta x = 480, 960$, this *overfitting* becomes negligible.
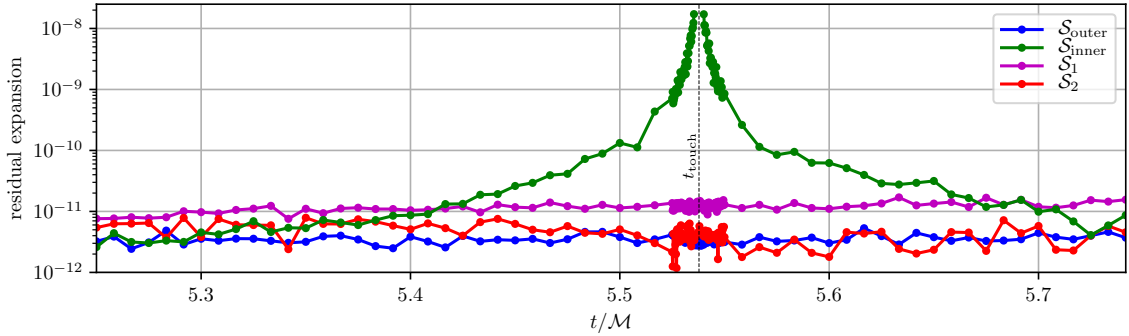
Figure 5.8: Residual expansion of the four MOTSs as function of time close to t_{touch} for the simulation of highest resolution $1/\Delta x = 960$. As $\mathcal{S}_{\mathrm{inner}}$ approaches the state of having a cusp at t_{touch}, the residual expansion grows due to the large increase in pseudospectral resolution N causing accumulation of round-off errors. (Figure adapted from [84].)

Clearly, a numerical algorithm for choosing the pseudospectral resolution needs to avoid increasing the resolution far into this slowly decaying region. Without accounting for this effect, the numerical searches quickly failed in case of low grid resolutions as the pseudospectral resolutions were reaching our cutoff of $12\,000$ collocation points. A heuristic algorithm subsequently prevented the resolutions to grow into very slowly converging regimes, where the meaning of "slow" is determined from an initial phase of fast convergence.

However, in order to ensure this method does not cut off the resolution too early, we monitor the residual expansion for all horizons at all time steps for sudden variations. Fig. 5.8 shows a subset of this data for times before and after t_{touch}. Each dot represents the residual expansion of a particular MOTS for the simulation with highest resolution $1/\Delta x = 960$. For $\mathcal{S}_{\mathrm{inner}}$, we find that the residual expansion increases very close to t_{touch} where we chose to disregard results with expansions $\|\Theta_{(\ell)}\|_\infty \gtrsim 10^{-8}$. The increased error can be attributed to the formation of the cusp in the horizon shape, requiring a much larger pseudospectral resolution. This in turn increases the accumulation of round-off errors. Interestingly, about $0.1\,\mathcal{M}$ away from t_{touch}, $\mathcal{S}_{\mathrm{inner}}$ is as accurate as the other MOTSs. In fact, $\mathcal{S}_1$ is the least accurate at later times, which is well explained by its proximity (in coordinates) to the puncture.

The above tests for accuracy strongly indicate that $\mathcal{S}_{\mathrm{inner}}$ exists and is found with high accuracy by our algorithm before *and after* t_{touch}, where in the latter case it possesses self-intersections.

We are not able to reliably track $\mathcal{S}_{1,2}$ and $\mathcal{S}_{\mathrm{inner}}$ beyond about $t \approx 8\,\mathcal{M}$. This is due to the used gauge conditions, which make them move very close to the punctures in coordinates, where the geometry is underresolved in the simulation. This effect can be seen in Fig. 5.1 as an apparent *shrinking* of the horizons $\mathcal{S}_{1,2}$. This only happens
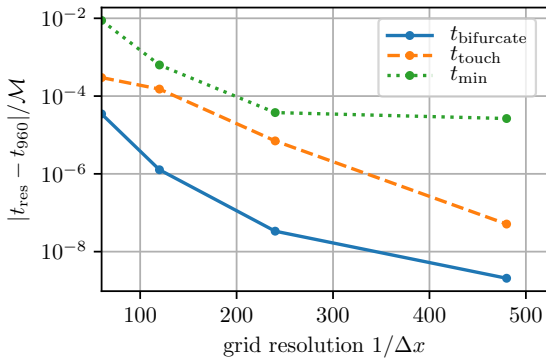
**Figure 5.9:** Convergence of three different times characteristic for the simulation. The first (blue solid line) is the time $t_{\text{bifurcate}}$ where the two common horizons form. The dashed orange line shows t_{touch} where $\mathcal{S}_{1,2}$ touch. At t_{min}, the area of $\mathcal{S}_{\text{inner}}$ has its first local minimum. The full merger analysis has been carried out for the grid resolutions $1/\Delta x = 60, 120, 240, 480, 960$ and these times have been determined in each case. We plot here the difference to the results for the $1/\Delta x = 960$ resolution as function of $1/\Delta x$, which gives an estimate of the accuracy of these times. (Figure adapted from [84].)

in coordinate space and we will see later that, e.g., the areas of $\mathcal{S}_1$ and $\mathcal{S}_2$ are, in fact, non-decreasing. The gauge conditions used in the simulations were analyzed in more detail by Evans et al. in [41]. Using adaptive mesh refinement, they were able to resolve the individual horizons up to much later simulation times and could show that proper time essentially halts in the central region.

Finally, by determining the various relevant times in the different simulations, we can give an estimate of their accuracy. Fig. 5.9 shows that the time $t_{\text{bifurcate}}$ of formation of the two common horizons $\mathcal{S}_{\text{outer}}$ and $\mathcal{S}_{\text{inner}}$ is the most precise, with a difference smaller than $10^{-8}\,\mathcal{M}$ for the highest two resolutions. In these two simulations, the time at which $\mathcal{S}_{1,2}$ touch and start to intersect, t_{touch}, varies by less than $10^{-7}\,\mathcal{M}$. The least accurate value shown in Fig. 5.9 is t_{min}. This is the time at which $\mathcal{S}_{\text{inner}}$ has the first local *minimum* in its area evolution. This will be shown in more detail in Sec. 5.5.3. Here we just note that the accuracy of this value is at least $10^{-4}\,\mathcal{M}$.

5.4 Merger of MOTSs

With the accuracy and reliability of both the performed simulations as well as the location of the MOTSs shown, this section will now turn towards the merger of MOTSs described in Sec. 5.1. One way to visualize this merger is in terms of physical quantities that can be tracked along the dynamical horizons. Various such quantities will be discussed below, but the bifurcation and merger scenario is most easily understood in terms of the evolution of areas of the four different MOTSs. We therefore show in Fig. 5.10 the area evolution in the left panel. If $\mathcal{S}_{\text{inner}}$ is to coincide with $\mathcal{S}_1 \cup \mathcal{S}_2$ at t_{touch}, then clearly its area A_{inner} must equal the sum $A_1 + A_2$ of the areas of the two individual MOTSs. The area curves of $\mathcal{S}_{\text{inner}}$ and $\mathcal{S}_{1,2}$ in Fig. 5.10 consequently connect at t_{touch}. This creates the link between the initial state before the merger—the state where there are only two separate black holes far apart—and the final state
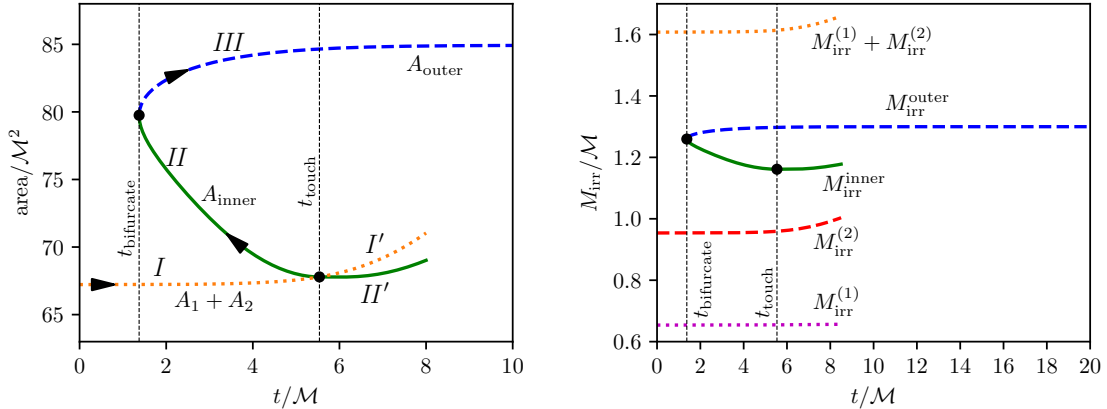
Figure 5.10: Areas (left) and irreducible masses (right) of the four horizons as function of time. The left panel shows that the sum of the areas of the individual MOTSs (segments *I* and *I'*) increases and coincides with the area A_{inner} (segments *II* and *II'*) at the time t_{touch}. On the other hand, A_{inner} connects smoothly at $t_{\text{bifurcate}}$ with the area of $\mathcal{S}_{\text{outer}}$ (segment *III*). Details and the non-monotonicity of segment *II* will be discussed in Sec. 5.5.3. The right panel shows that the irreducible masses of the horizons do not provide an intuitive interpretation of the MOTS merger due to the interaction energy $M - (M_{\text{irr}}^{(1)} + M_{\text{irr}}^{(2)})$ they include. See text for details. (Figures adapted from [80, 83].)

consisting of a single Kerr (or in our case Schwarzschild) black hole. The connected history of the merger in terms of MOTSs hence features no discontinuous jumps, but the connection is not smooth. The left panel of Fig. 5.10 indicates the path along this connected history with arrows following the different segments. The area sum of $\mathcal{S}_{1,2}$ increases slightly along segment *I* (before t_{touch}) and *I'* (after t_{touch}), while the area of $\mathcal{S}_{\text{inner}}$ is obviously not monotonic along segments *II* and *II'*. $\mathcal{S}_{\text{outer}}$ has monotonically increasing area shown as segment *III*. The connected path consists of $I \to II \to III$ (where *II* is followed backwards in time). We note here that even along this connected path, the area is *not* monotonically increasing, though it does increase overall, of course. This will be discussed in detail in Sec. 5.5.3.

Since the black holes are non-spinning, the area directly leads to the irreducible mass via Eq. (4.11). Fig. 5.10 shows in the right panel the evolution of these masses for the four horizons as well as the sum $M_{\text{irr}}^{(1)} + M_{\text{irr}}^{(2)}$. This sum does not equal the mass of $\mathcal{S}_{\text{inner}}$ at t_{touch} but lies significantly higher. It is also larger than the ADM mass of $M = 1.3$ in this simulation, which can be interpreted as being due to the binding energy between the individual black holes [68, 93].

Several other quantities tracked along the horizons justify the proposed merger of $\mathcal{S}_{\text{inner}}$ with $\mathcal{S}_{1,2}$. Fig. 5.11 shows four curves that each need to become zero if the merger is to happen. The first is the red solid line, showing the proper distance of the south pole of $\mathcal{S}_1$ and north pole of $\mathcal{S}_2$. Let z_1 and z_2 be the respective z coordinates of
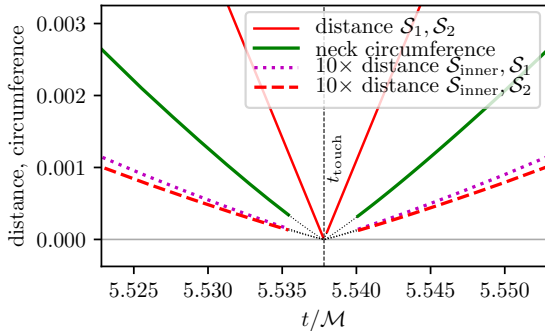
Figure 5.11: Various quantities we track to indicate the merger of $\mathcal{S}_{\text{inner}}$ with $\mathcal{S}_1 \cup \mathcal{S}_2$. The solid red line shows the distance of $\mathcal{S}_{1,2}$, which defines the time t_{touch} as its root. The neck circumference of $\mathcal{S}_{\text{inner}}$ as well as the respective proper distances of $\mathcal{S}_{\text{inner}}$ to $\mathcal{S}_1$ and $\mathcal{S}_2$ is then extrapolated from the last instances where $\mathcal{S}_{\text{inner}}$ could be located (the latter two multiplied by 10 to make them clearly visible here). See text for the precise definition of the shown quantities. The roots of the extrapolated curves agree within $\Delta t \approx 10^{-5} \, \mathcal{M}$ with t_{touch}. (Figure adapted from [83].)

these points. The distance is computed as the proper length of the geodesic along the symmetry axis connecting these two points. By definition, the length of this geodesic is non-negative and the time of its vanishing is, again by definition, the time t_{touch}. To accurately determine this time, however, we count the length as positive when $z_1 > z_2$ and as negative for $z_1 < z_2$. An interpolation of the distances we obtain at the discrete time steps of the simulation allow us to find t_{touch} to an accuracy of about $10^{-7} \, \mathcal{M}$, as was shown in Sec. 5.3.3.

The other quantities shown in Fig. 5.11 are computed fully independently from this distance. They are the proper circumference of the "neck" of $\mathcal{S}_{\text{inner}}$ and two different distance measures between $\mathcal{S}_{\text{inner}}$ and the individual MOTSs. The neck is defined as follows. Consider an axisymmetric MOTS $\mathcal{S}$ represented by a curve, whose surface of revolution is $\mathcal{S}$. Fixing a point on the curve, we take the proper length of the curve obtained by rotating this point along the φ direction by 2π. This length is, of course, zero at the two poles. However, for $\mathcal{S}_{\text{inner}}$, there is a local minimum at the point at which the cusp forms at t_{touch}. In Fig. 5.1, this point can be seen in the two insets in the bottom panels, where it lies approximately at the point of closest approach to the axis $x = 0$.

The two distances of $\mathcal{S}_{\text{inner}}$ to $\mathcal{S}_{1,2}$ are defined as proper lengths of geodesics connecting the north poles of $\mathcal{S}_{\text{inner}} \leftrightarrow \mathcal{S}_1$ and the south poles of $\mathcal{S}_{\text{inner}} \leftrightarrow \mathcal{S}_2$ on the z axis, respectively.

All these quantities can be tracked up to a small time interval around t_{touch}, where $\mathcal{S}_{\text{inner}}$ almost pinches off and becomes numerically difficult to represent. For reference, in the simulation with the highest grid resolution $1/\Delta x = 960$, we find $\mathcal{S}_{\text{inner}}$ the last time at about $2.4 \times 10^{-3} \, \mathcal{M}$ before and $2.3 \times 10^{-3} \, \mathcal{M}$ after t_{touch}. In this resolution, one time step is $\Delta t \approx 2.6 \times 10^{-4} \, \mathcal{M}$, which means we approach the horizon merger up to about 9 time slices from both sides. We get equally close for the lower resolution of $1/\Delta x = 480$. Since the size of the simulation time steps is coupled to the grid resolution, this means that we approach the merger up to about 4 slices from each

side. Note that $\mathcal{S}_{\mathrm{inner}}$ has self-intersections from the first time it is found after t_{touch}.

Extrapolating these curves (dotted lines in Fig. 5.11) shows that they all become zero within $\sim 10^{-5}\,\mathcal{M}$ of t_{touch}, which we take as strong numerical indication that the time of $\mathcal{S}_{\mathrm{inner}}$ pinching off and the time of $\mathcal{S}_{1,2}$ touching coincide.

5.5 Geometric Properties of the Dynamical Horizons

The previous section presented the general properties of the MOTS evolution, including their merger and formation of a connected history taking us from the initial separate horizons to the final one. This section will continue this analysis and focus on certain geometric properties which characterize the dynamical horizons foliated by the MOTSs. One result will be that in practice, we do encounter kinds of such dynamical horizons not usually considered in the literature. Even the outermost MOTS, the apparent horizon, possesses unusual properties, albeit for a very short time directly after formation. The results will be related to the behavior of the areas already mentioned in the previous section, with a focus on their (non-)monotonicity for $\mathcal{S}_{\mathrm{inner}}$. The case studied here in detail is the same as before, starting with a Brill-Lindquist configuration of two black holes at rest and bare masses $m_1 = 0.5$, $m_2 = 0.8$ and $d = M$.

The horizons usually considered in dynamical situations are those meant by the "traditional" definition of a dynamical horizon. In the terminology defined in Sec. 2.2, these are *future spacelike dynamical horizons*. Here, "future" refers to the expansion $\Theta_{(n)}$ of the ingoing null rays to be negative everywhere and "spacelike" to the signature of the world tube, i. e. its induced metric has signature $(+++)$. The expansion $\Theta_{(n)}$ is a property of a MOTS, while the signature requires knowledge of the time evolution of the MOTS. We will now in turn present $\Theta_{(n)}$, which we will sometimes refer to as *ingoing expansion*, and the signature for all four dynamical horizons. The following two sections focus primarily on a descriptive presentation of the results. These will be interpreted and related to the status of the area increase law in Sec. 5.5.3.

5.5.1 The Expansion of the Ingoing Null Rays

The two individual MOTSs $\mathcal{S}_{1,2}$ initially have vanishing $\Theta_{(n)}$. This is due to the initial data being time symmetric, which implies $\Theta_{(n)} = \Theta_{(\ell)} = 0$ on a MOTS. However, immediately afterwards we have $\Theta_{(n)} < 0$ everywhere. This can be seen in the top two panels of Fig. 5.12. The two panels in the middle row of this figure show the sign of $\Theta_{(n)}$ for $\mathcal{S}_{\mathrm{outer}}$. This holds the first interesting feature, as we find a very short time of $\Delta T \approx 0.056\,\mathcal{M}$ with a small region of *positive* ingoing expansion. This early part is shown in the middle-right panel of Fig. 5.12. The part with $\Theta_{(n)} > 0$ corresponds to a ring near the equator of $\mathcal{S}_{\mathrm{outer}}$, which quickly becomes thinner and then vanishes.
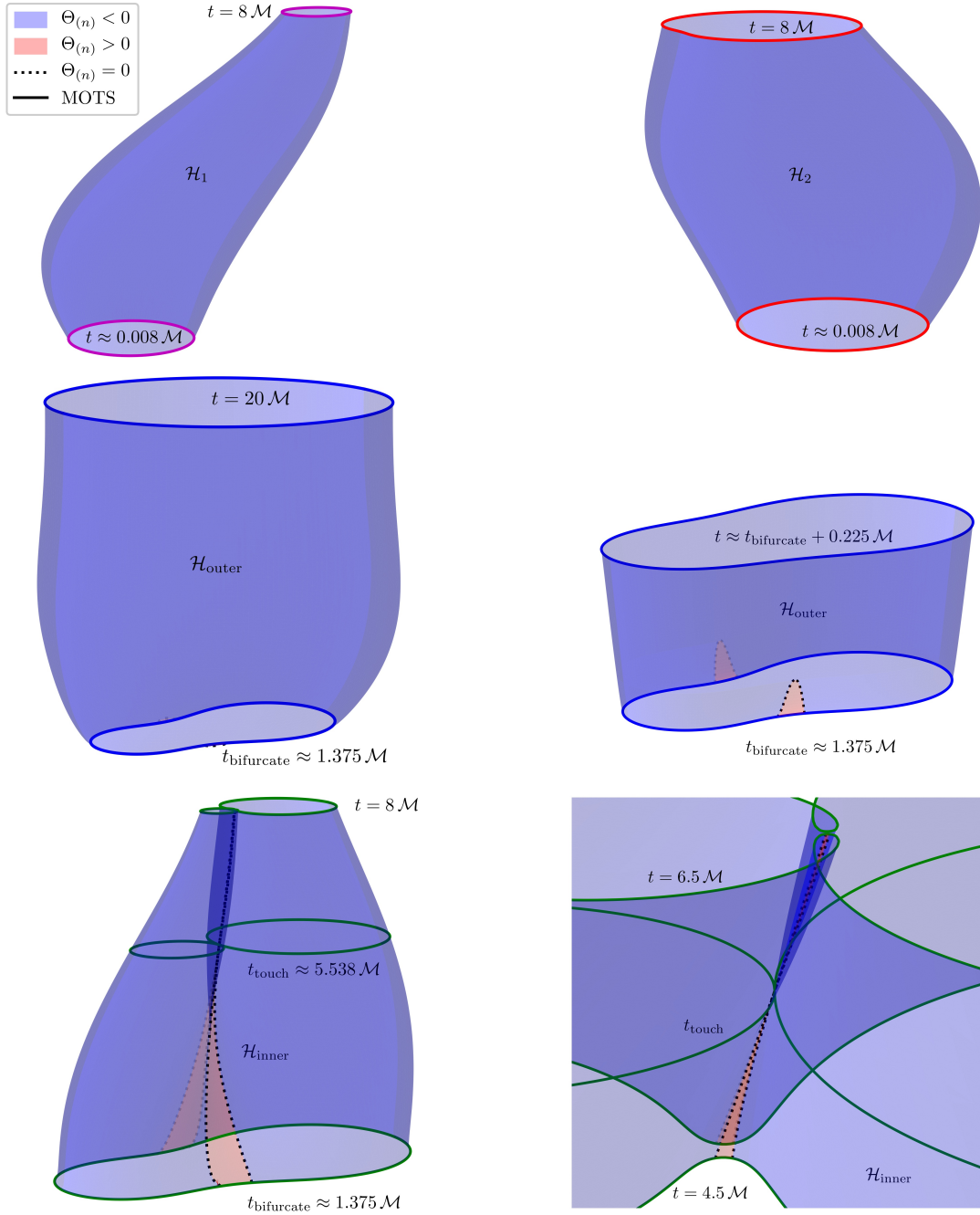
Figure 5.12: Sign of the ingoing expansion $\Theta_{(n)}$ for all four dynamical horizons. For the individual horizons $\mathcal{H}_{1,2}$ (top row), the sign is purely negative. $\mathcal{H}_{\text{outer}}$ (middle row) has a small portion at the beginning where the sign is positive on a region near the equator (see close-up in the middle-right panel). The bottom row shows that $\mathcal{H}_{\text{inner}}$ has a region with $\Theta_{(n)} > 0$ through the whole evolution, which momentarily vanishes at t_{touch}, see close-up on the bottom-right. (Parts of this figure adapted from [80].)
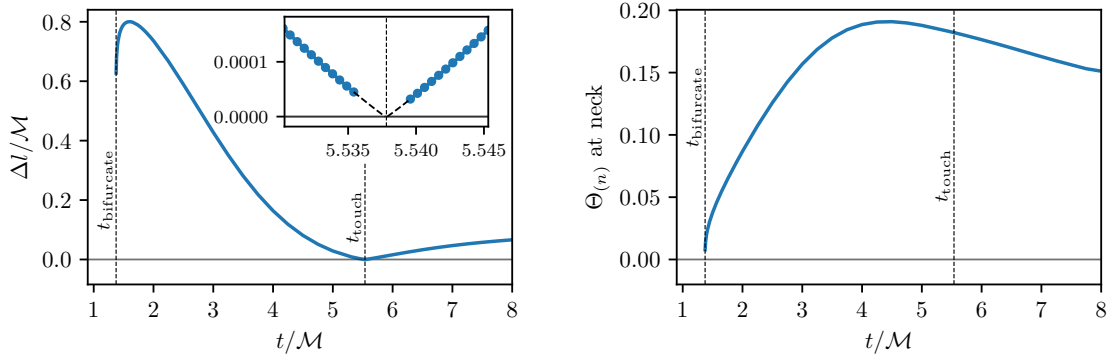
Figure 5.13: Analysis of the ingoing expansion $\Theta_{(n)}$ near the neck of $\mathcal{S}_{\text{inner}}$. The left panel shows a measure of the width of the region with $\Theta_{(n)} > 0$ along $\mathcal{H}_{\text{inner}}$ shown in Fig. 5.12. The quantity Δl is computed as the proper length of the curve segment of $\mathcal{S}_{\text{inner}}$ having $\Theta_{(n)} > 0$. The dashed line in the inset is an extrapolation of this curve and reaches zero from both sides within $\Delta t \approx 10^{-4}\,\mathcal{M}$ from t_{touch}. The right panel shows the value of $\Theta_{(n)}$ at the neck of $\mathcal{S}_{\text{inner}}$, which seems to smoothly cross the time t_{touch}.

Figure 5.14: Average ingoing expansion as function of time. For all times $t > 0$, the average $\overline{\Theta_{(n)}}$ is negative for all four horizons despite some regions having $\Theta_{(n)} > 0$. (Figure adapted from [80].)
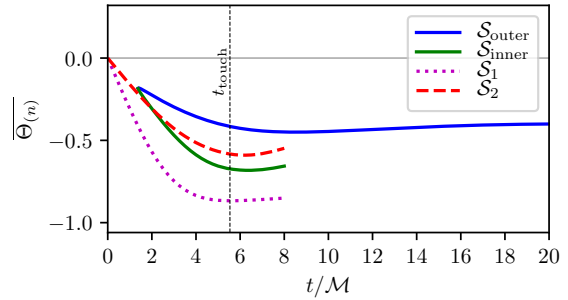
Such a region with positive ingoing expansion also exists for $\mathcal{S}_{\text{inner}}$, which is consistent with $\mathcal{S}_{\text{inner}}$ smoothly connecting with $\mathcal{S}_{\text{outer}}$. However, in the bottom row in Fig. 5.12 it can be seen that this region persists and becomes smaller, vanishing momentarily at t_{touch} and then reappearing afterwards. To show this, we plot in the left panel of Fig. 5.13 the proper length Δl of the curve segment of $\mathcal{S}_{\text{inner}}$ along which $\Theta_{(n)} > 0$. This becomes smaller towards t_{touch} and the extrapolated intersections with zero coincide with t_{touch} to about $\Delta t \approx 10^{-4}\,\mathcal{M}$. On the other hand, the right panel of Fig. 5.13 shows that the value of $\Theta_{(n)}$ seems to evolve smoothly across t_{touch}.

None of the regions with positive ingoing expansion become dominant. To demonstrate this, Fig. 5.14 shows the average

$$\overline{\Theta_{(n)}} := \frac{1}{A} \int_{\mathcal{S}} \Theta_{(n)}\, dA\,. \tag{5.6}$$

It is zero for the MOTSs present in the time symmetric initial state and negative

thereafter.

5.5.2 The Horizon Signatures

The signature is one of several properties which require knowledge of the evolution of the MOTSs on a dynamical horizon. This poses new numerical challenges and our approach to computing these quantities includes several new algorithms, which will be described briefly. In the case of the signature, the definition is straight forward: Given a point $p \in \mathcal{H}$ on a dynamical horizon $\mathcal{H}$, the signature at p is defined via the determinant of the induced metric Q_{ab} on $\mathcal{H}$. If $\mathcal{H}$ is *spacelike* at p, then $\det Q > 0$ and the metric has Riemannian signature $(+++)$. $\mathcal{H}$ is *timelike* if one of the eigenvalues of Q_{ab} is negative, i.e. when its signature is $(-++)$ and hence $\det Q < 0$. In the degenerate case when $\det Q = 0$, $\mathcal{H}$ is said to have *null* signature at p. In principle, this can change from point to point, and we will see that this will become important in our case.

Numerical Computation of the Signature

Numerically, the signature is determined in the following way. We will use the fact that the signature of $\mathcal{H}$ at p can be determined by the character of any *normal* τ^μ to $\mathcal{H}$. Let $\tau_p^\mu \in T_p\mathcal{M}$ be a normal to $\mathcal{H}$ at p, then

$$\tau_p \cdot \tau_p \begin{cases} < 0 & \Leftrightarrow & \mathcal{H} \text{ spacelike} \\ > 0 & \Leftrightarrow & \mathcal{H} \text{ timelike} \\ = 0 & \Leftrightarrow & \mathcal{H} \text{ null} \end{cases} . \tag{5.7}$$

Since a normal to $\mathcal{H}$ is also normal to $\mathcal{S}$, we have $\tau_p^\mu \in T_p^\perp \mathcal{S}$, which is spanned by the null normals n^μ and ℓ^μ. This implies

$$\tau_p^\mu = c_1 \ell_p^\mu + c_2 n_p^\mu \tag{5.8}$$

for some coefficients c_1, c_2, and hence $\tau_p \cdot \tau_p = -2c_1 c_2$. Now, let U_p^μ be any tangent to $\mathcal{H}$ at p with $0 \neq U_p^\mu \notin T_p\mathcal{S}$ (to exclude the case that U_p^μ is orthogonal to ℓ^μ and n^μ). Clearly, U_p^μ and τ_p^μ are orthogonal, implying $\tau_p \cdot U_p = 0$ and thus

$$c_1 \left(\ell_p \cdot U_p \right) = -c_2 \left(n_p \cdot U_p \right) . \tag{5.9}$$

Therefore, the sign of $-2c_1 c_2$ is the same as that of

$$f_{\text{sig}} := (\ell \cdot U)(n \cdot U) . \tag{5.10}$$

Numerically, a valid tangent U_p is very efficient to compute: We simply take any parametrization along the curves representing the MOTSs $\mathcal{S}_t$ at different times, which varies smoothly along $\mathcal{H}$. An example is the invariant angle ζ introduced in Sec. 2.3. An equally valid choice is the *relative proper length parameter*

$$\tilde{\lambda}(\lambda) := \frac{l_\lambda}{l_\pi} \,, \tag{5.11}$$

where $\lambda \in [0, \pi]$ is the parameter along the curve of $\mathcal{S}_t$ used in the numerical representation, and l_λ the proper length of the curve segment starting at the north pole (where $\lambda = 0$) and ending at λ, i.e. l_π is the total proper length of the curve from the north pole of $\mathcal{S}$ to the south pole. Fixing ζ or $\tilde{\lambda}$ and varying t, we obtain a curve along $\mathcal{H}$ and take U_p to be the tangent along this curve.

One useful property of Eq. (5.10) is that f_{sig} has no poles along $\mathcal{S}$ and also varies smoothly in time. This allows us to obtain accurate interpolations of function values, yielding precise locations of the signature changes on $\mathcal{H}$.

The Evolution Vector Field

A different quantity on $\mathcal{H}$ will be very important for various physical properties. Among other uses, it yields the signature of $\mathcal{H}$ in a different way than discussed above. This quantity is the *evolution vector field* V^μ, which is tangent to $\mathcal{H}$ and orthogonal to the MOTSs $\mathcal{S}$. We fix the scaling by requiring $\mathcal{L}_V t = 1$, where $\mathcal{L}_V$ is the Lie derivative along V. Since $\mathcal{L}_V t = V^\mu \partial_\mu t = V^0$ in the simulation coordinates, this scaling is numerically trivial to achieve. To determine the signature of $\mathcal{H}$, we write V^μ using the null normals of $\mathcal{S}$:

$$V^\mu = b\ell^\mu + cn^\mu \,. \tag{5.12}$$

Since V^μ is orthogonal to $\mathcal{S}$, the signature of $\mathcal{H}$ only depends on the sign of $V \cdot V = -2bc$. When b and c have opposite signs, $\mathcal{H}$ is spacelike. When they have the same sign, $\mathcal{H}$ is timelike. $\mathcal{H}$ is null if either b or c vanish. Intuitively, this can be understood by writing the null normals ℓ^μ and n^μ in terms of the timelike normal T^μ on the slice and the spacelike normal R^μ of $\mathcal{S}$ within the slice. Doing this, using Eq. (2.8), we get

$$V^\mu = \frac{b+c}{\sqrt{2}} \, T^\mu + \frac{b-c}{\sqrt{2}} \, R^\mu \,. \tag{5.13}$$

When b and c have different signs, the R^μ term dominates and $\mathcal{H}$ is spacelike. Conversely, the T^μ term is dominant if b and c have the same sign.

Despite the simplicity in scaling, finding V^μ numerically is more expensive than computing f_{sig} via Eq. (5.10), which is why we use f_{sig} for computing the signature if none of the other advantages (to be discussed later) of V^μ are needed. We note that

the signature results determined via V^μ and f_{sig} agree within numerical limits.

Numerically, V^μ can be determined as illustrated in Fig. 5.15. First, we choose invariant coordinates (θ, φ) on each MOTS $\mathcal{S}$ constituting $\mathcal{H}$ based on the construction in Sec. 2.3. Using the simulation time coordinate t, we obtain coordinates (θ, φ, t) on $\mathcal{H}$. Fixing θ and φ yields a curve in $\mathcal{H}$, which is in general not orthogonal to the MOTSs $\mathcal{S}$. Consider now a point $p \in \mathcal{H}$ and a MOTS $\mathcal{S}_{t_0}$ containing p. We then introduce a linear t-dependence for θ and φ,

$$\theta \to \theta(t) = \theta_0 + \varepsilon_1 \, (t - t_0), \qquad \varphi \to \varphi(t) = \varphi_0 + \varepsilon_2 \, (t - t_0), \qquad (5.14)$$

where (θ_0, φ_0) are the coordinates of p in $\mathcal{S}_{t_0}$ and $\varepsilon_{1,2}$ are constants which are numerically optimized. The optimization condition is that the tangent X^μ to the generated curve be orthogonal to $\mathcal{S}_{t_0}$. In case of no angular momentum, it turns out that the numerical coordinates already fix φ such that setting $\varepsilon_2 \equiv 0$ suffices for finding V^μ. This leaves us with a one-dimensional optimization problem, which is numerically efficient to solve.

Signature Results

Let us now turn to the results computed using the above methods. As already mentioned, the signature turns out to be accurately computed with both methods. We will show the signature itself, and also describe the signs of the coefficients b and c of Eq. (5.12).

As before, the two individual horizons $\mathcal{H}_{1,2}$ are the easiest to describe: They are spacelike everywhere, as can be seen in first two panels of Fig. 5.16. In contrast to the ingoing expansion, $\mathcal{H}_{\text{outer}}$ remains uninteresting as well and is spacelike everywhere. This is shown in the right panel of Fig. 5.16. In these three cases, we have $b > 0$ and $c < 0$ everywhere.

The picture changes dramatically for $\mathcal{H}_{\text{inner}}$, for which we show the signature in Fig. 5.17. We find in total two transitions. $\mathcal{H}_{\text{inner}}$ starts out being spacelike everywhere for a very short duration. In this part, visible at the bottom of the bottom-left panel of Fig. 5.17, we have $b < 0$ and $c > 0$. Starting from the two poles, b changes sign and
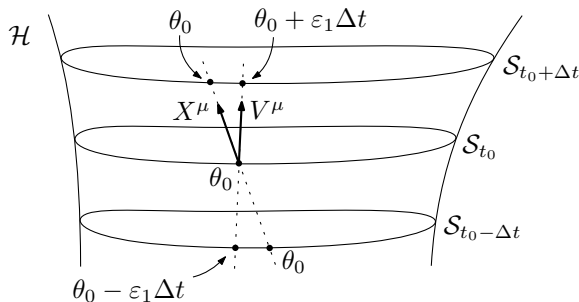
Figure 5.15: Numerical method to determine the evolution vector V^μ at a point $p \in \mathcal{H}$ with coordinates (θ_0, t_0) in $\mathcal{H}$ (the φ dependence is suppressed in this example). Keeping θ_0 fixed, we obtain a curve with tangent $X^\mu \in T_p\mathcal{H}$. Numerical minimization is used to determine ε_1 such that X^μ becomes orthogonal to $\mathcal{S}_{t_0}$, whence $X^\mu = V^\mu$.
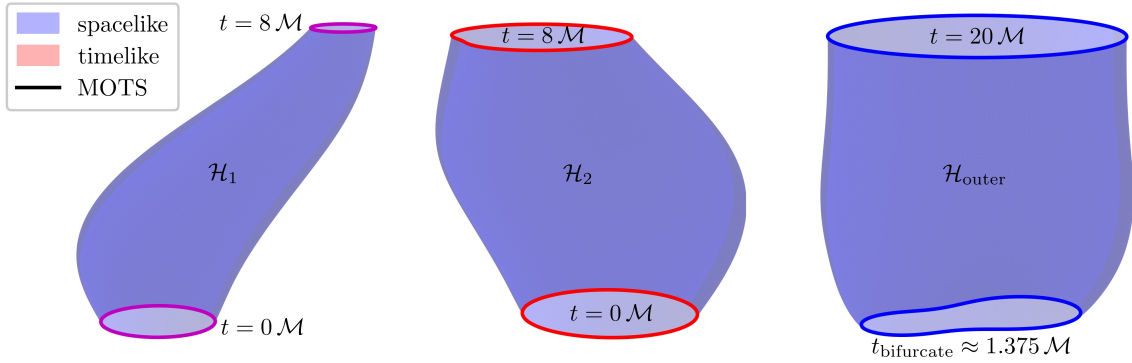
Figure 5.16: Signature of $\mathcal{H}_1$, $\mathcal{H}_2$ and $\mathcal{H}_{\text{outer}}$. All three of these horizons are purely spacelike hypersurfaces.

becomes positive. The corresponding red region of timelike signature soon stretches across the full MOTSs of $\mathcal{H}_{\text{inner}}$. At a time before (but relatively close to) t_{touch}, the region enclosing $\mathcal{S}_2$ shows a transition to spacelike signature, indicated by the blue area. Here, c changes sign and becomes negative. As will be discussed in Sec. 5.5.3, this sign change of c is crucial in understanding the behavior of the area of $\mathcal{S}_{\text{inner}}$. Of special importance is the fact that c is at no point negative on one full MOTS. In fact, the spacelike region never reaches the neck of $\mathcal{S}_{\text{inner}}$, except for potentially at one instant, namely t_{touch}. This latter fact is shown in Fig. 5.18, where we show the proper length of the curve segment connecting the neck with the point of signature change.

5.5.3 The Area Increase Law and the Area Anomaly

The general behavior of the area was already presented in Fig. 5.10 in Sec. 5.4. There, we briefly mentioned that even along the connected path $I \rightarrow II \rightarrow III$, the area is not monotonically increasing. The precise location where monotonicity fails is along segment II, just before t_{touch}. A close-up of this part is shown in Fig. 5.19, where we see that the area change turns from decreasing to increasing at $t_{\text{min}} \approx 5.5059\,\mathcal{M} < t_{\text{touch}}$. We shall call the difference between the area at the MOTS merger and the minimum the *area increase* ΔA. If the anomalous area increase ΔA vanishes, the area increases monotonically along $I \rightarrow II \rightarrow III$.

The fact that ΔA is greater than zero for a particular valid initial configuration is enough to show that monotonicity cannot be expected to hold in all cases. However, it is still of interest whether astrophysically relevant configurations also show such a feature. Keeping axisymmetry, a clearly non-generic property, we can still vary the parameters of the initial condition and determine the effect on ΔA. Fig. 5.20 contains the numerically computed values of ΔA when varying the initial separation and the mass ratio. Keeping a fixed mass ratio, we find that the area increase generally shrinks
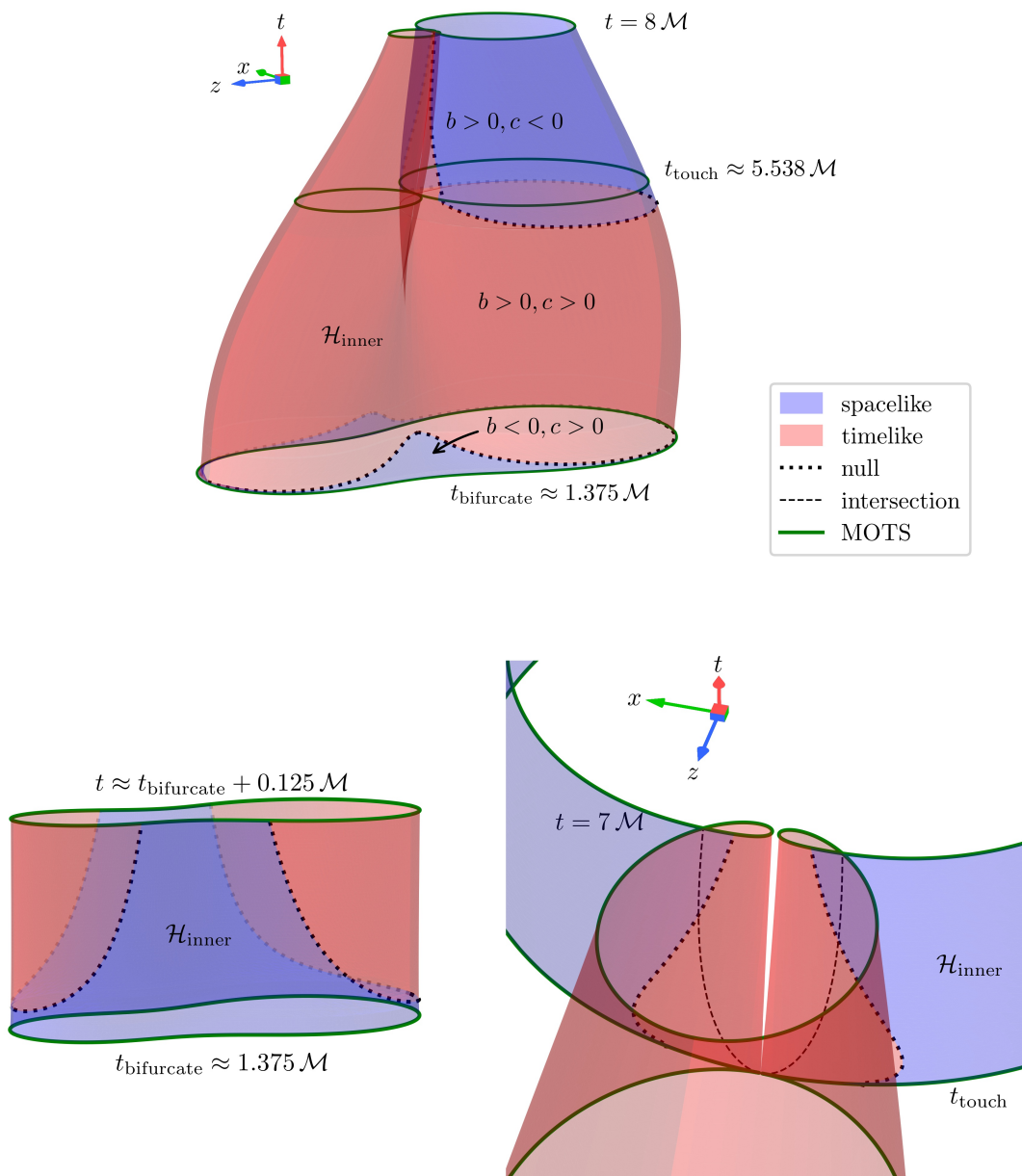
Figure 5.17: Signature of $\mathcal{H}_{\text{inner}}$. Blue regions are spacelike, red regions are timelike, and the thick dotted line indicates the transition where the signature is null. The top panel contains an overview and includes the signs of the coefficients b and c of Eq. (5.12). A close-up in the bottom-left shows that $\mathcal{H}_{\text{inner}}$ is initially spacelike on full sections and quickly develops timelike portions around the poles. The bottom-right panel shows a close-up of the part after t_{touch} and contains an indication of the double points where $\mathcal{S}_{\text{inner}}$ self-intersects (thin dashed line). The coordinate axes are included so that the perspective is easier to make out. (Parts of this figure adapted from [80].)

Figure 5.18: Proper length Δl of the curve that connects the point of signature change on $\mathcal{S}_{\text{inner}}$ (dotted line in Fig. 5.17) with the neck for times close to and after t_{touch}. It is numerically difficult to confirm whether the signature change happens at the neck in the limit $t \to t_{\text{touch}}$. (Figure adapted from [80].)
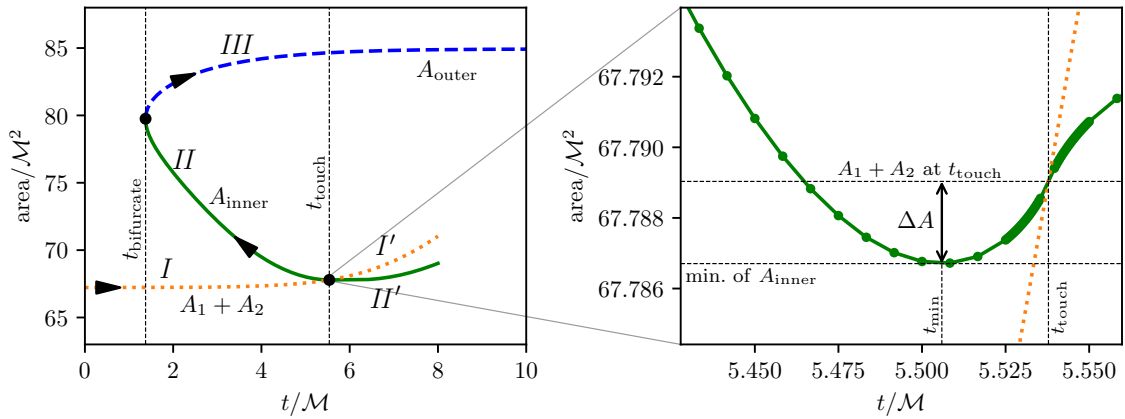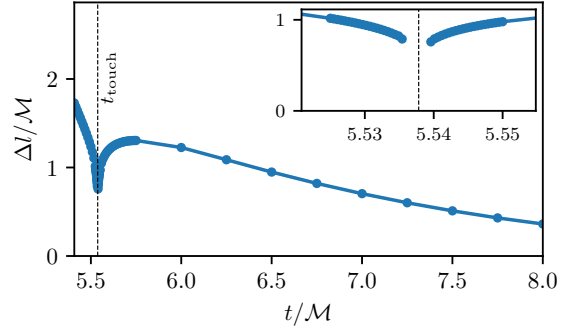
Figure 5.19: Details of the area anomaly of $\mathcal{S}_{\text{inner}}$. The left panel shows the overview of the left panel of Fig. 5.10 and the right panel a close-up of the times near t_{touch}. The dotted orange line shows the area sum $A_1 + A_2$ and the green dots are the data points at which we have found the MOTS and computed the area. The area increase ΔA is defined as the difference between the minimal area at t_{min} and the value of $A_1 + A_2$ at t_{touch}. (Figure adapted from [83].)

as the initial separation is increased. We also see an increase of ΔA for more unequal masses. The shaded region in Fig. 5.20 shows the parameter space in which the initial data already contain a common horizon. Note that our initial data consist of a time symmetric slice; the black holes are initially "at rest". Since merging astrophysical black holes will unlikely assume a configuration of being at rest while in close proximity, one should expect larger initial separations $\tilde{d}_0$ to be more natural, and thus ΔA to become insignificant.

Despite this observation, the mathematical question of how this result is consistent with the various area increase laws remains. The most important result for our case is the proof of Bousso & Engelhardt [30, 31]. Consistency with our result is easily found, since $\mathcal{H}_{\text{inner}}$ does not satisfy the necessary conditions required for the proof to hold, i. e. it is not a *regular holographic screen*. In fact, it is not even a holographic screen, which
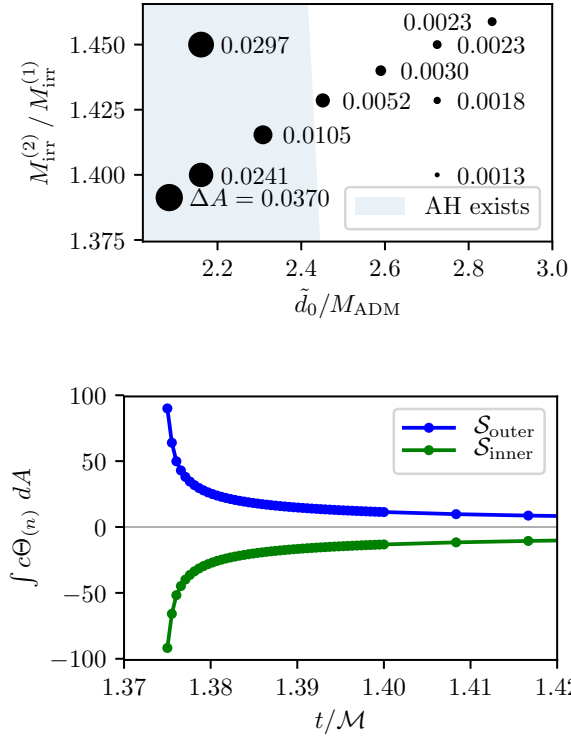
Figure 5.20: Values of the area increase ΔA for various initial data. We vary both, the initial distance and the mass ratio and compute the proper initial distance $\tilde{d}_0$ of the horizons along the z axis as well as the ratio of the irreducible masses $M_{\mathrm{irr}}^{(1)}$ and $M_{\mathrm{irr}}^{(2)}$. The shaded region is the part of parameter space where the common horizons are already present in the initial data. (Figure taken from [83].)
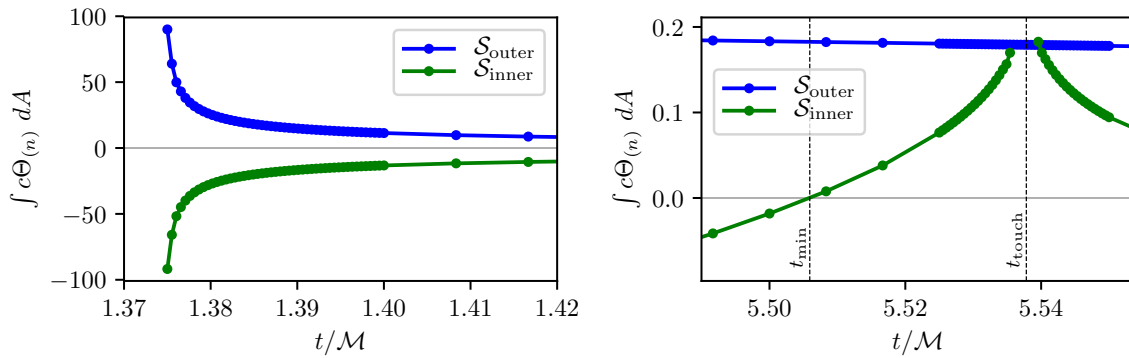
Figure 5.21: Integral of $c\Theta_{(n)}$ for $\mathcal{S}_{\mathrm{outer}}$ and $\mathcal{S}_{\mathrm{inner}}$ as functions of time, where c is defined via Eq. (5.12). The left panel shows the results close to where the common horizons form and rapidly increase ($\mathcal{S}_{\mathrm{outer}}$) or decrease ($\mathcal{S}_{\mathrm{inner}}$) in area. The right panel shows the times t_{min} of minimal area and t_{touch} where $\mathcal{S}_{\mathrm{inner}}$ merges with $\mathcal{S}_{1,2}$. A comparison with Fig. 5.19 shows that it is consistent with the integrals plotted here being the time derivative of the area. (Figure adapted from [80].)

in the terminology used here is called a future dynamical horizon with no condition on the signature. This is because the future condition is violated by the portions of $\mathcal{H}_{\mathrm{inner}}$ having $\Theta_{(n)} \geq 0$. At this point, it is already clear that no inconsistencies are present. However, especially in light of the discussion of the Penrose inequality in Sec. 2.5, it is useful to precisely point out which of the remaining conditions are not satisfied either.

The first step is the following observation. The rate of change of the area A with respect to our time coordinate t can be written as the Lie derivative of A along the evolution vector field V^{μ}:

$$\dot{A} = \mathcal{L}_V A = \mathcal{L}_V \int_{\mathcal{S}} dA = \int_{\mathcal{S}} c\Theta_{(n)} \, dA \,. \tag{5.15}$$

Fig. 5.21 shows the numerically computed values of Eq. (5.15) for $\mathcal{H}_{\mathrm{outer}}$ and $\mathcal{H}_{\mathrm{inner}}$. We have seen that, apart from a very small region near the formation of the common horizons, $\mathcal{H}_{\mathrm{outer}}$, $\mathcal{H}_1$ and $\mathcal{H}_2$ all have $\Theta_{(n)} < 0$ and $c < 0$, so that the area must increase.

For $\mathcal{H}_{\text{inner}}$, we initially have $c > 0$. The ingoing expansion $\Theta_{(n)}$ does have a region near the neck where it is positive. However, this is too small and the values not large enough to become important, whence the area initially decreases. However, it is the sign change of c from positive to negative values which results in a growing region having a positive integrand in Eq. (5.15). The left panel of Fig. 5.21 shows the times close to the formation of the common horizons and the right panel the behavior near t_{touch}. The interpolated curve for $\mathcal{H}_{\text{inner}}$ crosses zero within a time about $10^{-5}\,\mathcal{M}$ from t_{min}. Since the computation of both c and $\Theta_{(n)}$ is fully independent of the area, this also presents another verification for the area increase not being a numerical artifact.

Summarizing the behavior of $\mathcal{H}_{\text{inner}}$ relevant for the proof in [30, 31], we have the following properties:

1. $c > 0$ on a portion covering most of $\mathcal{H}_{\text{inner}}$, with the exception of a portion appearing *before* t_{touch}, where $c < 0$.

2. The portion with $c < 0$ never contains a full MOTS for as long as we can track $\mathcal{H}_{\text{inner}}$. On this portion, $\mathcal{H}_{\text{inner}}$ is spacelike.

3. After t_{touch}, the leaves $\mathcal{S}_{\text{inner}}$ of $\mathcal{H}_{\text{inner}}$ self-intersect, i.e. they do *not* split the Cauchy slices Σ into just two disjoint portions.

Regularity in the sense of Definition II.8 in [31] requires, in addition to certain genericity conditions satisfied in our case, that (i) every inextendible portion of definite sign of c is entirely timelike or contains at least one full MOTS and (ii) every MOTS of the horizon splits a Cauchy slice Σ into two disjoint portions.

Property 2 in the above list violates (i) and property 3 violates (ii).

5.6 Stability Analysis

The analysis of the stability operator in the time symmetric case in Chapter 4 proved to be a key ingredient in assessing the existence of the MOTSs and thus show the capabilities of the new MOTS finding algorithm. In anticipation of the dynamical case, where MOTSs did vanish in earlier analyses (see e.g. [46]), this application of the stability spectrum was supposed to aid in arguing *why* the MOTSs vanished. In fact, it turned out that in the simulations we analyzed thus far, no such sudden vanishing of MOTSs could be observed. The instances of our finder failing to locate a MOTS present in a neighboring time slice can, in each case, be ascribed to one of two reasons: i) lack of accuracy of the numerical slice data ii) distortions approaching a non-smooth state. The first can be alleviated by increasing the numerical resolution. This was necessary to, e.g., locate $\mathcal{S}_{1,2}$ at times up to $t = 8\,\mathcal{M}$ in the simulation setup discussed in the previous sections. The second is a consequence of our numerical representation

of the MOTSs (cf. Sec. 3.1), which leads to the resolution diverging when a non-smooth feature like the cusp of $\mathcal{S}_{\text{inner}}$ forms at t_{touch}.

Both of these instances are consistent with no eigenvalue of the stability operator approaching zero, which we will discuss below. However, the application of the spectrum is potentially wider than predicting existence. After focusing on the lower eigenvalues and existence in Sec. 5.6.1, section 5.6.2 will present a much larger part of the spectrum than shown in the time symmetric case.

5.6.1 Existence and the low Eigenvalues

Building on the results obtained for the time symmetric case in Sec. 4.3.1, we expect the individual MOTSs $\mathcal{S}_{1,2}$ and the apparent horizon $\mathcal{S}_{\text{outer}}$ to be stable, i.e. the principal eigenvalues Λ_0 of L_Σ should be positive as long as these MOTSs are found. Fig. 5.22 shows the principal eigenvalue of L_Σ for all four horizons in the two left panels. For comparison, the right panels show the principal eigenvalue of $L^{(-n)}$. The two bottom panels of Fig. 5.22 show the absolute value of Λ_0 on a logarithmic scale in order to capture their behavior for $\mathcal{S}_{\text{inner}}$.

As long as we can track them, $\mathcal{S}_{1,2}$ always have $\Lambda_0 > 0$, with $\mathcal{S}_1$ having the larger of the two values. This is consistent with Eq. (2.29) since $\mathcal{S}_1$ has the smaller area (and hence areal radius R). For $\mathcal{S}_{\text{outer}}$ and $\mathcal{S}_{\text{inner}}$ the initial behavior is very similar to the time symmetric case when decreasing the distance d: They are both born with vanishing principal eigenvalue. Λ_0 then increases to positive values for $\mathcal{S}_{\text{outer}}$ and decreases to large negative values for $\mathcal{S}_{\text{inner}}$. In contrast to the time symmetric case, $\mathcal{S}_{\text{inner}}$ forms a cusp and then self-intersects. As a result, the evolution of the principal eigenvalue is very different. At the moment the cusp forms at t_{touch}, Λ_0 seems to diverge to $-\infty$. After this time, it falls to negative values of much smaller magnitude, with no indication of eventually becoming 0.

The principal eigenvalue of the stability operator $L^{(-n)}$ differs from that of L_Σ in that it is generally larger. Interestingly, there is a short time interval after formation where $\mathcal{S}_{\text{inner}}$ has *positive* principal eigenvalue $\Lambda_0^{(-n)} > 0$. This eigenvalue then becomes zero at some time $t < 2\,\mathcal{M}$, which demonstrates that for the existence analysis, L_Σ should be considered.

Since the principal eigenvalue of L_Σ for $\mathcal{S}_{\text{inner}}$ is negative, we need to consider the higher eigenvalues to analyse existence. First, it is clear that during the smooth evolution of $\mathcal{S}_{\text{inner}}$ from the point it is born up to t_{touch}, all higher eigenvalues must be positive. This is due to $\Lambda_0 = 0$ initially, combined with the fact that it is the smallest eigenvalue and can be shown to be non-degenerate [7, 8]. Consequently, all higher eigenvalues are greater than zero and should remain so for as long as $\mathcal{S}_{\text{inner}}$ evolves smoothly. This expectation is indeed met, which is shown in Fig. 5.23 where $\Lambda_{1,0}$ is
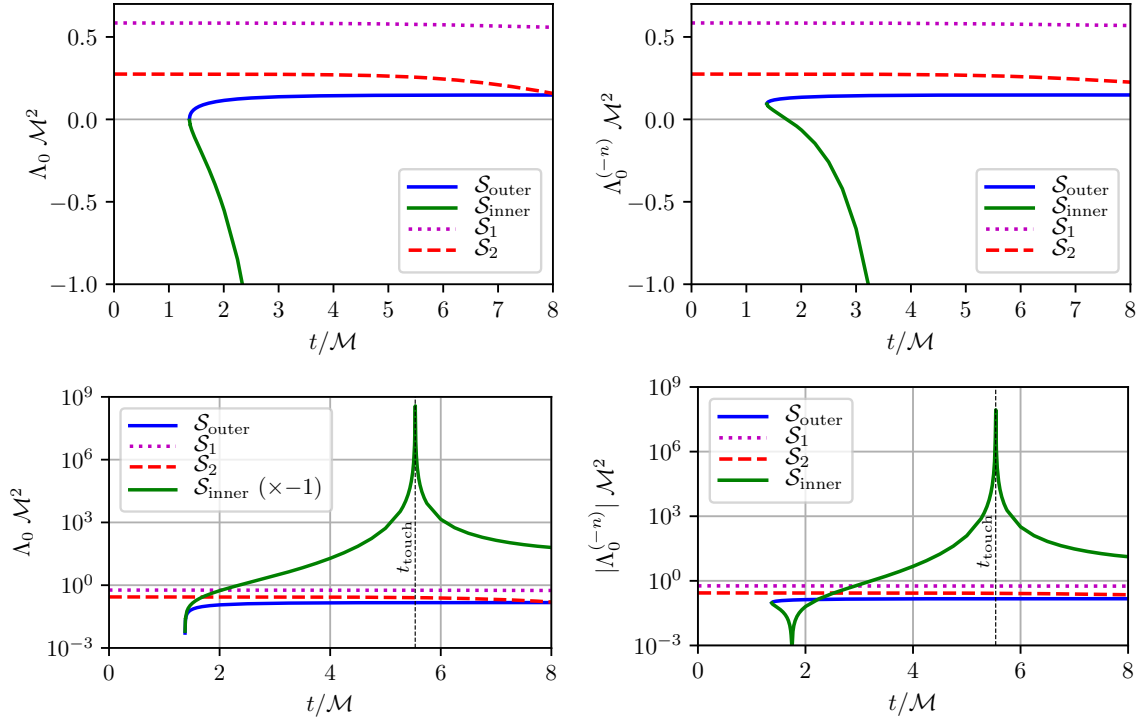
Figure 5.22: Principal eigenvalue Λ_0 of the stability operators L_Σ (left) and $L^{(-n)}$ (right) as function of time. The top two panels clearly show the bifurcation of $\mathcal{S}_{\text{outer}}$ and $\mathcal{S}_{\text{inner}}$ while the bottom two panels present the numerical indication that Λ_0 diverges to $-\infty$ for $\mathcal{S}_{\text{inner}}$ at t_{touch}. Note that $\Lambda_0^{(-n)}$ has a root for $\mathcal{S}_{\text{inner}}$ in the upper-right panel which is also visible in the lower-right panel. (Parts of this figure adapted from [81].)
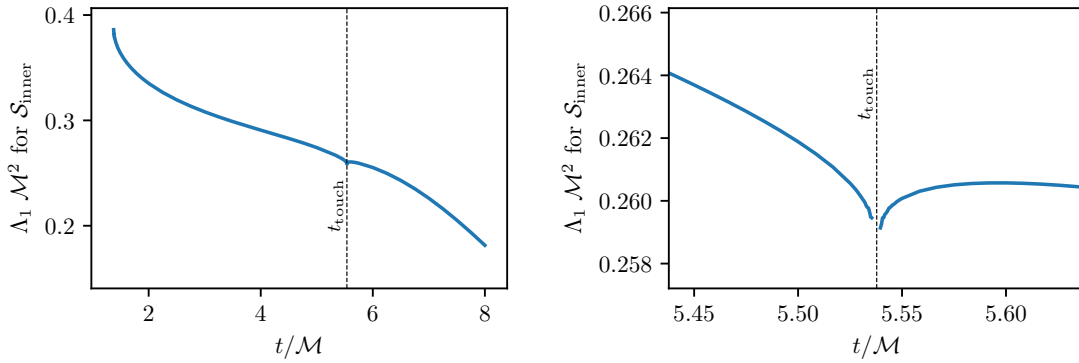
Figure 5.23: Eigenvalue $\Lambda_1 := \Lambda_{1,0}$ of $\mathcal{S}_{\text{inner}}$ for angular mode $m = 0$. Before t_{touch}, this is the second lowest eigenvalue of L_Σ and can hence be seen as "stability parameter". The left panel shows the full behavior and the right panel a close-up near t_{touch}. The curve seems to form a cusp at t_{touch} but we cannot numerically resolve how far further down it drops. Since it is not zero here, $\mathcal{S}_{\text{inner}}$ is guaranteed to exist even closer to t_{touch} (Figure adapted from [81].)
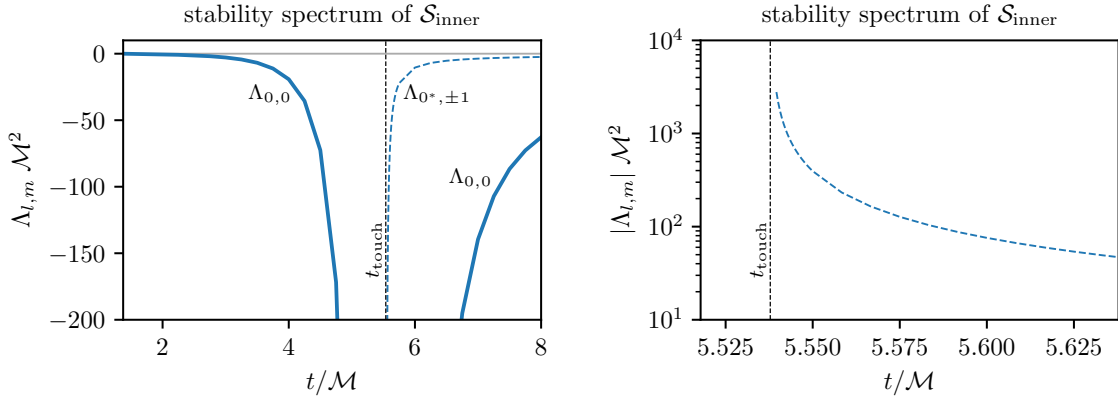
Figure 5.24: The negative eigenvalues of L_Σ for $\mathcal{S}_{\text{inner}}$ as function of time. Before t_{touch}, the principal eigenvalue $\Lambda_0 := \Lambda_{0,0}$ is the only negative eigenvalue. After t_{touch}, a new pair of degenerate eigenvalues $\Lambda_{0^*,\pm 1}$ appears. The left panel shows an overview and the right panel the magnitude of $\Lambda_{0^*,\pm 1}$. (Figure adapted from [81].)

plotted.[3] Note that in the left panel, there is no visible indication of this eigenvalue vanishing at t_{touch}. However, very close to t_{touch}, a cusp seems to form in this curve, as can be seen in the close-up in the right panel. Based on these results, it is not possible to exclude the case that $\Lambda_{1,0}$ becomes zero for one instant in time at t_{touch}.

The proposed merger scenario could be excluded if $\Lambda_{1,0}$ vanishes at a time *before* t_{touch}. This could happen if $\Lambda_{1,0} \to -\infty$ for $t \to t_{\text{touch}}$. Numerically, such a case cannot be completely ruled out, though the results presented here also do not point towards this possibility.

Interestingly, two new (degenerate) negative eigenvalues appear after t_{touch}. Since these are *added* to the spectrum, we chose to deviate from the labeling scheme discussed in Sec. 2.4 and instead assign these values the label $\Lambda_{0^*,\pm 1}$. These values are shown in Fig. 5.24 as dashed blue curve. The close-up on logarithmic scale in the right panel suggests that these eigenvalues might also diverge to $-\infty$ at t_{touch}, though this is far less clear than for Λ_0. No such new negative eigenvalues appear for $L^{(-n)}$. Their appearance for L_Σ is hence caused by the shear term $-2|\sigma|^2$ by which the two operators differ (cf. their definitions (2.26) and (2.27)). Fig. 5.25 shows that indeed this term also seems to diverge at t_{touch}.

Turning again to $\mathcal{H}_{\text{outer}}$, we have already mentioned that at late times, the apparent horizon approaches its equilibrium state, for which Eq. (2.29) tells us that $\Lambda_0 \to 1/4M_{\text{irr}}^2$. We can thus ask how Λ_0 approaches this asymptotic value during the evolution. Seeing that $\Lambda_0 \times 4M_{\text{irr}}^2 \to 1$, Fig. 5.26 shows the difference of this value to 1. After an initially fast, almost exponential decay, a phase of slower decay follows, with the transition

---

[3]The shown eigenvalue is the next higher one for an angular mode $m = 0$. Before t_{touch}, it is indeed the lowest eigenvalue $> \Lambda_0$. This changes after t_{touch} and is discussed below.

Figure 5.25: Maximum of of $|\sigma|^2$ along $\mathcal{S}_{\mathrm{inner}}$ as function of time.
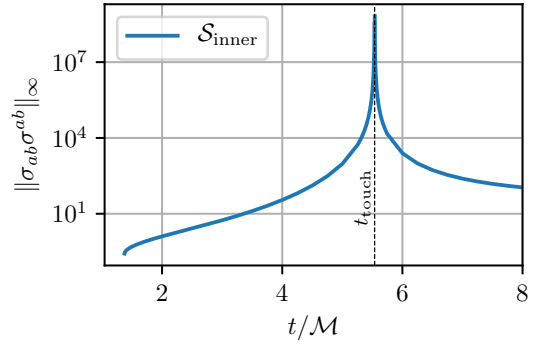
Figure 5.26: Approach of the principal eigenvalue Λ_0 of L_Σ to its asymptotic value $1/4M_{\mathrm{irr}}^2$. After an initially steep decay, an oscillating shallower decay can be observed. (Figure adapted from [81].)
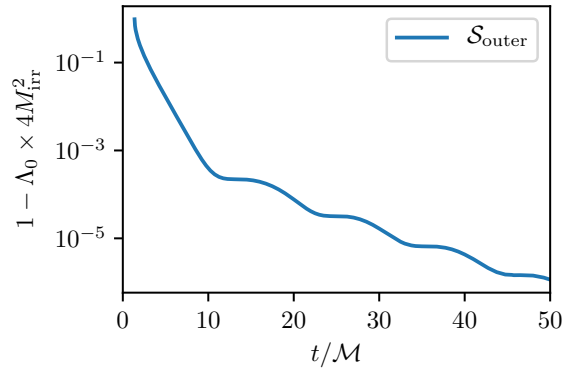
happening approximately at $10\,\mathcal{M}$. In contrast to the first phase, the shallower decay exhibits an oscillating behavior. This general behavior will occur again in Sec. 5.7, where we analyze the approach of $\mathcal{H}_{\mathrm{outer}}$ to the final state.

5.6.2 Global behavior

After discussing the stability and existence of the horizons based on the lowest eigenvalues of L_Σ, we will now focus on the higher eigenvalues, the structures they form, and their possible interpretations. For the horizons that either begin or end in a nearly spherical state, namely $\mathcal{H}_{1,2}$ and $\mathcal{H}_{\mathrm{outer}}$, one would expect the spectrum to reflect this behavior. Fig. 5.27 shows that this is indeed the case. The top two panels show the spectrum for the two individual horizons and the bottom two panels for $\mathcal{H}_{\mathrm{outer}}$ and $\mathcal{H}_{\mathrm{inner}}$, respectively.

For $\mathcal{H}_{1,2}$, we initially find the eigenvalues to be relatively close to the prediction of Eq. (2.29). The eigenvalues clearly form what might be called a multiplet structure, where the $(2l + 1)$ fold degeneracy of the l'th multiplet is broken as the evolution progresses and the horizons start to interact. Due to the axisymmetry and absence of
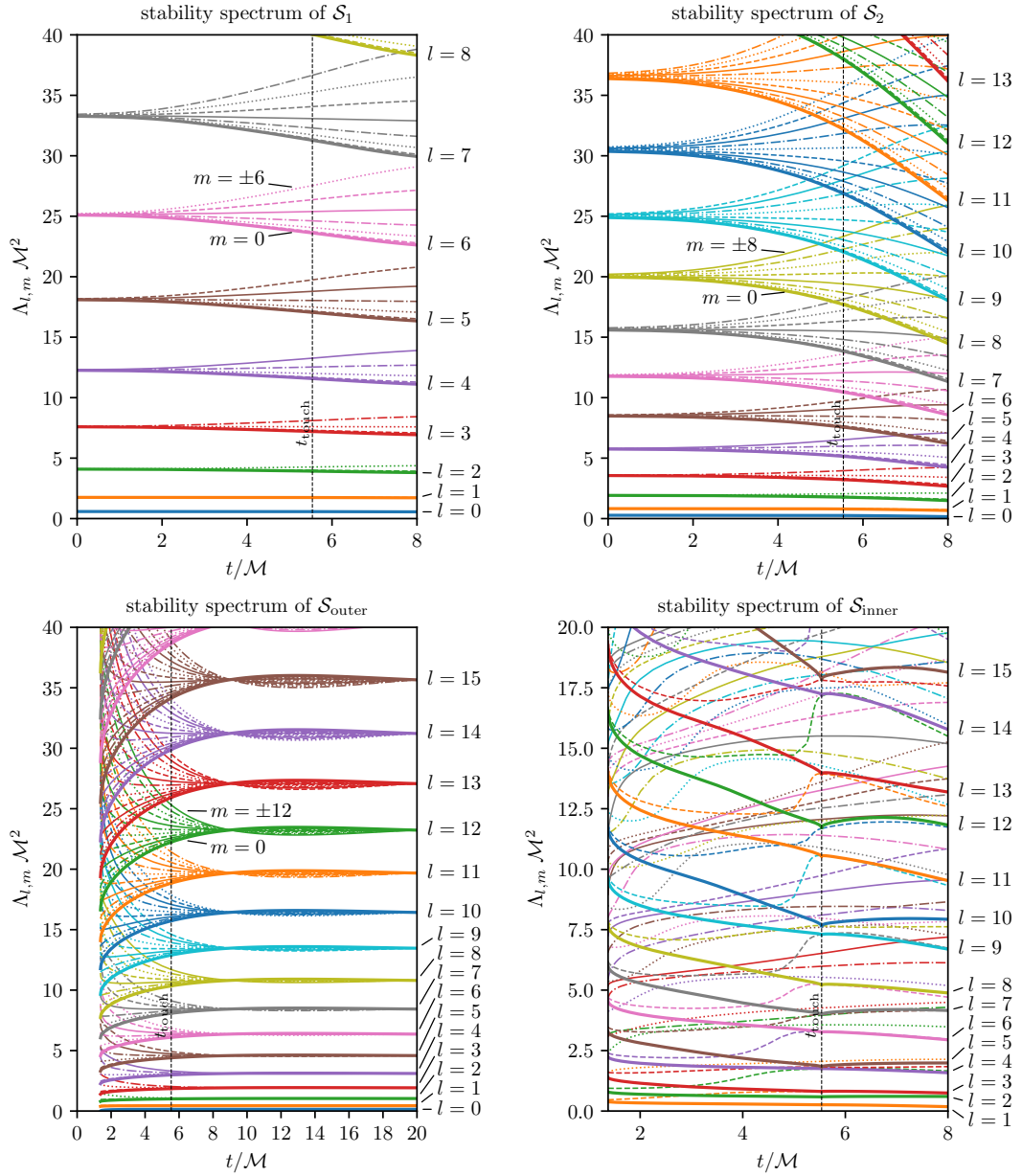
Figure 5.27: Higher eigenvalues of the stability operator L_Σ for all four horizons as function of time. The values $\Lambda_{l,m}$ of equal l and different m are given the same color to visualize the multiplet structures for $\mathcal{H}_{1,2}$ and $\mathcal{H}_{\text{outer}}$. For the individual horizons, the spectrum is initially well described by Eq. (2.29) and becomes more complicated as they interact during the merger. The opposite happens for $\mathcal{H}_{\text{outer}}$, which approaches such an equilibrium state at later times. For $\mathcal{H}_{\text{inner}}$, the positive eigenvalues exhibit a much more complicated structure. (Figure adapted from [81].)

any angular momentum in the problem, the $\pm m$ degeneracy is not broken and remains throughout the whole merger. In the fully generic situation of inspiralling black holes, the $\pm m$ degeneracy will not be present. Note that the different levels cross during the evolution. Visually, the differentiation between the levels becomes more difficult. However, due to the axisymmetry which causes the eigenvalue problem of the stability operator to separate, we can always numerically control the angular mode m, see also Sec. 2.4. Fixing this "quantum number", the spectrum for fixed m is sorted in ascending order. For these sorted eigenvalues, we assign increasing values of l starting with $l = |m|, |m| + 1, |m| + 2, \dots$ (with the exception of $\Lambda_{0*,\pm 1}$ mentioned in Sec. 5.6.1, where we start with $l = 0$ to account for the additional values).

The spectrum of $\mathcal{H}_{\text{outer}}$ (bottom-left panel of Fig. 5.27) behaves very similar to that of $\mathcal{H}_{1,2}$, with the main difference being that $\mathcal{H}_{\text{outer}}$ starts highly distorted and then relaxes to a spherical state. It is noteworthy that a new feature occurs here not present for $\mathcal{H}_{1,2}$: In the relaxation phase, there are repeated instances of the multiplets being nearly fully degenerate. The figure shows such instances close to $t = 9\,\mathcal{M}$ and $t = 20\,\mathcal{M}$. As we shall see in the next section, these are the times where the dominant multipole mode crosses zero, i.e. a state that is highly spherical.

In Fig. 5.27, the bottom-right panel shows the stability spectrum of $\mathcal{H}_{\text{inner}}$, which seems far more complex and with a much less clear indication for a multiplet structure. However, one apparent behavior is easy to see: The $|m| = 1$ angular modes all seem to "migrate" two levels from $l \to l + 2$, with the transition being completed at time t_{touch}. Geometrically, $\mathcal{S}_{\text{inner}}$ pinches off at this time and consists of two nearly spherical parts. As t_{touch} is approached, the gradual transition to this state of two round parts leads to the eigenfunctions of L_Σ to be concentrated on one or the other of these halves. This is demonstrated in Fig. 5.28, which shows two different eigenfunctions of L_Σ for $\mathcal{S}_{\text{inner}}$ at a time before t_{touch}.

Clearly, the stability spectrum of $\mathcal{S}_{\text{inner}}$ holds more information to explore than these first observations have provided. Furthermore, once we leave axisymmetric configurations, or even just consider spinning black holes still in axisymmetry, there will be even more complexity as the spectra cease to be purely real. Gaining more insight could then be accomplished using statistical methods. In what follows, we will apply one possible statistical analysis tool which focuses on the short-range interaction of the levels, i.e. their attraction and repulsion. This is only the first step into a systematic analysis, and it will not yield a clear understanding of what distinguishes the dynamics of $\mathcal{H}_{\text{inner}}$ from the other horizons. However, it will establish the foundations upon which further analyses of larger scale level interactions, such as the number variance $\Sigma(L)$ and spectral rigidity $\Delta(L)$, can be built (see e.g. [99]).

The terminology and methods used here apply in the context of the Hamiltonian of a quantum particle, in particular the study of quantum chaos [23, 24, 65, 99], and by interpreting the stability operator L_Σ as quantum Hamiltonian $\hat{H}$ (cf. sec 4.4 in [59]),

$\mathcal{S}_{\text{inner}}$ at $t = 5.35\,\mathcal{M}$
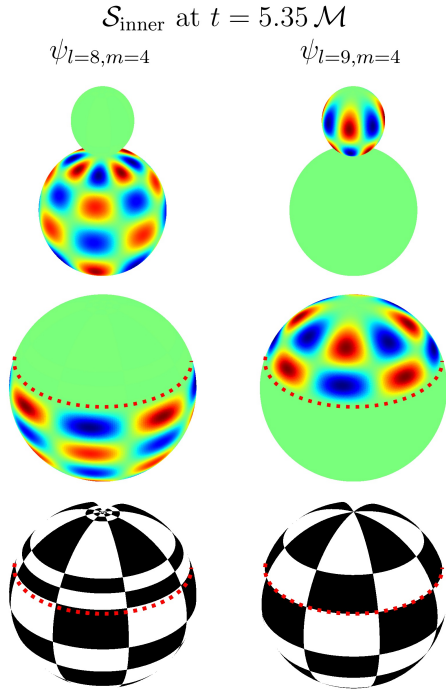
$\psi_{l=8,m=4}$ $\qquad\qquad$ $\psi_{l=9,m=4}$

Figure 5.28: Visualization of two eigenfunctions $\psi_{l=8,m=4}$ (left) and $\psi_{l=9,m=4}$ (right) of the stability operator L_Σ. The top two panels indicate the function values on the MOTS represented in the x, y, z coordinate space. Blue regions belong to negative and red regions to positive values. The two panels in the middle show the same information on a round sphere, where the location of the neck is drawn as dotted line. The bottom panels show the signs of the eigenfunctions and demonstrate that even in the regions of nearly constant green color there is still structure. It also clearly shows crossing of the nodal lines. (Figure adapted from [81].)

we will be able to benefit from the methods developed in that context.

One immediate insight comes from the fact that the eigenvalues—the "energy levels"—do cross during evolution for all horizons. This is a non-generic feature for a one-parameter (i.e. time) family of real self-adjoint operators. If the corresponding classical system is integrable, the levels are independent and can cross. Since our axisymmetric configuration leads to a *separable* problem, which implies integrability, these level crossings are not a surprising feature. Furthermore, the crossing of nodal lines visible in Fig. 5.28 is also a consequence of separability [23].

Apart from their crossing, we will now aim for an understanding of the interaction of adjacent levels, which we gain from the *nearest neighbor spacing* distribution $P(s)$. This distribution is constructed from a suitably normalized spectrum, where the average level distance $\langle s \rangle$ is set to 1, and visualizes the relative abundances of different adjacent level distances. If trivial degeneracies are present, a distance of $s = 0$ will dominate in this analysis and hide the remaining structure. We will therefore remove the one degeneracy due to our symmetry, i.e. the $\pm m$ degeneracy, when constructing $P(s)$.

In the context of quantum chaology, the generally occurring classical systems are discussed in [65] and it was found that the distribution $P(s)$ generically falls into one of a very few universal classes. For classically integrable systems, the levels are distributed like random numbers, resulting in the Poissonian distribution

$$P(s) = e^{-s}\,. \tag{5.16}$$

No level repulsion happens here, as, in fact, small distances are preferred over large ones. On the other hand, time-reversal symmetric but otherwise chaotic classical systems have the spectrum of a (large) random real symmetric matrix, yielding

$$P(s) = \frac{\pi}{2} s e^{-\pi s^2/4} \,. \tag{5.17}$$

Here the levels repel and consequently $P(s)$ vanishes for $s \to 0$. The matrices having these kinds of spectra form the *Gaussian Orthogonal Ensemble* (GOE) considered in random matrix theory.

In our case, we already discussed that we have level crossings with no sign of repulsion. This justifies the expectation that we should not find a distribution like Eq. (5.17). Before presenting numerical results of our simulations, we will address the construction of $P(s)$.

To this end, consider the eigenvalues of L_Σ,

$$\Lambda_0 < \Lambda_1 \le \Lambda_2 \le \dots \,, \tag{5.18}$$

where the trivial $\pm m$ degeneracy has been removed and we have labeled the eigenvalues in increasing order, ignoring any possible assignment of "mode numbers" (l, m). Let $N(\Lambda)$ be the level counting function defined by

$$N(\Lambda) := \sum_{n=0}^{\infty} H(\Lambda - \Lambda_n) \,, \tag{5.19}$$

where $H(x)$ is the Heaviside step function. We decompose $N(\Lambda)$ into a smooth monotonically increasing *average* $N_{\mathrm{av}}(\Lambda)$ and a fluctuating part $N_{\mathrm{fl}}(\Lambda)$, such that

$$N(\Lambda) = N_{\mathrm{av}}(\Lambda) + N_{\mathrm{fl}}(\Lambda) \,. \tag{5.20}$$

The "unfolding" is done by a change of variable $x = N_{\mathrm{av}}(\Lambda)$ and defining

$$x_n := N_{\mathrm{av}}(\Lambda_n) \,. \tag{5.21}$$

The averaged spectrum $\{x_n\}$ has the property that the average level distance, or equivalently the average level density, is unity:

$$\rho_{\mathrm{av}}(x) = \frac{dN_{\mathrm{av}}}{dx} = \frac{dN_{\mathrm{av}}}{d\Lambda} \frac{d\Lambda}{dx} = 1 \,, \tag{5.22}$$

since $d\Lambda/dx = dN_{\mathrm{av}}^{-1}/dx = (dx/dN_{\mathrm{av}}^{-1})^{-1} = (dN_{\mathrm{av}}/d\Lambda)^{-1}$. The nearest-neighbor spacing is then defined as

$$s_n = x_{n+1} - x_n \tag{5.23}$$
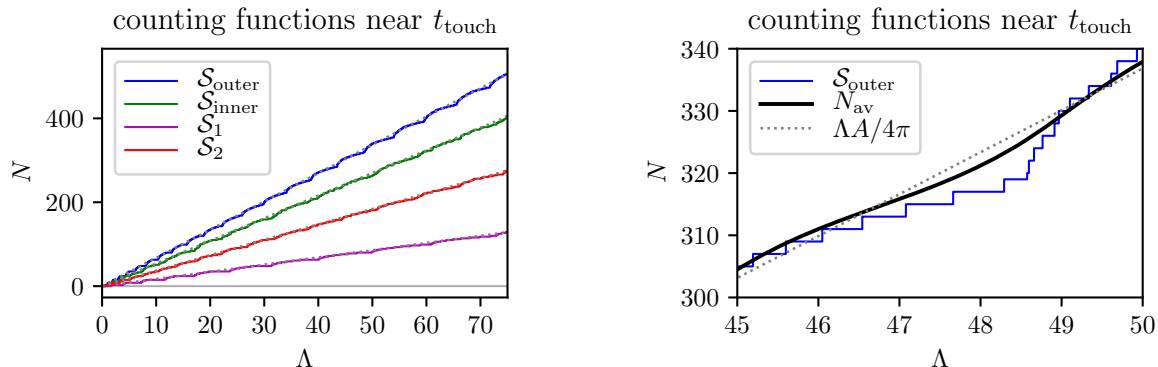
Figure 5.29: Counting function N and its average N_{av} at time $t \approx 5.5354\,\mathcal{M}$. The left panel shows an overview for all four MOTSs and the right panel a close-up where the average N_{av} can be seen. The dotted lines drawn in both panels show that we find agreement with Weyl's law presented in Appendix A of [81]. (Figure adapted from [81].)

from which we get the distribution $P(s)$, i.e. we let $P(s)\,ds$ be the probability of finding a spacing s between s and $s + ds$.

As an example, Fig. 5.29 shows in the left panel the level counting function $N(\Lambda)$ for all four horizons at time $t \approx 5.5354\,\mathcal{M}$ very close to $t_{touch} \approx 5.5378176\,\mathcal{M}$. The right panel shows a close-up for $\mathcal{S}_{outer}$ containing the average $N_{av}(\Lambda)$. Fig. 5.30 summarizes the results for our simulation, which generally satisfy the expectations. In panels (a) and (c), we plot $P(s)$ at this same time for $\mathcal{S}_{inner}$ and $\mathcal{S}_{outer}$, respectively. Despite the significantly different states these two MOTSs are in, their short-range level statistics are well described by the Poisson-like distribution corresponding to the integrability of the system.

We find a clear indication of level repulsion when picking out the eigenvalues for a fixed m. This is shown in panel (b) of Fig. 5.30, where we see a peak at $s = 1$, indicating a "picket fence" structure of the distribution of eigenvalues. An example of non-generic behavior is shown in panel (d). For this distribution we take a time $t = 9\,\mathcal{M}$, which was already mentioned at the beginning of this section as being one example of $\mathcal{S}_{outer}$ being almost spherical and the eigenvalues for different $|m|$ almost degenerate. This results in an overabundance of small level distances and hence a larger peak of $P(s)$ at $s = 0$ than expected for generic cases. This might be called a "quasi-picket-fence" structure.

(a) Poisson-like distribution for $\mathcal{S}_{\text{inner}}$.

(b) "Picket-fence" distribution for fixed m.

(c) As (a) but for $\mathcal{S}_{\text{outer}}$.

(d) "Quasi-picket-fence".
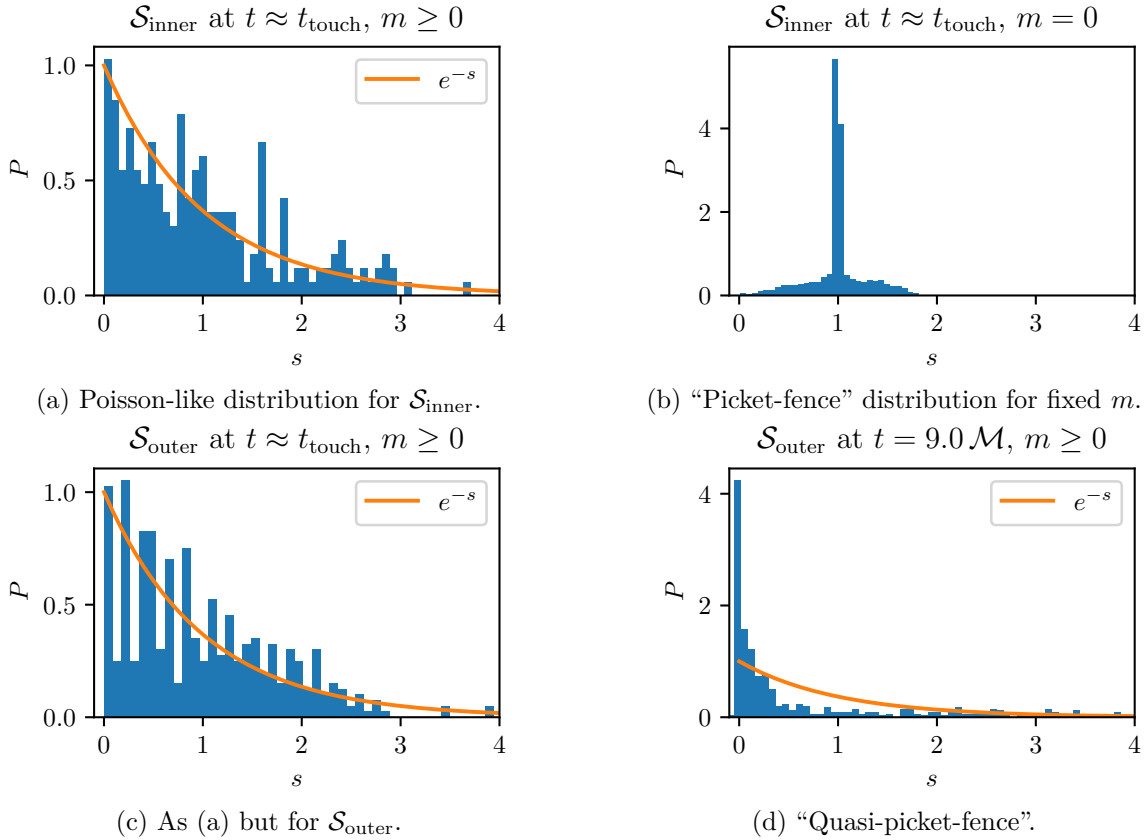
Figure 5.30: Nearest neighbor spacing distribution P for $\mathcal{S}_{\text{outer}}$ and $\mathcal{S}_{\text{inner}}$. See text for details. (Figure adapted from [81].)

5.7 The Fluxes and the Approach to the Final State

When discussing the approach to the final state, the main object of interest is the outer common horizon $\mathcal{H}_{\text{outer}}$, which, in absence of angular momentum and spin, will asymptote to a Schwarzschild horizon at late times. There are several ways to quantify this approach, the area (cf. Fig. 5.10) and the non-constant components of the intrinsic Ricci scalar being just two examples. We have also seen the approach of Λ_0 to its asymptotic value in Fig. 5.26, showing clearly two different regimes with different decay behavior. This section will first collect several observations of how this approach happens and then relates this behavior to gravitational fluxes through the horizons. The decay of both, the geometric properties encoded in the Ricci scalar as well as the dominant components of the fluxes will be shown to be closely correlated with the quasi-normal modes describing the gravitational radiation produced by the relaxation of a perturbed Schwarzschild black hole. For reference, and for comparison, many of
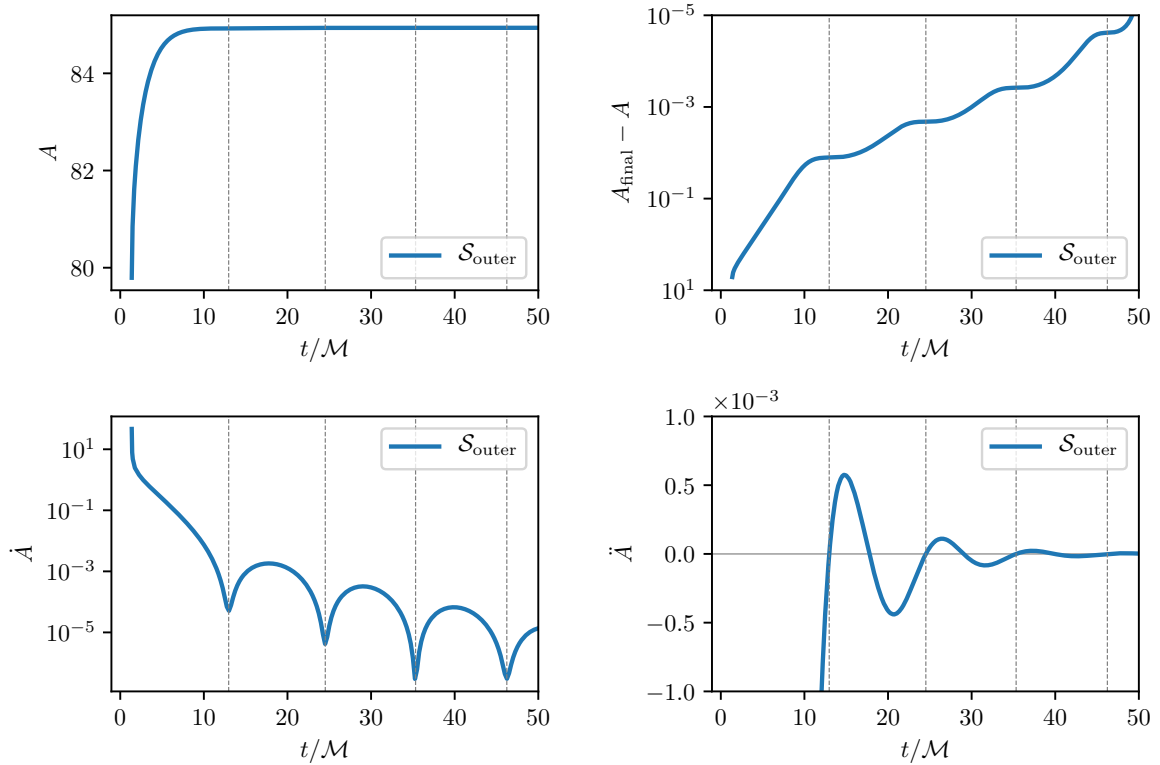
Figure 5.31: Visualizations of how the area of $\mathcal{S}_{\text{outer}}$ approaches the equilibrium state. The top-left panel shows the evolution of the area A, the initial part of which we have already seen in Fig. 5.10. The top-right panel visualizes the same data in a different way by plotting the difference to the final area on a logarithmic scale. The bottom-left panel shows the first time derivative of the area, which is strictly positive but has regular minima after the initially steep decay. The bottom-right panel contains the second time derivative, exhibiting a damped oscillation. For visual orientation, the dashed vertical lines indicate the times of the local minima of $\dot{A}$.

the results will also be presented for the other horizons $\mathcal{H}_{\text{inner}}$ and $\mathcal{H}_{1,2}$.

One of the most intuitive results describing the approach of $\mathcal{H}_{\text{outer}}$ to its asymptotic state is the evolution of the area. The top-left panel of Fig. 5.31 shows this evolution for our longest simulation of the Brill-Lindquist setup that has been the main focus thus far. After the initially fast area increase, it quickly settles at an almost constant value. A much closer look at how this settling happens is possible if the difference to its final value is plotted logarithmically. This is done in the top-right panel. A new feature not seen in the top-left panel becomes apparent: an oscillatory behavior as the final area is approached. The first and second time derivatives of the area, shown respectively in the bottom left and bottom right panel, make this even more clear. To understand this behavior, we will now show how the geometric approach to the

"round sphere" state is reflected in the oscillatory behavior of the modes of a multipolar decomposition of the Ricci scalar.

5.7.1 The Geometric Evolution: Multipole Moments

Using the invariant coordinate ζ introduced in Sec. 2.3, the decomposition of the Ricci scalar $\mathcal{R}$ of a MOTS $\mathcal{S}$ into spherical harmonics $Y_{l,m}$ yields the *geometric mass multipoles*

$$I_l := \frac{1}{4} \int_{\mathcal{S}} \mathcal{R} Y_{l,0}(\zeta) \, dA \,. \tag{5.24}$$

Obviously, none of the $m \neq 0$ modes can contribute in axisymmetry. In [15], the I_l are defined for cross sections of axisymmetric isolated horizons together with *geometric angular momentum multipoles*

$$L_l := - \int_{\mathcal{S}} \mathrm{Im}\Psi_2 \, Y_{l,0}(\zeta) \, dA \,, \tag{5.25}$$

using the component Ψ_2 of the Weyl curvature. For isolated horizons, if the multipole moments converge for large l, then they completely characterize the horizon geometry. We do not have any angular momentum in our setup, whence the L_l all vanish for us. We also do not consider isolated horizons. On the contrary, we will compute the multipoles (5.24) in the highly dynamical regimes, where they continue to give useful results [13].

Note that for $l = 0$, we have $Y_{0,0} = 1/\sqrt{4\pi}$ and hence get

$$I_0 = \frac{1}{4} \int_{\mathcal{S}} \mathcal{R} Y_{0,0} \, dA = \frac{1}{8\sqrt{\pi}} \int_{\mathcal{S}} \mathcal{R} \, dA = \sqrt{\pi} \tag{5.26}$$

using the Gauss-Bonnet theorem for the last equality. Furthermore, our choice of invariant coordinates results in I_1 vanishing.

Note that these geometric multipoles are dimensionless. The dimensionful mass multipoles are constructed (in absence of angular momentum) from the geometric multipoles via [15]

$$M_l := \sqrt{\frac{4\pi}{2l + 1}} \frac{R_{\mathcal{S}}^{l+1}}{4\pi} \, I_l \,, \tag{5.27}$$

where $R_{\mathcal{S}} := \sqrt{A/4\pi}$ is the areal radius of $\mathcal{S}$, restoring the horizon's irreducible mass $M_{\mathrm{irr}} = \sqrt{A/16\pi} = R_{\mathcal{S}}/2 = M_0$.

In the axisymmetric Brill-Lindquist spacetimes considered here, the final state is a Schwarzschild black hole with all multipoles except I_0 vanishing. Similarly, the individual horizons are well approximated as isolated Schwarzschild black holes for
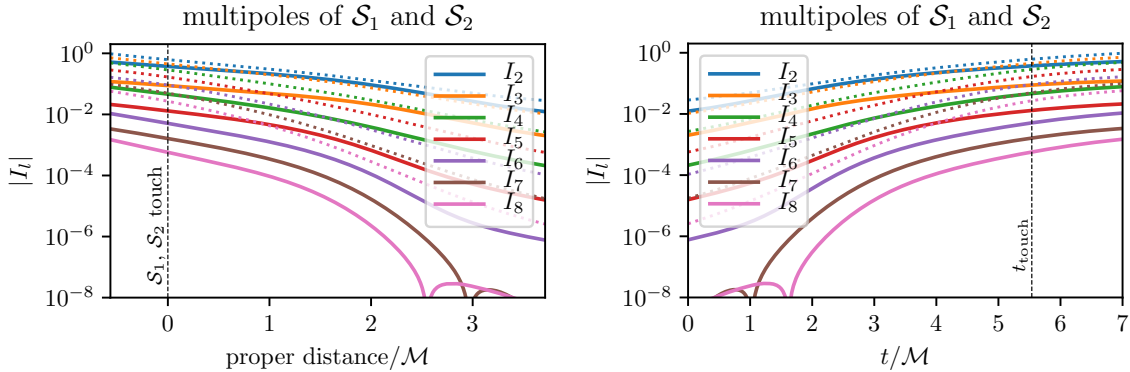
Figure 5.32: Geometric mass multipoles I_l of $\mathcal{S}_1$ (solid lines) and $\mathcal{S}_2$ (dotted lines). The multipoles are shown as function of the proper distance along the z axis (left panel) and as function of time (right panel). Note that the proper distance is here defined to be negative when the MOTSs intersect. (Figure adapted from [81].)

large distance parameters d. Since our initial data has $d = M$ somewhat small in order to have common horizons form soon after starting the evolution, we can expect the individual MOTSs $\mathcal{S}_{1,2}$ to have nontrivial multipole moments even in the initial state. This can be seen in Fig. 5.32, where the multipole moments are shown as function of the proper distance of $\mathcal{S}_1$ and $\mathcal{S}_2$ in the left panel, and as function of time in the right panel. Note that we have defined the proper distance as length of the geodesic connecting the south pole of $\mathcal{S}_1$ with the north pole of $\mathcal{S}_2$ along the z axis, and we take this value to be negative when $\mathcal{S}_{1,2}$ intersect. The invariant I_0 as well as the vanishing I_1 are not shown. The remaining multipole moments increase as the black holes approach each other during the evolution. The solid lines belong to $\mathcal{S}_1$ and are for each mode seen to be smaller than the corresponding mode of the larger horizon $\mathcal{S}_2$ shown as dotted lines.

The opposite behavior is expected for $\mathcal{S}_{\text{outer}}$, which is distorted upon formation and then loses its deformation as it approaches the Schwarzschild state. In the left panel of Fig. 5.33, we can see that this relaxation happens with the various modes initially decaying very steeply, followed by damped oscillations[4] of different frequencies for the different modes. A more detailed analysis of these frequencies will be done in Sec. 5.7.3.

Using the multipole moments, we can also visualize the fact that $\mathcal{H}_{\text{inner}}$ and $\mathcal{H}_{\text{outer}}$ connect smoothly. For this, we use the areal radius $R = \sqrt{A/4\pi}$ as a coordinate along $\mathcal{H}_{\text{inner}}$ and $\mathcal{H}_{\text{outer}}$. This is possible at least for the times close to $t_{\text{bifurcate}}$ where the horizons appear and their area is strictly monotonic. In this coordinate, the multipole

---

[4]The multipoles are here visualized on a logarithmic scale to make the behavior of the higher modes visible. Damped sinusoids hence appear as curves with a regular "arc"-like pattern.
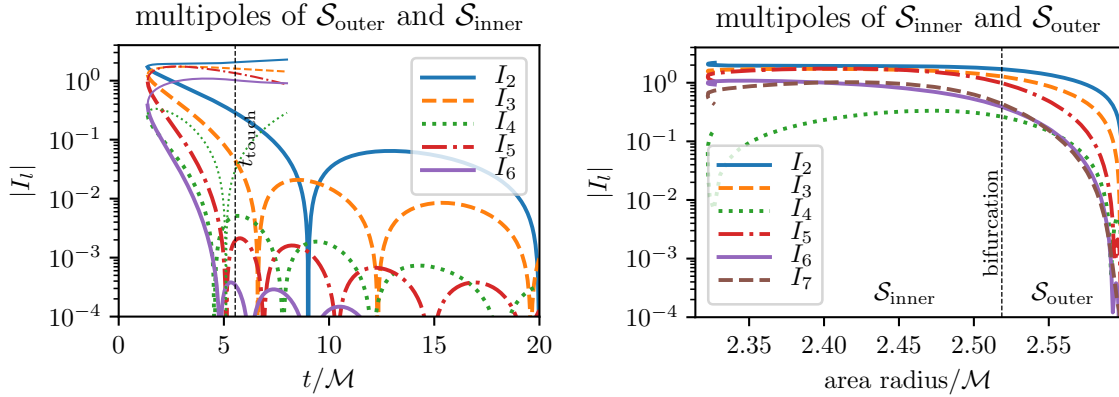
Figure 5.33: Geometric mass multipoles I_l of $\mathcal{S}_{\text{outer}}$ and $\mathcal{S}_{\text{inner}}$ as function of time (left panel) and area (right panel). In the left panel, the multipoles of $\mathcal{S}_{\text{outer}}$ are drawn as thick lines while those of $\mathcal{S}_{\text{inner}}$ are drawn as thin lines. For the same value of l, line colors and styles match between the two horizons. The right panel indicates that $\mathcal{S}_{\text{inner}}$ and $\mathcal{S}_{\text{outer}}$ together form a smooth hypersurface. (Figure adapted from [81].)

moments connect smoothly, as is demonstrated in the right panel of Fig. 5.33.

In the remainder of this section, the physical reason for the change of the area and the geometry, i.e. the fluxes of gravitational energy through the horizons, is discussed.

5.7.2 Fluxes: Shear and the ξ^A Vector Field

For future spacelike dynamical horizons, it is possible to formulate a relation, valid in exact nonlinear general relativity, between the change of area and the flux of gravitational radiation through the horizon. This is interpreted as the in-falling radiation *causing* the horizon to grow, and is in [18] described as "physical process" version of the first law of black hole mechanics. The construction is as follows. Consider a future spacelike dynamical horizon $\mathcal{H}$. A normal field on $\mathcal{H}$ will then be timelike everywhere and we shall call $\widehat{\tau}$ the unique normalized future pointing normal field. Let further $\widehat{r}$ be the unit spacelike tangent to $\mathcal{H}$ which is an outward normal to the leaves $\mathcal{S}$ of $\mathcal{H}$. Outward and inward pointing null normals of each MOTS $\mathcal{S}$ can then be defined only by the geometry of $\mathcal{H}$ via[5]

$$\widehat{\ell}^\mu := \frac{1}{\sqrt{2}}(\widehat{\tau} + \widehat{r}), \qquad\qquad \widehat{n}^\mu := \frac{1}{\sqrt{2}}(\widehat{\tau} - \widehat{r}), \qquad (5.28)$$

---

[5]These differ from the null normals defined in Eq. (2.8) only by a scaling. However, contrary to these, the null normals (5.28) cannot be defined if $\mathcal{H}$ contains portions with null signature.
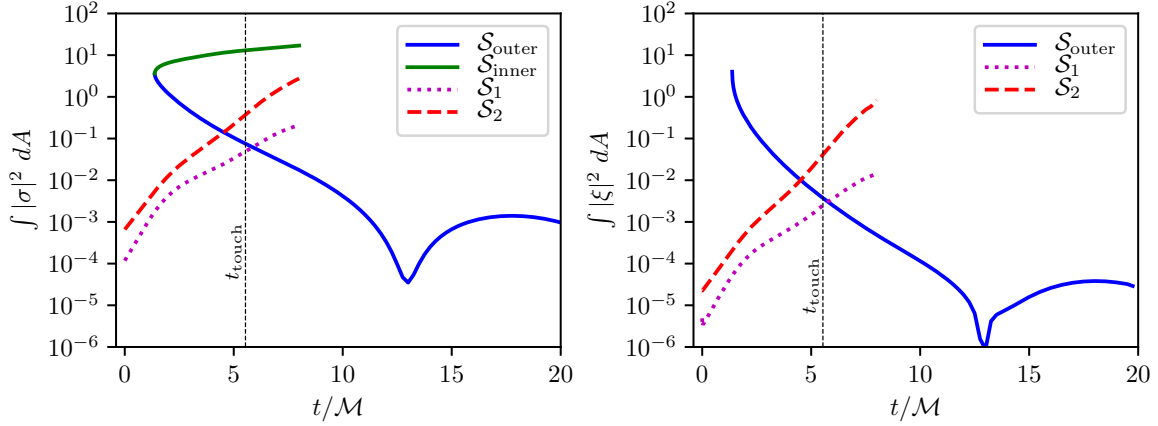
Figure 5.34: Integrals of $|\sigma|^2 := \sigma_{\mu\nu}\sigma^{\mu\nu}$ (left panel) and $|\xi|^2 := \xi^\mu \xi_\mu$ (right panel) as function of time. The latter is numerically difficult to compute for $\mathcal{S}_{\mathrm{inner}}$ due to the signature changes and is hence not shown here. (Figure adapted from [81].)

respectively. Let furthermore $\Delta\mathcal{H}$ be a portion of $\mathcal{H}$ bounded by two MOTSs with areas A_i and A_f, respectively. The balance law [18, 19] now states that their horizon radii $R = \sqrt{A/4\pi}$ satisfy a relation which in vacuum reads

$$R_f - R_i = \frac{1}{4\pi} \int_{\Delta\mathcal{H}} \left(\widehat{\sigma}_{\mu\nu}\widehat{\sigma}^{\mu\nu} + 2\widehat{\xi}_\mu \widehat{\xi}^\mu \right) N_R \, d^3V \, . \tag{5.29}$$

Here, $\widehat{\sigma}_{\mu\nu}$ is the shear of $\widehat{\ell}^\mu$ and $\widehat{\xi}^\mu := q^{\mu\nu}\widehat{r}^\rho \nabla_\rho \widehat{\ell}_\nu$. N_R is a suitable lapse function such that $N_R \, d^3V = dR \, dA$.

We will now present the results for the individual fluxes corresponding to the shear and ξ^μ fields. However, we will use the definition (2.8) and compute $\sigma_{\mu\nu}$ and ξ^μ using ℓ^μ instead of $\widehat{\ell}^\mu$. The numerically more difficult to compute quantities $\widehat{\sigma}_{\mu\nu}$ and $\widehat{\xi}^\mu$ will be left to future work. The analysis of $\sigma_{\mu\nu}$ and ξ^μ will still turn out to be fruitful.

The first result is the integral of $|\sigma|^2 := \sigma_{\mu\nu}\sigma^{\mu\nu}$ over a MOTS $\mathcal{S}$ as function of time. Fig. 5.34 shows in the left panel the computed values for all four horizons. For the individual horizons $\mathcal{H}_{1,2}$, this value increases rapidly beyond the flux through $\mathcal{H}_{\mathrm{outer}}$. The curve for $\mathcal{H}_{\mathrm{inner}}$ connects smoothly with the one for $\mathcal{H}_{\mathrm{outer}}$ and has the largest values of the four horizons. Interestingly, there is no significant effect visible when $\mathcal{H}_{\mathrm{inner}}$ pinches off at t_{touch} and then develops self-intersections, despite $|\sigma|^2$ becoming large at the neck (cf. Fig. 5.25). The flux through $\mathcal{H}_{\mathrm{outer}}$ rapidly decays after it has formed, with the beginning of an oscillating behavior visible in the part after about $t = 10\,\mathcal{M}$. The right panel of Fig. 5.34 contains the analog results for the flux of ξ^μ. Note that due to the signature change of $\mathcal{H}_{\mathrm{inner}}$, the vector ξ^μ is not well defined at the points of null signature, resulting in the integrals not converging numerically. For the

other horizons, the behavior is very similar to the shear flux, which is generally about one order of magnitude larger. Furthermore, at the times of minimal area change of $\mathcal{H}_{\text{outer}}$ (cf. Fig. 5.31), ξ^μ becomes numerically inaccurate due to the horizon becoming close to null.

To gain more insight into the dynamics of these fields on the horizons, we can perform the decomposition of the shear and ξ^μ into spherical harmonics and track the evolution of the individual modes in time. In fact, to decompose the symmetric tensor $\sigma_{\mu\nu}$ and the vector field ξ^μ, we will use the Newman-Penrose formalism to construct respective complex scalars which are then decomposed into spin-weighted spherical harmonics (SWSPH) $_sY_{l,m}$ of spin weight s suitable for their representation. To this end, we first construct a complex null tetrad $(\ell, n, m, \overline{m})$, where ℓ and n are the outward and inward pointing null normals defined by Eq. (2.8) and the complex null vector m is defined via

$$m := \frac{1}{\sqrt{2}} \left(\frac{\partial_\zeta}{\|\partial_\zeta\|} + i \frac{\partial_\varphi}{\|\partial_\varphi\|} \right) . \tag{5.30}$$

The vector $\overline{m}$ is the complex conjugate of m. The complex shear scalar is built using

$$\sigma := m^\mu m^\nu \sigma_{\mu\nu} . \tag{5.31}$$

Note that a phase change $m \to e^{i\phi} m$ results in $\sigma \to e^{2i\phi}\sigma$. The field σ hence has a spin weight of $+2$ and should be decomposed into SWSPH of spin weight $s = 2$. On the other hand, we use

$$\overline{\xi} := \overline{m}^\mu \xi_\mu \tag{5.32}$$

to obtain a scalar suitable for being decomposed into SWSPH of spin weight $s = -1$. Since we have no angular momentum or spin in our simulation, both fields will be purely real. Also, only the $_sY_{l,0}$ will contribute since the axisymmetry implies the fields will not depend on φ. We hence write

$$\sigma(\theta, \varphi, t) = \sum_{l=2}^{\infty} \sigma_l(t) \, _2Y_{l,0}(\theta, \varphi) , \tag{5.33}$$

$$\overline{\xi}(\theta, \varphi, t) = \sum_{l=1}^{\infty} \overline{\xi}_l(t) \, _{-1}Y_{l,0}(\theta, \varphi) , \tag{5.34}$$

where $\cos\theta = \zeta$.

The first ten modes of this decomposition for the shear are shown in Fig. 5.35 for all four horizons. The top two panels show the modes of the individual horizons, which increase during the evolution. The modes of the larger horizon $\mathcal{H}_2$ are generally larger than the corresponding ones for $\mathcal{H}_1$. The decay of all shown modes for $\mathcal{H}_{\text{outer}}$ is visible
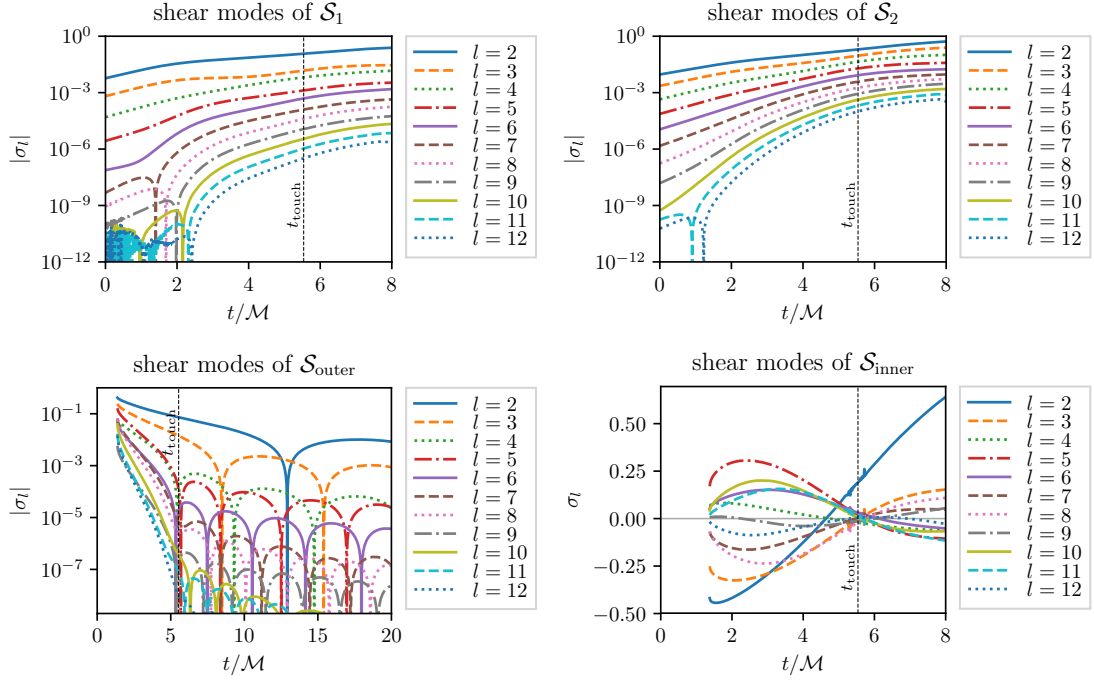
Figure 5.35: Modes σ_l of the decomposition of the shear $\sigma_{\mu\nu}$ for all four horizons. Note that all modes are purely real in our case and we take the absolute value when plotting on a logarithmic scale. (Figure adapted from [81].)

in the lower-left panel of Fig. 5.35, with the $l = 2$ mode being the dominant one. This decay will be focused on in much greater detail in the next section. For $\mathcal{H}_{\text{inner}}$ (bottom-right panel) we do not plot the modes logarithmically since they do not decay with time. Instead, the dominant mode seems to increase steadily while the other modes have a zero crossing shortly after t_{touch}. The dominant mode does not seem to be influenced by the formation of the cusp at t_{touch}, despite the signs of reduced numerical accuracy very close to t_{touch}.

As already mentioned, it is difficult to obtain accurate numerical results for ξ^μ, which is also reflected in the mode decomposition shown in Fig. 5.36. The main problems occur around $t = 13\,\mathcal{M}$, which is roughly the first minimum of the area change, as can be seen in Fig. 5.31 (bottom-left panel). We will therefore not attempt to model the decay behavior of these modes in the following subsection.

We will, however, do so for the shear modes and the multipole moments.

modes of $\bar{\xi}$ for $\mathcal{S}_{\text{outer}}$

Figure 5.36: Modes $\bar{\xi}_l$ of the ξ vector as function of time. After an initially steep decay, we see the beginning of an oscillatory behavior. However, the numerical results are unreliable near the minima of $\dot{A}$, in this case near $t = 13\,\mathcal{M}$, cf. Fig. 5.31. (Figure adapted from [81].)
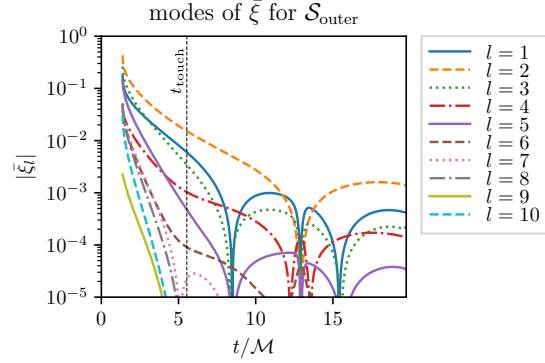
5.7.3 The Correlation with Quasi-Normal Modes

Here, we will attempt to fit a very simple model to the decaying and partially oscillating modes shown above, namely for the multipoles and the shear modes of $\mathcal{H}_{\text{outer}}$. In order to obtain more accurate results, we will use the longest simulation lasting until $t_{\max} = 50\,\mathcal{M}$. Partial results of this simulation have already been shown above in Figs. 5.26 and 5.31.

Fig. 5.37 shows in the top panel the multipole moments and in the bottom panel the shear modes for this simulation. Both cases show an initially steep decay without oscillation, followed by a much slower decay in the form of damped sinusoids. For the same mode index l, the roots of one of these seem to coincide with the extrema of the other. A simple model for all modes in both cases is

$$f_l(t) = A_l^{(1)} e^{\alpha_l^{(1)} t} + \mathrm{Re}\left(A_l^{(2)} e^{-i\alpha_l^{(2)} t} \right) , \qquad (5.35)$$

where $\alpha_l^{(1)}$ are real and model the initial fast decay, while $\alpha_l^{(2)}$ are complex in order to model the damped oscillations. The functions f_l are either the shear modes σ_l or the multipole moments I_l. A more thorough analysis will be postponed to a future work. Here we shall instead simplify further to a piecewise model of the form

$$f_l(t) = \begin{cases} A_l^{(1)} e^{\alpha_l^{(1)} t} , & t < t^{(1)} \\ \mathrm{Re}\left(A_l^{(2)} e^{-i\alpha_l^{(2)} t} \right) , & t > t^{(2)} \end{cases} , \qquad (5.36)$$

where we will set $t^{(1)} < t^{(2)}$ to separately fit the two different regimes and ignore the transition phase. The initial decay is not well modeled by a damped exponential and the results for $\alpha_l^{(1)}$ are highly dependent on the choice of $t^{(1)}$. We chose $t^{(1)} = 4\,\mathcal{M}$ which minimizes these variations. However, by construction this method will be able to accurately determine the frequencies and damping coefficients for the late time behavior, with more accurate results for larger $t^{(2)}$ (given sufficient remaining data).
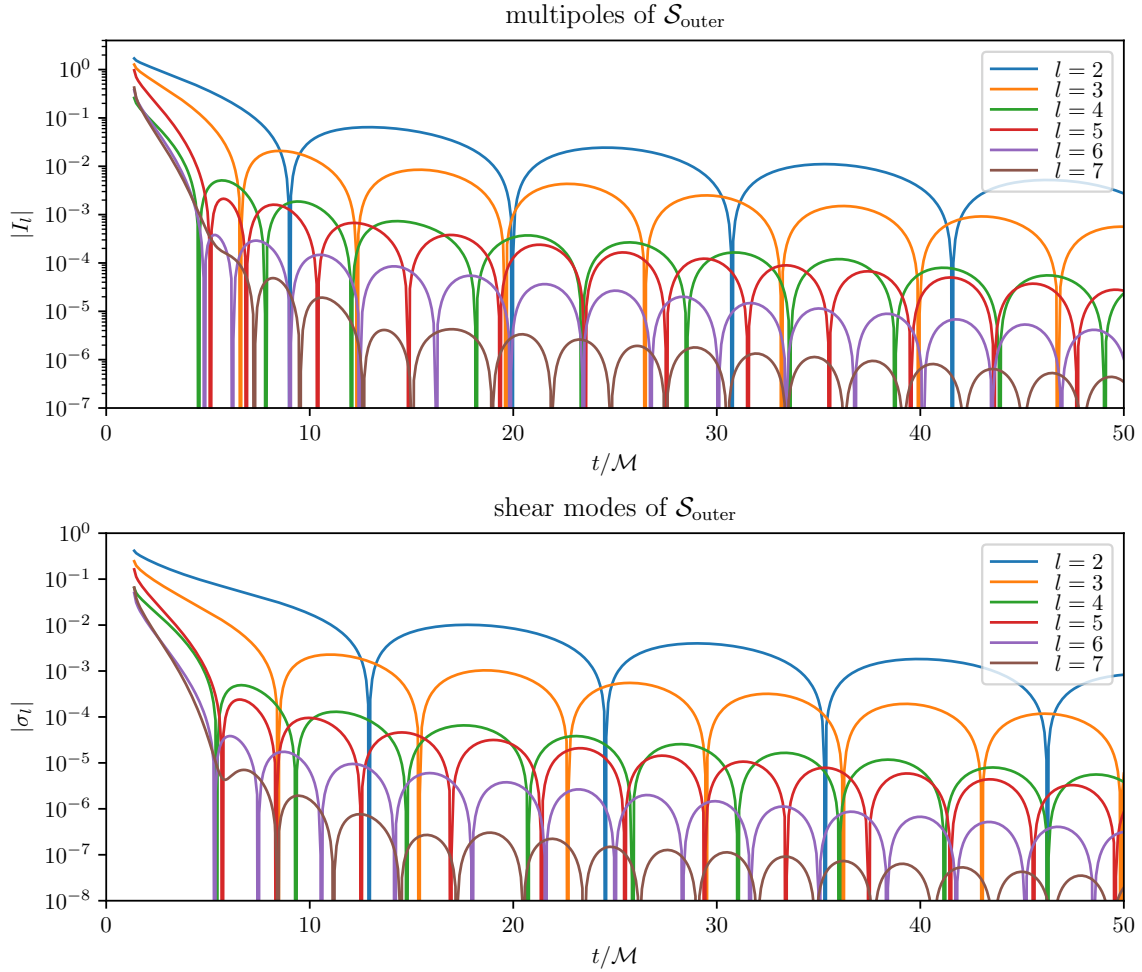
Figure 5.37: Multipoles (top panel) and shear modes (bottom panel) of $\mathcal{S}_{\text{outer}}$ for our longest simulation lasting up to $t = 50\,\mathcal{M}$. Both show qualitatively very similar behavior with an initially steep decay followed by a shallower decay with oscillations. The $l = 0$ and $l = 1$ multipole modes have been omitted since they are constant, $\sqrt{\pi}$ and 0, respectively.

For the below results, we chose $t^{(2)} = 20\,\mathcal{M}$.

The fits for the oscillating part are performed for the real and imaginary parts separately. The frequencies (real parts of $\alpha_l^{(2)}$) are determined via the roots of the respective mode f_l. For the damping coefficient, we take the local maxima of $|f_l|$ and fit an exponential. The results are shown in Figs. 5.38 and 5.39 with the damping parameter values summarized in Tables 5.1 and 5.2. We find very good agreement of the late time behavior between the multipoles and shear modes. In fact, they are equal within the accuracy we estimate for these values. We do not give an error estimate for the initial damping parameters as this model does not seem to be well suited, compare

also the dotted orange lines indicating this fit in Figs. 5.38 and 5.39. A more careful modeling is required to extract more reliable information from this initial part.

We find a most interesting correspondence of our values with certain quasi-normal mode frequencies of a Schwarzschild black hole. These quasi-normal modes appear in the context of linear perturbations of fixed black hole background spacetimes and describe the universal characteristic oscillations present when a perturbed Kerr or Schwarzschild black hole spacetime settles down. They are fully determined by the mass and spin of the black hole and present a set of complex frequencies, with the imaginary part containing the inverse decay time scale and the real part being the oscillation frequency. They are labeled by three integers (n, l, m) where (l, m) describe the angular components (corresponding to our l and m angular "quantum" numbers). A set of frequencies for fixed l and m is then assigned an *overtone index n* in order of increasing damping factors (i.e. imaginary parts), with $n = 0$ being the longest lived *fundamental mode*. See [26] for a review. For the Schwarzschild case considered here, only the $m = 0$ mode is relevant. We collect in Tab. 5.3 the first few $m = 0$ modes for Schwarzschild, taken from [25]; see also [26, 27].

A comparison of these values with Tables 5.1 and 5.2 reveals a striking agreement of the frequencies $\mathrm{Re}(\alpha_l^{(2)})$ we find with the corresponding quasi-normal mode for the same value of l for $n = 0$. The damping coefficients $\mathrm{Im}(\alpha_l^{(2)})$ agree less well, but show a similarity in that they do not depend strongly on l. We find no immediate correspondence of the initial damping coefficients $\alpha_l^{(1)}$ with any quasi-normal mode.

As the quasi-normal mode oscillations can be found in the wave zone, it is surprising to see their presence in quasilocal quantities computed only at the horizon. Obviously, the frequencies and damping coefficients we calculate highly depend on the time coordinate used in the simulations. As far as we are aware, a fundamental theoretical understanding of why our gauge conditions lead to this direct correspondence without requiring any further conversion is, as of yet, missing.
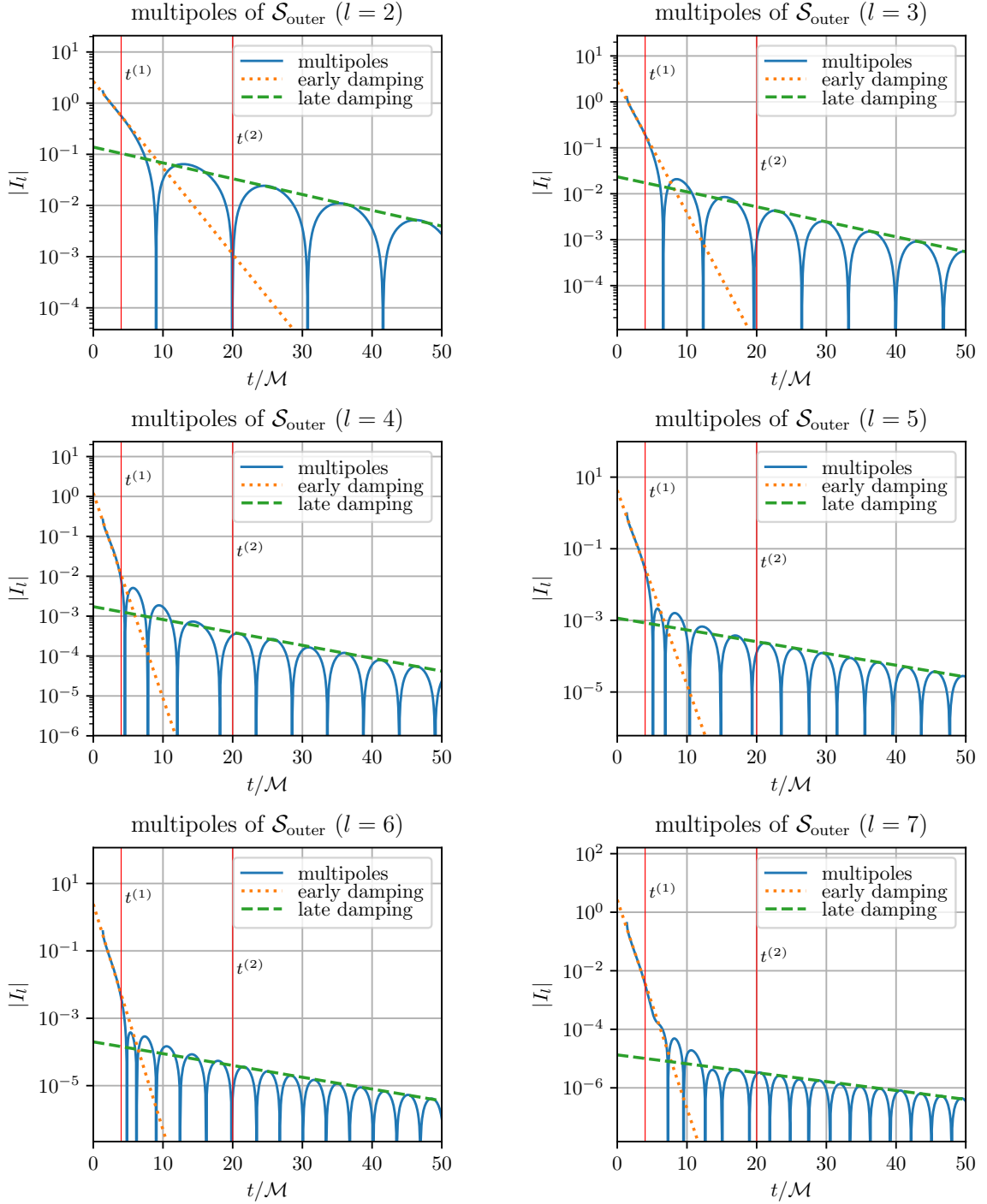
Figure 5.38: Fits of the multipole moments $I_2, \dots, I_7$ using the piecewise model of Eq. (5.36). The solid line shows the respective mode and the two vertical thin lines the two times $t^{(1)}$, $t^{(2)}$ used for the fits. The dotted orange line indicates the exponential fit of the initial steep decay while the green dashed line shows the damping part of the late time fits. (Figure adapted from [81].)
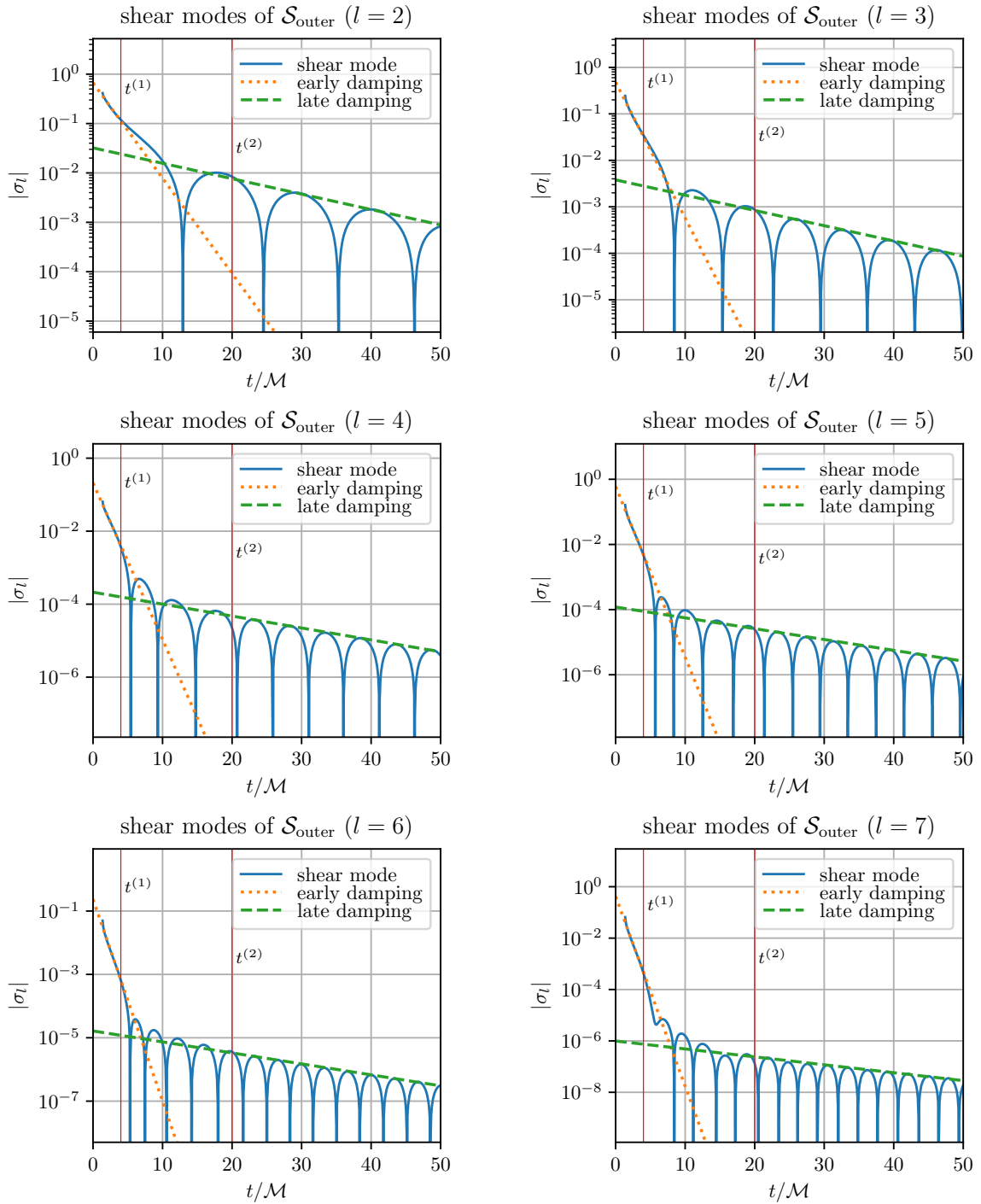
Figure 5.39: Fits of the shear modes $\sigma_2, \ldots, \sigma_7$ again using the piecewise model of Eq. (5.36). Otherwise similar to Fig. 5.38. (Figure adapted from [81].)

l	$\alpha_l^{(1)}$	$\mathrm{Re}(\alpha_l^{(2)})$	$\mathrm{Im}(\alpha_l^{(2)})$
2	-0.506	0.377	-0.092
3	-0.853	0.604	-0.098
4	-1.540	0.796	-0.097
5	-1.625	1.014	-0.098
6	-2.006	1.216	-0.105
7	-2.134	1.410	-0.091

Table 5.1: Multipole damping coefficients of the piecewise model (5.36) with $t^{(1)} = 4\,\mathcal{M}$ and $t^{(2)} = 20\,\mathcal{M}$. We estimate an accuracy of $1\,\%$ for the real parts (frequencies) of $\alpha_l^{(2)}$ and $10\,\%$ for the imaginary parts (damping) for $l \leq 6$. All values have been scaled to correspond to a $M = 1$ simulation.

l	$\alpha_l^{(1)}$	$\mathrm{Re}(\alpha_l^{(2)})$	$\mathrm{Im}(\alpha_l^{(2)})$
2	-0.578	0.377	-0.093
3	-0.875	0.602	-0.098
4	-1.285	0.800	-0.098
5	-1.568	1.013	-0.099
6	-1.907	1.212	-0.104
7	-2.211	1.414	-0.092

Table 5.2: As in Tab. 5.1 (incl. the error estimates) but for the fits of the shear modes.

	$n = 0$		$n = 1$		$n = 2$		$n = 3$	
	Re	Im	Re	Im	Re	Im	Re	Im
$l = 2$	0.3737	-0.0890	0.3467	-0.2739	0.3011	-0.4783	0.2515	-0.7051
$l = 3$	0.5994	-0.0927	0.5826	-0.2813	0.5517	-0.4791	0.5120	-0.6903
$l = 4$	0.8092	-0.0942	0.7966	-0.2843	0.7727	-0.4799	0.7398	-0.6839
$l = 5$	1.0123	-0.0949	1.0022	-0.2858	0.9827	-0.4803	0.9550	-0.6806
$l = 6$	1.2120	-0.0953	1.2036	-0.2866	1.1871	-0.4806	1.1633	-0.6786
$l = 7$	1.4097	-0.0955	1.4025	-0.2872	1.3882	-0.4807	1.3674	-0.6773

Table 5.3: The first few complex Schwarzschild quasi-normal mode frequencies with $m = 0$ for the fundamental mode ($n = 0$) and the first three overtones ($n = 1, 2, 3$). The real part represents the frequency and the imaginary part the damping coefficient. Taken from [25].

Chapter 6

Steps towards dropping axisymmetry

From a numerical perspective, the obvious next step is to generalize our new horizon finder and drop the requirement of axisymmetry. The most relevant numerical simulations for astrophysical situations are, of course, not axisymmetric. This generalization will therefore open up a wide window into observationally relevant scenarios and presents the logical continuation of this project.

Given that axisymmetry presents a severe restriction and dramatically simplifies the numerical task—the nonlinear problem of finding our horizon function h becomes a one-dimensional ordinary differential equation—one might ask whether the method can, in principle, be generalized. Fortunately, while developing the new algorithm, the goal of applying it in the fully generic case was set from the beginning and all steps specific to the axisymmetric case were carefully evaluated for applicability in the planned generalization. Even though the presentation of the numerical method in Chapter 3 specializes to axisymmetry starting from Sec. 3.3, the main idea enabling the representation of non-star-shaped and even self-intersecting MOTSs is fully general.

The remainder of this chapter will describe the main differences to the axisymmetric case from a numerical viewpoint in Sec. 6.1, where problems and strategies to solve them are presented. Our first working implementation will be discussed in Sec. 6.2. There, first results of MOTSs in non-axisymmetric initial data are shown, providing a "proof-of-concept" that the new algorithm can indeed be generalized. Sec. 6.3 will conclude this chapter by summarizing the current status and future tasks for arriving at a fully functional finder.

6.1 Numerical Method

Numerically, most of the discussion of Chapter 3 still applies. The differences to the axisymmetric case occur at two main points:

- The reference shape representation needs to be capable of representing arbitrary closed smooth two-dimensional surfaces. This includes non-star-shaped surfaces and self-intersections.

- The linear steps in the non-linear search described in Sec. 3.2.2 become partial differential equations for the horizon function $h : S^2 \to \mathbb{R}$.

These two aspects will now be discussed in turn.

Let $\mathcal{S}$ be an arbitrary smooth closed two-dimensional surface. As before, we will restrict ourselves to surfaces of spherical topology. Without axisymmetry, we can no longer represent $\mathcal{S}$ as a surface of revolution of a curve. A parametric representation of $\mathcal{S}$ satisfying all the requirements while still being numerically efficient is the following. Let S_i, $i = 1, 2, 3$, be mappings $S^2 \to \mathbb{R}$, represented as an expansion into (real) spherical harmonics $Y_{lm}(\theta, \varphi)$, where (θ, φ) are coordinates on S^2. That is, we have three functions

$$S_i(\theta, \varphi) = \sum_{l=0}^{N-1} \sum_{m=-l}^{l} a_{lm}^{(i)} \, Y_{lm}(\theta, \varphi) \, . \tag{6.1}$$

The three finite sets of each N^2 coefficients $a_{lm}^{(i)}$ then represent $\mathcal{S}$ by taking S_i to be the component functions of a parametrization of $\mathcal{S}$ in the numerical coordinates.

The reference-shape based parametrization of a MOTS $\mathcal{S}$ is then given by Eq. (3.5), as in the axisymmetric case, with a parametric reference surface $\mathcal{S}_{\text{ref}}$ represented as above and a horizon function $h : S^2 \to \mathbb{R}$, which itself is again represented as a finite sum of spherical harmonics with coefficients a_{lm}.

The second aspect mentioned above is solving the nonlinear problem using a Newton-like search with linear steps as described in Sec. 3.2.2. The numerical representation of h as a sum of spherical harmonics lends itself ideally to the pseudospectral method described in that section, with two aspects that need attention: The first is that the finite set of indices (l, m) of the coefficients a_{lm} needs to be converted to a single index $n = 0, \ldots, N^2 - 1$. The second is more difficult, as we need to choose a set of N^2 collocation points on S^2 in order to turn Eq. (3.27) into a determined linear system of equations. One common strategy is to take the so-called "Lat-Long" grid of $2N^2$ points (cf. [74])

$$\left\{ (\theta_i, \varphi_j) = \left(\arccos(g_i^N), 2\pi \frac{j}{2N} \right) : i = 0, 1, \ldots, N-1, \; j = 0, 1, \ldots, 2N - 1 \right\} \, , \tag{6.2}$$

where g_i^N are the N roots of the N'th Legendre polynomial. With these points, Eq. (3.27) is overdetermined and usually solved using a least-squares algorithm. We have experimented with different choices of collocation points. Fig. 6.1 shows three examples, the "Lat-Long" grid of Eq. (6.2) in the left panel and two choices based on generalized spiral points [90] in the middle and right panels. We have not yet found a set of N^2 collocation points in closed form producing a determined set of N^2 equations of full rank. Finding such an optimum set would reduce the computational cost and is deferred to future work.
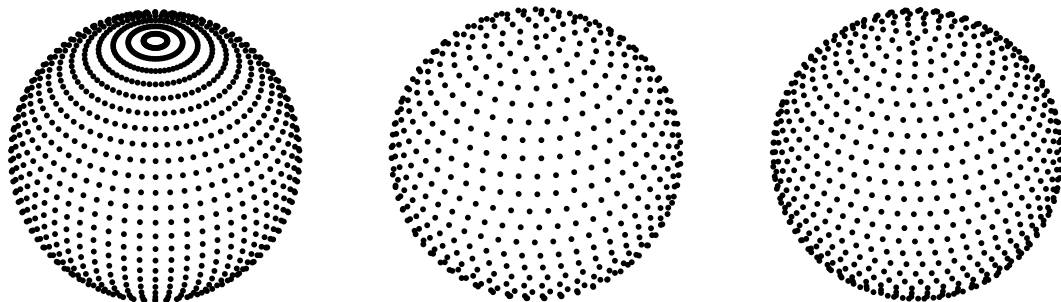
Figure 6.1: Different choices of collocation points on the sphere. The left panel shows the usual "Lat-Long" grid for $N = 30$. In this case, we have $N^2 = 900$ basis functions and $2N^2 = 1800$ collocation points. The resulting $(N^2, 2N^2)$ matrix appearing in the pseudospectral method has a condition number of ≈ 5.1 and the (solvable) overdetermined system of equations can thus be solved accurately using a least-squares solver. The other two panels show two choices of generalized spiral points with 900 points in the middle panel and 1156 points in the right panel. Unfortunately, the 900 points in the middle panel lead to an ill-conditioned system with condition number $> 10^{16}$. Adding points to this set leads again to an overdetermined problem. However, with the 1156 points shown in the right panel, the condition number becomes ≈ 1.7 and a least-squares solver produces an accurate solution.

6.2 Results for a Time Symmetric Case

In order to test the generalized MOTS finder algorithm we proceed similarly to the axisymmetric case and start with time symmetric initial data. A non-axisymmetric configuration can easily be obtained using, again, a Brill-Lindquist metric of the form (4.3) by choosing three punctures to construct the conformal factor Eq. (4.5). The punctures are initially all aligned on the same axis, so that our tested and validated axisymmetric finder can be used to obtain the first set of MOTSs. The result has already been shown in Fig. 4.1. The surfaces of revolution are then represented as described in Sec. 6.1 and used as initial guess for the generalized finder, which successfully reproduced the axisymmetric results. Subsequently, the three punctures are moved in small steps away from being aligned on one axis, yielding a non-axisymmetric configuration. After each step, the previous MOTSs are used as reference surfaces and initial guesses for the respective next search. Fig. 6.2 shows the result after a few steps, indicating that the concept has been successfully implemented and is in principle able to be used for realistic cases of two inspiralling black holes.

Figure 6.2: Example of non-axisymmetric MOTSs in a 3-black-hole configuration. Starting with the configuration shown in Fig. 4.1, the puncture at $z_1 = -0.45$ is rotated to remove the symmetry. The generalized MOTS finder successfully tracks all 9 MOTSs, including the non-star-shaped inner MOTS containing all three punctures.
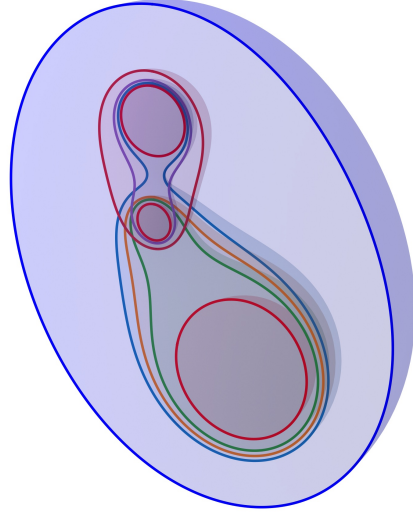
6.3 Future of the Generalized MOTS Finder

The main open tasks in the development of the general MOTS finder are increasing the numerical efficiency and generalizing the Hermite interpolation described in Sec. 5.3 to the case of 3-dimensional grids. Furthermore, the definitions and computations of several of the physical properties presented throughout Chapters 4 and 5 need to be revisited. For example, in full generality, we do not have access to an invariantly defined angular coordinate system (ζ, φ) which exists in axisymmetry. This poses additional complications in the definition of the decomposition of fields like the shear and the intrinsic Ricci scalar into spherical harmonics. If the horizon asymptotes to an axisymmetric state, which is the case for the outermost horizon, or originates from a nearly axisymmetric state, like the individual MOTSs when they are initially well separated, then a prescription exists to transport the coordinates along the dynamical horizons. This procedure is described in [13].

Chapter 7

Conclusions

The project of this dissertation started out with the goal to better understand the merger process of two black holes in terms of their dynamical horizons. The axisymmetric configuration was originally meant to be a "test case" used to develop and validate a new MOTS finding algorithm that overcomes the limitations imposed by the extant algorithms. However, the numerous surprising results generated in even the seemingly simple Brill-Lindquist configuration studied throughout this work—including the appearance of self-intersecting horizons, the cusp-formation during the MOTS merger, and the area anomaly of the inner horizon—has resulted in a number of smaller and larger projects centered around the axisymmetric case. The present work collects these findings and aims at providing a first interpretation.

The original goal has been achieved: The merger of MOTSs found in the head-on collision of two non-spinning black holes yields a connected history, where we can follow the dynamical horizons from the initial state of two disjoint black holes to the final remnant black hole. As a result, we now have the quasilocal analog of the "pair-of-pants" picture describing such a merger in terms of the event horizon. Furthermore, the suggested possibility that the MOTSs annihilate when they merge turned out to not occur. Instead, after the time the inner common MOTS coincides with the union of the two individual MOTSs, each continue to exist separately. The individual horizons then intersect each other, while the inner common MOTS, quite unexpectedly, is seen to self-intersect.

Obtaining these results required the design and implementation of a new algorithm for finding highly distorted MOTSs with high accuracy. We have encountered no case where our finder could not, at least in principle, find a MOTS that exists. Failure of a MOTS being located could be attributed to either insufficient resolution of the numerical simulation, or the formation of a cusp in the MOTS geometry requiring exponentially increasing resolution of the MOTS representation. All other cases of MOTSs vanishing happened in families of time-symmetric initial data, where a detailed analysis of the MOTS stability operator revealed physical instability as cause for the MOTS actually disappearing from the configuration.

In the dynamical case, the evolution of the spectrum of the MOTS stability operator is shown to provide useful insights into the horizon dynamics, although more can be

gained from a more detailed analysis of the global properties, especially for the inner common horizon.

Geometrically, we find that dynamical horizons appear in a larger variety than often considered in the literature, including in proofs of the area increase law for dynamical horizons. The outermost horizon is not always future trapped and the inner horizon is seen to never be completely future or past trapped, while its signature undergoes several characteristic changes. The area anomaly found in the evolution of this inner horizon is related to these signature changes and does not contradict the area monotonicity results of, e. g., Bousso & Engelhardt. This area increase just before the MOTS merger could potentially contain as yet unknown important physical information. A deeper understanding of this behavior could possibly lead to an application in a proof of the Penrose inequality for binary black hole mergers using the connected history of MOTSs.

The analysis of the evolution of multipole moments and gravitational fluxes through the outermost horizon shows a striking and not yet fully understood correspondence of their decay behavior with the quasi-normal modes of a Schwarzschild black hole. However, it is consistent with a strong correlation between the gravitational radiation observed at infinity and the horizon dynamics.

In summary, the contribution this work provides is twofold: On the technical side, we have devised a new method capable of finding horizons that could not be located previously, and our implementation of this method has been made publicly available. Thus far, we have looked at only a small set of physical configurations where this algorithm was able to uncover new results. In the future, the generalization to non-axisymmetric situations, with a working proof-of-concept already presented here, will be able to extend the applicability to astrophysically relevant configurations.

The first configuration analysed with the new method, namely the axisymmetric two-black-hole Brill-Lindquist setup, already generated the main physical contribution—the merger of MOTSs, which finally completes the picture of a binary black hole merger in terms of quasilocal horizons. From future analyses of mergers with nonzero orbital angular momentum, we will be able to answer whether and how these mergers of MOTSs happen in full generality.

All the horizons analysed in this work are, of course, hidden in the black hole region and thus no information about their behavior can reach an observer at infinity. However, there is a connection to the observable regime, since the region close to the horizons is the common source of the gravitational radiation partly entering the horizons and partly escaping. The surprisingly direct correspondence of quasi-normal modes with the behavior of fields on the horizon found in the axisymmetric case promises to be fruitful for further research.

Bibliography

[1] B. P. Abbott et al. "Binary Black Hole Mergers in the first Advanced LIGO Observing Run". In: *Phys. Rev.* X6.4 (2016). [erratum: Phys. Rev.X8, no.3, 039903(2018)], 041015. DOI: 10.1103/PhysRevX.6.041015, 10.1103/PhysRevX.8.039903. arXiv: 1606.04856 [gr-qc].

[2] B. Abbott et al. "GWTC-1: A Gravitational-Wave Transient Catalog of Compact Binary Mergers Observed by LIGO and Virgo during the First and Second Observing Runs". In: *Phys. Rev. X* 9.3 (2019), 031040. DOI: 10.1103/PhysRevX.9.031040. arXiv: 1811.12907 [astro-ph.HE].

[3] K. Akiyama et al. "First M87 Event Horizon Telescope Results. I. The Shadow of the Supermassive Black Hole". In: *Astrophys. J.* 875.1 (2019), L1. DOI: 10.3847/2041-8213/ab0ec7. arXiv: 1906.11238 [astro-ph.GA].

[4] M. Alcubierre et al. "Gauge conditions for long term numerical black hole evolutions without excision". In: *Phys. Rev.* D67 (2003), 084023. DOI: 10.1103/PhysRevD.67.084023. arXiv: gr-qc/0206072 [gr-qc].

[5] M. Alcubierre et al. "Symmetry without symmetry: Numerical simulation of axisymmetric systems using Cartesian grids". In: *Int. J. Mod. Phys.* D10 (2001), 273–290. DOI: 10.1142/S0218271801000834. arXiv: gr-qc/9908012 [gr-qc].

[6] M. Alcubierre et al. "Towards a stable numerical evolution of strongly gravitating systems in general relativity: The Conformal treatments". In: *Phys. Rev.* D62 (2000), 044034. DOI: 10.1103/PhysRevD.62.044034. arXiv: gr-qc/0003071 [gr-qc].

[7] L. Andersson, M. Mars, and W. Simon. "Local existence of dynamical and trapping horizons". In: *Phys.Rev.Lett.* 95 (2005), 111102. DOI: 10.1103/PhysRevLett.95.111102. arXiv: gr-qc/0506013 [gr-qc].

[8] L. Andersson, M. Mars, and W. Simon. "Stability of marginally outer trapped surfaces and existence of marginally outer trapped tubes". In: *Adv.Theor.Math.Phys.* 12 (2008). arXiv: 0704.2889 [gr-qc].

[9] M. Ansorg, B. Brügmann, and W. Tichy. "A single-domain spectral method for black hole puncture data". In: *Phys. Rev. D* 70 (2004), 064011. DOI: 10.1103/PhysRevD.70.064011. eprint: arXiv:gr-qc/0404056.

[10] A. Ashtekar, C. Beetle, and S. Fairhurst. "Isolated horizons: A generalization of black hole mechanics". In: *Class. Quant. Grav.* 16 (1999), L1–L7. DOI: 10.1088/0264-9381/16/2/027. arXiv: gr-qc/9812065.

[11] A. Ashtekar, C. Beetle, and S. Fairhurst. "Mechanics of Isolated Horizons". In: *Class. Quant. Grav.* 17 (2000), 253–298. DOI: 10.1088/0264-9381/17/2/301. arXiv: gr-qc/9907068.

[12] A. Ashtekar, C. Beetle, and J. Lewandowski. "Mechanics of Rotating Isolated Horizons". In: *Phys. Rev.* D64 (2001), 044016. DOI: 10.1103/PhysRevD.64.044016. arXiv: gr-qc/0103026.

[13] A. Ashtekar, M. Campiglia, and S. Shah. "Dynamical Black Holes: Approach to the Final State". In: *Phys. Rev.* D88.6 (2013), 064045. DOI: 10.1103/PhysRevD.88.064045. arXiv: 1306.5697 [gr-qc].

[14] A. Ashtekar and A. Corichi. "Laws governing isolated horizons: Inclusion of dilaton couplings". In: *Class. Quant. Grav.* 17 (2000), 1317–1332. DOI: 10.1088/0264-9381/17/6/301. arXiv: gr-qc/9910068.

[15] A. Ashtekar, J. Engle, T. Pawłowski, and C. Van Den Broeck. "Multipole moments of isolated horizons". In: *Class. Quant. Grav.* 21 (2004), 2549–2570. DOI: 10.1088/0264-9381/21/11/003. arXiv: gr-qc/0401114.

[16] A. Ashtekar, S. Fairhurst, and B. Krishnan. "Isolated horizons: Hamiltonian evolution and the first law". In: *Phys. Rev.* D62 (2000), 104025. DOI: 10.1103/PhysRevD.62.104025. arXiv: gr-qc/0005083.

[17] A. Ashtekar and G. J. Galloway. "Some uniqueness results for dynamical horizons". In: *Adv. Theor. Math. Phys.* 9.1 (2005), 1–30. DOI: 10.4310/ATMP.2005.v9.n1.a1. arXiv: gr-qc/0503109.

[18] A. Ashtekar and B. Krishnan. "Dynamical horizons and their properties". In: *Phys. Rev.* D68 (2003), 104030. DOI: 10.1103/PhysRevD.68.104030. arXiv: gr-qc/0308033.

[19] A. Ashtekar and B. Krishnan. "Dynamical horizons: Energy, angular momentum, fluxes and balance laws". In: *Phys. Rev. Lett.* 89 (2002), 261101. DOI: 10.1103/PhysRevLett.89.261101. arXiv: gr-qc/0207080.

[20] A. Ashtekar and B. Krishnan. "Isolated and dynamical horizons and their applications". In: *Living Rev. Rel.* 7 (2004), 10. arXiv: gr-qc/0407042.

[21] T. W. Baumgarte and S. L. Shapiro. *Numerical Relativity: Solving Einstein's Equations on the Computer.* Cambridge University Press, 2010. DOI: 10.1017/CBO9781139193344.

[22] I. Ben-Dov. "The Penrose inequality and apparent horizons". In: *Phys. Rev.* D70 (2004), 124031. DOI: 10.1103/PhysRevD.70.124031. arXiv: gr-qc/0408066 [gr-qc].

[23] M. Berry. "Semiclassical mechanics of regular and irregular motion". In: *Comportement chaotique des systèmes déterministes*. Ed. by G. Iooss, R. H. G. Helleman, and R. Stora. North-Holland. Les Houches, session XXXVI. 1981, 173–271.

[24] M. Berry, I. Percival, and N. Weiss. "Quantum chaology". In: *Proc. Roy. Soc. London A* 413 (1987), 183–198.

[25] E. Berti. https://pages.jh.edu/~eberti2/ringdown/.

[26] E. Berti, V. Cardoso, and A. O. Starinets. "Quasinormal modes of black holes and black branes". In: *Class. Quant. Grav.* 26 (2009), 163001. DOI: 10.1088/0264-9381/26/16/163001. arXiv: 0905.2975 [gr-qc].

[27] E. Berti, V. Cardoso, and C. M. Will. "On gravitational-wave spectroscopy of massive black holes with the space interferometer LISA". In: *Phys. Rev. D* 73 (2006), 064030. DOI: 10.1103/PhysRevD.73.064030. arXiv: gr-qc/0512160.

[28] H. Bondi, M. van der Burg, and A. Metzner. "Gravitational waves in general relativity. 7. Waves from axisymmetric isolated systems". In: *Proc. Roy. Soc. Lond. A* A269 (1962), 21–52. DOI: 10.1098/rspa.1962.0161.

[29] I. Booth, R. Hennigar, and S. Mondal. "Marginally outer trapped (open) surfaces and extreme mass ratio mergers". In: (May 2020). arXiv: 2005.05350 [gr-qc].

[30] R. Bousso and N. Engelhardt. "New Area Law in General Relativity". In: *Phys. Rev. Lett.* 115.8 (2015), 081301. DOI: 10.1103/PhysRevLett.115.081301. arXiv: 1504.07627 [hep-th].

[31] R. Bousso and N. Engelhardt. "Proof of a New Area Law in General Relativity". In: *Phys. Rev.* D92.4 (2015), 044031. DOI: 10.1103/PhysRevD.92.044031. arXiv: 1504.07660 [gr-qc].

[32] J. Boyd. *Chebyshev and Fourier Spectral Methods*. Dover Publications, New York, 2001.

[33] M. Boyle. *spinsfast: Fast and exact spin-s spherical-harmonic transforms*. Version v2.0. Apr. 2018. DOI: 10.5281/zenodo.1221354.

[34] H. L. Bray. "Proof of the Riemannian Penrose Inequality Using the Positive Mass Theorem". In: *J. Differential Geom.* 59.2 (Oct. 2001), 177–267. DOI: 10.4310/jdg/1090349428.

[35] D. R. Brill and R. W. Lindquist. "Interaction energy in geometrostatics". In: *Phys. Rev.* 131 (1963), 471–476. DOI: 10.1103/PhysRev.131.471.

[36] J. D. Brown, P. Diener, O. Sarbach, E. Schnetter, and M. Tiglio. "Turduckening black holes: an analytical and computational study". In: *Phys. Rev. D* 79 (2009), 044023. DOI: 10.1103/PhysRevD.79.044023. eprint: arXiv:0809.3533[gr-qc].

[37] C. Canuto, M. Y. Hussaini, A. Quarteroni, and T. A. Zang. *Spectral Methods: Fundamentals in Single Domains.* Springer Verlag, 2006.

[38] M. Droettboom et al. *matplotlib/matplotlib v2.2.2.* Mar. 2018. DOI: 10.5281/zenodo.1202077.

[39] *Einstein Toolkit: Open software for relativistic astrophysics.* http://einsteintoolkit.org/.

[40] R. Emparan and D. Marin. "Precursory collapse in Neutron Star-Black Hole mergers". In: *Phys. Rev. D* 102.2 (2020), 024009. DOI: 10.1103/PhysRevD.102.024009. arXiv: 2004.08143 [gr-qc].

[41] C. Evans, D. Ferguson, B. Khamesra, P. Laguna, and D. Shoemaker. "Inside the Final Black Hole: Puncture and Trapped Surface Dynamics". In: (Apr. 2020). arXiv: 2004.11979 [gr-qc].

[42] X. J. Forteza, S. Bhagwat, P. Pani, and V. Ferrari. "On the spectroscopy of binary black hole ringdown using overtones and angular modes". In: (May 2020). arXiv: 2005.03260 [gr-qc].

[43] M. Giesler, M. Isi, M. A. Scheel, and S. Teukolsky. "Black Hole Ringdown: The Importance of Overtones". In: *Phys. Rev. X* 9.4 (2019), 041060. DOI: 10.1103/PhysRevX.9.041060. arXiv: 1903.08284 [gr-qc].

[44] D. Giulini. "Dynamical and Hamiltonian Formulation of General Relativity". In: *Springer handbook of spacetime.* Ed. by A. Ashtekar and V. Petkov. Springer, 2014. Chap. 17.

[45] C. Gundlach. "Pseudospectral apparent horizon finders: An efficient new algorithm". In: *Physical Review D* 57.2 (1998), 863.

[46] A. Gupta, B. Krishnan, A. Nielsen, and E. Schnetter. "Dynamics of marginally trapped surfaces in a binary black hole merger: Growth and approach to equilibrium". In: *Phys. Rev.* D97.8 (2018), 084028. DOI: 10.1103/PhysRevD.97.084028. arXiv: 1801.07048 [gr-qc].

[47] S. Hawking and G. Ellis. *The Large Scale Structure of Space-Time*. Cambridge Monographs on Mathematical Physics. Cambridge University Press, Feb. 2011. ISBN: 978-0-521-20016-5, 978-0-521-09906-6, 978-0-511-82630-6, 978-0-521-09906-6. DOI: `10.1017/CBO9780511524646`.

[48] S. Hawking and R. Penrose. "The Singularities of gravitational collapse and cosmology". In: *Proc. Roy. Soc. Lond. A* A314 (1970), 529–548. DOI: `10.1098/rspa.1970.0021`.

[49] S. Hawking. "The occurrence of singularities in cosmology. III. Causality and singularities". In: *Proc. Roy. Soc. Lond. A* A300 (1967), 187–201. DOI: `10.1098/rspa.1967.0164`.

[50] S. Hayward. "General laws of black hole dynamics". In: *Phys.Rev.* D49 (1994), 6467–6474. DOI: `10.1103/PhysRevD.49.6467`.

[51] S. A. Hayward. "Angular momentum conservation for dynamical black holes". In: *Phys. Rev.* D74 (2006), 104013. DOI: `10.1103/PhysRevD.74.104013`. arXiv: `gr-qc/0609008`.

[52] S. A. Hayward. "Energy and entropy conservation for dynamical black holes". In: *Phys. Rev.* D70 (2004), 104027. DOI: `10.1103/PhysRevD.70.104027`. arXiv: `gr-qc/0408008`.

[53] S. A. Hayward. "Spin coefficient form of the new laws of black hole dynamics". In: *Class. Quant. Grav.* 11 (1994), 3025–3036. DOI: `10.1088/0264-9381/11/12/016`. arXiv: `gr-qc/9406033`.

[54] S. Holmes and W. Featherstone. "A simple and stable approach to high degree and order spherical harmonic synthesis". In: *Vistas for Geodesy in the New Millennium*. Springer, 2002, 259–264.

[55] G. Huisken and T. Ilmanen. "The Inverse Mean Curvature Flow and the Riemannian Penrose Inequality". In: *J. Differential Geom.* 59.3 (Nov. 2001), 353–437. DOI: `10.4310/jdg/1090349447`.

[56] J. D. Hunter. "Matplotlib: A 2D graphics environment". In: *Computing in Science & Engineering* 9.3 (2007), 90–95. DOI: `10.1109/MCSE.2007.55`.

[57] S. Husa, I. Hinder, and C. Lechner. "Kranc: a Mathematica application to generate numerical codes for tensorial evolution equations". In: *Comput. Phys. Commun.* 174 (2006), 983–1004. eprint: `arXiv:gr-qc/0404023`.

[58] J. Jaramillo, R. Macedo, P. Moesta, and L. Rezzolla. "Towards a cross-correlation approach to strong-field dynamics in Black Hole spacetimes". In: *AIP Conf. Proc.* 1458.1 (2012). Ed. by J. Beltran Jimenez, J. A. Ruiz Cembranos, A. Dobado, A. Lopez Maroto, and A. De la Cruz Dombriz, 158–173. DOI: `10.1063/1.4734411`. arXiv: `1205.3902 [gr-qc]`.

[59] J. L. Jaramillo. "Black hole horizons and quantum charged particles". In: *Class. Quant. Grav.* 32.13 (2015), 132001. DOI: 10.1088/0264-9381/32/13/132001. arXiv: 1410.0509 [gr-qc].

[60] J. L. Jaramillo. "A note on degeneracy, marginal stability and extremality of black hole horizons". In: *Class. Quant. Grav.* 29 (2012), 177001. DOI: 10.1088/0264-9381/29/17/177001. arXiv: 1206.1271 [gr-qc].

[61] J. L. Jaramillo, R. P. Macedo, P. Moesta, and L. Rezzolla. "Black-hole horizons as probes of black-hole dynamics II: geometrical insights". In: *Phys. Rev. D* 85 (2012), 084031. DOI: 10.1103/PhysRevD.85.084031. arXiv: 1108.0061 [gr-qc].

[62] J. L. Jaramillo, R. Panosso Macedo, P. Moesta, and L. Rezzolla. "Black-hole horizons as probes of black-hole dynamics I: post-merger recoil in head-on collisions". In: *Phys. Rev. D* 85 (2012), 084030. DOI: 10.1103/PhysRevD.85.084030. arXiv: 1108.0060 [gr-qc].

[63] J. L. Jaramillo, M. Reiris, and S. Dain. "Black hole Area-Angular momentum inequality in non-vacuum spacetimes". In: *Phys. Rev. D* 84 (2011), 121503. DOI: 10.1103/PhysRevD.84.121503. arXiv: 1106.3743 [gr-qc].

[64] F. Johansson et al. *mpmath: a Python library for arbitrary-precision floating-point arithmetic (version 1.0.0)*. http://mpmath.org/. Nov. 2018.

[65] J. Keating. "The quantum mechanics of chaotic systems or 'Can one hear the chaology of a drum?'" In: *The nature of chaos*. Ed. by T. Mullin. Oxford University Press, 1993. Chap. 12.

[66] *Kranc: Kranc Assembles Numerical Code*. URL: http://kranccode.org/.

[67] B. Krishnan. "Fundamental properties and applications of quasi-local black hole horizons". In: *Class. Quant. Grav.* 25 (2008). Ed. by S. M. Scott and D. E. McClelland, 114005. DOI: 10.1088/0264-9381/25/11/114005. arXiv: 0712.1575 [gr-qc].

[68] B. Krishnan. "Isolated Horizons in Numerical Relativity". Ph.D. thesis. 2002.

[69] F. Löffler et al. "The Einstein Toolkit: A Community Computational Infrastructure for Relativistic Astrophysics". In: *Class. Quantum Grav.* 29.11 (2012), 115001. DOI: doi:10.1088/0264-9381/29/11/115001. eprint: arXiv:1111.3344[gr-qc].

[70] M. Mars. "Present status of the Penrose inequality". In: *Class. Quant. Grav.* 26 (2009), 193001. DOI: 10.1088/0264-9381/26/19/193001. arXiv: 0906.5566 [gr-qc].

[71]   R. A. Matzner et al. "Geometry of a black hole collision". In: *Science* 270 (1995), 941–947. DOI: 10.1126/science.270.5238.941.

[72]   R. A. Matzner, M. F. Huq, and D. Shoemaker. "Initial data and coordinates for multiple black hole systems". In: *Phys. Rev. D* 59 (1999), 024015. DOI: 10.1103/PhysRevD.59.024015. arXiv: gr-qc/9805023.

[73]   A. Meurer et al. "SymPy: symbolic computing in Python". In: *PeerJ Computer Science* 3 (2017), e103. DOI: 10.7717/peerj-cs.103.

[74]   M. J. Mohlenkamp. *A user's guide to spherical harmonics*. Available at http://www.ohiouniversityfaculty.com/mohlenka/research/uguide.pdf (Accessed: 15 Aug. 2019). Oct. 2016.

[75]   P. Mösta, L. Andersson, J. Metzger, B. Szilágyi, and J. Winicour. "The Merger of Small and Large Black Holes". In: *Class. Quant. Grav.* 32.23 (2015), 235003. DOI: 10.1088/0264-9381/32/23/235003. arXiv: 1501.05358 [gr-qc].

[76]   A. H. Nitz et al. "1-OGC: The first open gravitational-wave catalog of binary mergers from analysis of public Advanced LIGO data". In: *Astrophys. J.* 872.2 (2019), 195. DOI: 10.3847/1538-4357/ab0108. arXiv: 1811.01921 [gr-qc].

[77]   A. H. Nitz et al. "2-OGC: Open Gravitational-wave Catalog of binary mergers from analysis of public Advanced LIGO and Virgo data". In: *Astrophys. J.* 891 (Oct. 2019), 123. DOI: 10.3847/1538-4357/ab733f. arXiv: 1910.05331 [astro-ph.HE].

[78]   R. Penrose. "Naked singularities". In: *Annals N. Y. Acad. Sci.* 224 (1973), 125–134. DOI: 10.1111/j.1749-6632.1973.tb41447.x.

[79]   R. Penrose. "Gravitational collapse and space-time singularities". In: *Phys. Rev. Lett.* 14 (1965), 57–59. DOI: 10.1103/PhysRevLett.14.57.

[80]   D. Pook-Kolb, O. Birnholtz, J. L. Jaramillo, B. Krishnan, and E. Schnetter. "Horizons in a binary black hole merger I: Geometry and area increase". In: *arXiv preprint* (June 2020). arXiv: 2006.03939 [gr-qc].

[81]   D. Pook-Kolb, O. Birnholtz, J. L. Jaramillo, B. Krishnan, and E. Schnetter. "Horizons in a binary black hole merger II: Fluxes, multipole moments and stability". In: *arXiv preprint* (June 2020). arXiv: 2006.03940 [gr-qc].

[82]   D. Pook-Kolb, O. Birnholtz, B. Krishnan, and E. Schnetter. "Existence and stability of marginally trapped surfaces in black-hole spacetimes". In: *Phys. Rev. D* 99 (6 Mar. 2019), 064005. DOI: 10.1103/PhysRevD.99.064005.

[83]   D. Pook-Kolb, O. Birnholtz, B. Krishnan, and E. Schnetter. "Interior of a Binary Black Hole Merger". In: *Phys. Rev. Lett.* 123 (17 Oct. 2019), 171102. DOI: 10.1103/PhysRevLett.123.171102.

[84] D. Pook-Kolb, O. Birnholtz, B. Krishnan, and E. Schnetter. "Self-intersecting marginally outer trapped surfaces". In: *Phys. Rev. D* 100 (8 Oct. 2019), 084044. DOI: 10.1103/PhysRevD.100.084044.

[85] D. Pook-Kolb et al. *MOTS Finder version 1.4*. June 2020. DOI: 10.5281/zenodo.3885191.

[86] V. Prasad, A. Gupta, S. Bose, B. Krishnan, and E. Schnetter. "News from horizons in binary black hole mergers". In: (Mar. 2020). arXiv: 2003.06215 [gr-qc].

[87] F. Pretorius. "Numerical relativity using a generalized harmonic decomposition". In: *Classical and Quantum Gravity* 22.2 (Jan. 2005), 425–451. DOI: 10.1088/0264-9381/22/2/014. URL: https://doi.org/10.1088%2F0264-9381%2F22%2F2%2F014.

[88] L. Rezzolla, R. P. Macedo, and J. L. Jaramillo. "Understanding the 'anti-kick' in the merger of binary black holes". In: *Phys. Rev. Lett.* 104 (2010), 221101. DOI: 10.1103/PhysRevLett.104.221101. arXiv: 1003.0873 [gr-qc].

[89] R. Sachs. "Gravitational waves in general relativity. 8. Waves in asymptotically flat space-times". In: *Proc. Roy. Soc. Lond. A* A270 (1962), 103–126. DOI: 10.1098/rspa.1962.0206.

[90] E. B. Saff and A. B. Kuijlaars. "Distributing many points on a sphere". In: *The mathematical intelligencer* 19.1 (1997), 5–11.

[91] E. Schnetter. "A Fast apparent horizon algorithm". In: (June 2002). arXiv: gr-qc/0206003.

[92] E. Schnetter. "Finding apparent horizons and other two surfaces of constant expansion". In: *Class. Quant. Grav.* 20 (2003), 4719–4737. DOI: 10.1088/0264-9381/20/22/001. arXiv: gr-qc/0306006.

[93] E. Schnetter, B. Krishnan, and F. Beyer. "Introduction to dynamical horizons in numerical relativity". In: *Phys. Rev. D* 74 (2006), 024028. DOI: 10.1103/PhysRevD.74.024028. arXiv: gr-qc/0604015.

[94] J. Thornburg. "A Fast Apparent-Horizon Finder for 3-Dimensional Cartesian Grids in Numerical Relativity". In: *Class. Quant. Grav.* 21 (2004), 743–766. DOI: 10.1088/0264-9381/21/2/026. arXiv: gr-qc/0306056.

[95] J. Thornburg. "Finding apparent horizons in numerical relativity". In: *Phys. Rev. D* 54 (1996), 4899–4918. DOI: 10.1103/PhysRevD.54.4899. eprint: arXiv:gr-qc/9508014.

[96] S. van der Walt, S. C. Colbert, and G. Varoquaux. "The NumPy Array: A Structure for Efficient Numerical Computation". In: *Computing in Science Engineering* 13.2 (Mar. 2011), 22–30. ISSN: 1521-9615. DOI: `10.1109/MCSE.2011.37`.

[97] T. Venumadhav, B. Zackay, J. Roulet, L. Dai, and M. Zaldarriaga. "New Binary Black Hole Mergers in the Second Observing Run of Advanced LIGO and Advanced Virgo". In: (2019). arXiv: `1904.07214 [astro-ph.HE]`.

[98] P. Virtanen et al. "SciPy 1.0: Fundamental Algorithms for Scientific Computing in Python". In: *Nature Methods* 17 (2020), 261–272. DOI: `https://doi.org/10.1038/s41592-019-0686-2`.

[99] S. Wimberger. *Nonlinear Dynamics and Quantum Chaos.* Switzerland: Springer International Publishing, 2014.

[100] B. Zackay, T. Venumadhav, L. Dai, J. Roulet, and M. Zaldarriaga. "Highly spinning and aligned binary black hole merger in the Advanced LIGO first observing run". In: *Phys. Rev. D* 100.2 (2019), 023007. DOI: `10.1103/PhysRevD.100.023007`. arXiv: `1902.10331 [astro-ph.HE]`.

Curriculum Vitae

Professional experience

2019	Scientific talk at the 22nd International Conference on General Relativity and Gravitation, Valencia, Spain
2019	Scientific talk at the 22nd Eastern Gravity Meeting, North Dartmouth, USA
2019	Two-week stay at the Perimeter Institute for Theoretical Physics, Waterloo, Canada
since 2018	Scientific employee (Wissenschaftlicher Mitarbeiter) and PhD student at the Max Planck Institute for Gravitational Physics (Albert-Einstein-Institute) and the Leibniz Universität Hannover
2001–2018	Software development and support in the visual effects industry

Education

2012–2018	Studies of physics at the Leibniz Universität Hannover, 2018 Master of Science
2008–2012	Studies of physics at the Leibniz Universität Hannover, 2012 Bachelor of Science
1990–2001	School education up to and including grade 11, the latter at the St. Ursula-Schule, Hannover